

**DETERMINATION OF AXIAL LOAD AND SUPPORT STIFFNESS
OF CONTINUOUS BEAMS BY VIBRATION ANALYSIS**

by

Thomas P. Boggs

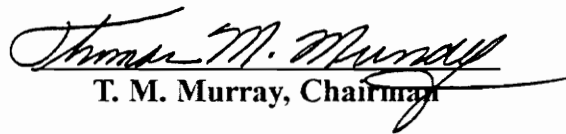
**Thesis submitted to the Faculty of the
Virginia Polytechnic Institute & State University
in partial fulfillment of the requirements for the degree of**

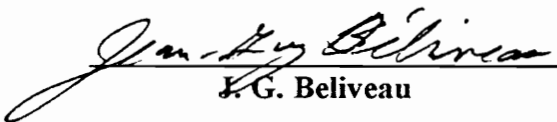
MASTER OF SCIENCE

in

CIVIL ENGINEERING

APPROVED:


T. M. Murray, Chairman


J. G. Beliveau


R. H. Plaut

October, 1994

Blacksburg, Virginia

C. 2

LD
5655
V855
1994
B644
C. 2

DETERMINATION OF AXIAL LOAD AND SUPPORT STIFFNESS OF CONTINUOUS BEAMS BY VIBRATION ANALYSIS

by

Thomas P. Boggs

Thomas M. Murray, Chairman

Civil Engineering

(ABSTRACT)

Three models are presented which predict frequencies and mode shapes of transverse vibration for a continuous prismatic Bernoulli-Euler beam on elastic supports, subjected to a compressive axial load. The first model, which approximates support stiffnesses by an equivalent elastic foundation, is found to be inaccurate for wave lengths close to the support spacing. A discrete mass model is formulated which accounts for axial load by stability functions which modify the element stiffness matrices. A continuous model is formulated which yields an exact solution for Bernoulli-Euler beam theory. The frequencies predicted by the discrete mass model and continuous model are in excellent agreement. A method of predicting axial compressive load and support stiffness based on measured frequency and phase data is presented which can be used for either the discrete mass model or the continuous model. A frequency reduction factor is derived which accounts for the effects of shear deformation and rotatory inertia. Tests are performed on an eight span beam with compressive axial load. Test results show that the models accurately predict frequencies and mode shapes of vibration. Results indicate that the method formulated can be used to determine compressive axial load and support stiffness.

Acknowledgment

I would like to thank my committee members, Prof. Jean-Guy Beliveau, Prof. Thomas M. Murray, and Prof. Raymond H. Plaut for their help over the past year. A special thanks goes to Prof. Beliveau whose guidance over the past year has been invaluable. I would like to thank Brett Farmer and Dennis Huffman for their assistance in the experimental portion of this research.

I would like to thank my parents, Willis Boggs and Ruth Zimmer-Boggs, for their support and encouragement over the years and for helping make my education possible. Finally, I would like to thank Susan Wheedleton, whose love and companionship over the last few years have been immeasurable.

TABLE OF CONTENTS

ABSTRACT	ii
ACKNOWLEDGMENT	iii
LIST OF FIGURES	vi
LIST OF TABLES	viii
NOMENCLATURE	ix
 CHAPTER	
I. INTRODUCTION	1
1.1 Objective	1
1.2 Literature Review.....	2
II. BEAM ON WINKLER FOUNDATION	5
2.1 Governing Equation	5
2.2 Infinite Beam	7
2.3 Finite Beam	10
2.4 Limitations of Model	13
III. DISCRETE MASS MODEL OF FINITE BEAM ON ELASTIC SUPPORTS	16
3.1 Eigenvalue Equation	16
3.2 Mass Matrix	17
3.3 Stiffness Matrix.....	18
3.4 Natural Frequencies and Mode Shapes	21
3.5 Load and Stiffness Determination	26
3.6 Effect of Shear and Rotatory Inertia	38

TABLE OF CONTENTS (cont.)

IV. CONTINUOUS MODEL OF FINITE BEAM ON ELASTIC SUPPORTS	41
4.1 General Equation of Motion	41
4.2 Characteristic Matrix	43
4.3 Natural Frequencies and Mode Shapes	44
V. EXPERIMENT AND ANALYSIS	52
5.1 Introduction	52
5.2 Test Setup	53
5.3 Data Acquisition	58
5.4 Results	59
5.5 Possible Effects of End Support Stiffness	82
VI. CONCLUSION	100
REFERENCES	102
APPENDIX A - DERIVATION OF SHEAR FACTOR	104
APPENDIX B - DISCRETE MASS MODEL CODE	109
APPENDIX C - CONTINUOUS MODEL CODE	114
APPENDIX D - DATA FOR MODE SHAPE DETERMINATION IN SECTION 5.4	120
APPENDIX E - DRIVING POINT FRF'S	137
VITA	148

List of Figures

- 2.1 Infinite Beam on Elastic Supports
- 2.2 Free Body Diagram of Winkler Model Beam Segment
- 2.3 Dispersion Plot for Various Axial Loads
- 2.4 Finite Beam on Elastic Supports
- 2.5 Winkler Model Frequencies vs. Axial Load
- 2.6 Pinned-Pinned Mode of Vibration
- 3.1 Degrees of Freedom of Beam Element
- 3.2 Mode 1 Eigenvector for Discrete Mass Model
- 3.3 Mode 2 Eigenvector for Discrete Mass Model
- 3.4 Mode 3 Eigenvector for Discrete Mass Model
- 3.5 Mode 4 Eigenvector for Discrete Mass Model
- 3.6 Mode 5 Eigenvector for Discrete Mass Model
- 3.7 Mode 6 Eigenvector for Discrete Mass Model
- 3.8 Mode 7 Eigenvector for Discrete Mass Model
- 3.9 Mode 8 Eigenvector for Discrete Mass Model
- 3.10 Frequency vs. Axial Load for Discrete Model and Winkler Model
- 3.11 Mode 1 Mesh Plot
- 3.12 Mode 2 Mesh Plot
- 3.13 Mode 3 Mesh Plot
- 3.14 Mode 4 Mesh Plot
- 3.15 Mode 5 Mesh Plot
- 3.16 Mode 6 Mesh Plot
- 3.17 Mode 7 Mesh Plot
- 3.18 Mode 8 Mesh Plot
- 3.19 Contour Plot for Load and Stiffness Determination
- 4.1 Free Body Diagram of Beam Segment at an Intermediate Support
- 4.2 Mode 1 Shape for Continuous, Discrete, and Winkler Model
- 4.3 Mode 2 Shape for Continuous, Discrete, and Winkler Model
- 4.4 Mode 3 Shape for Continuous, Discrete, and Winkler Model
- 4.5 Mode 4 Shape for Continuous, Discrete, and Winkler Model
- 4.6 Mode 5 Shape for Continuous, Discrete, and Winkler Model
- 4.7 Mode 6 Shape for Continuous, Discrete, and Winkler Model
- 4.8 Mode 7 Shape for Continuous, Discrete, and Winkler Model
- 4.9 Mode 8 Shape for Continuous, Discrete, and Winkler Model
- 4.10 Frequency vs. Axial Load for Continuous Model and Discrete Model
- 5.1 End of Test Beam

5.2	Left End Support
5.3	Right End Support
5.4	Intermediate Support
5.5	Impact Locations
5.6	Typical Hammer Impact Excitation
5.7	Typical Hammer Impact Spectrum
5.8	Typical Accelerometer Response
5.9	Typical FRF
5.10	Mode 1 Eigenvector
5.11	Mode 4 Eigenvector
5.12	Mode 5 Eigenvector
5.13	Mode 7 Eigenvector
5.14	Mode 8 Eigenvector
5.15	Measured Frequencies vs. Axial Load for $k_s=2.7$ kip/in.
5.16	Measured Frequencies vs. Axial Load for $k_s=5.4$ kip/in.
5.17	Contour Plot for $k_s=2.7$ kip/in. , $P=5$ kips
5.18	Contour Plot for $k_s=2.7$ kip/in. , $P=10$ kips
5.19	Contour Plot for $k_s=2.7$ kip/in. , $P=15$ kips
5.20	Contour Plot for $k_s=2.7$ kip/in. , $P=20$ kips
5.21	Contour Plot for $k_s=2.7$ kip/in. , $P=25$ kips
5.22	Contour Plot for $k_s=5.4$ kip/in. , $P=5$ kips
5.23	Contour Plot for $k_s=5.4$ kip/in. , $P=10$ kips
5.24	Contour Plot for $k_s=5.4$ kip/in. , $P=15$ kips
5.25	Contour Plot for $k_s=5.4$ kip/in. , $P=20$ kips
5.26	Contour Plot for $k_s=5.4$ kip/in. , $P=25$ kips
5.27	Estimated vs. Applied Axial Load for $k_s=2.7$ kip/in.
5.28	Estimated vs. Applied Axial Load for $k_s=5.4$ kip/in.
5.29	Effect of Ram End Support Stiffness on Mode 8 Frequency
5.30	Modified Model Contour Plot for $k_s=2.7$ kip/in. , $P=5$ kips
5.31	Modified Model Contour Plot for $k_s=2.7$ kip/in. , $P=10$ kips
5.32	Modified Model Contour Plot for $k_s=2.7$ kip/in. , $P=15$ kips
5.33	Modified Model Contour Plot for $k_s=2.7$ kip/in. , $P=20$ kips
5.34	Modified Model Contour Plot for $k_s=2.7$ kip/in. , $P=25$ kips
5.35	Modified Model Contour Plot for $k_s=5.4$ kip/in. , $P=5$ kips
5.36	Modified Model Contour Plot for $k_s=5.4$ kip/in. , $P=10$ kips
5.37	Modified Model Contour Plot for $k_s=5.4$ kip/in. , $P=15$ kips
5.38	Modified Model Contour Plot for $k_s=5.4$ kip/in. , $P=20$ kips
5.39	Modified Model Contour Plot for $k_s=5.4$ kip/in. , $P=25$ kips
5.40	Estimated vs. Applied Axial Load for $k_s=2.7$ kip/in. using Assumed End Stiffness
5.41	Estimated vs. Applied Axial Load for $k_s=5.4$ kip/in. using Assumed End Stiffness
5.42	Measured Frequencies Compared to Modified Frequencies for $k_s=2.7$ kip/in.
5.43	Measured Frequencies Compared to Modified Frequencies for $k_s=5.4$ kip/in.

List of Tables

- 3.1 Error in Frequency and Predicted Load due to Shear and Rotatory Inertia
- 5.1 Magnitude and Phase of Driving Point FRF for $k_s=2.7$ kip/in., $P=20$ kips
- 5.2 Estimated Loads and Stiffnesses
- 5.3 Estimated Loads and Stiffnesses for Assumed End Support Stiffness

NOMENCLATURE

k	=	beam element stiffness matrix
k_s	=	intermediate support stiffness
k'	=	shear area factor
l	=	length of beam element
m	=	mass per unit length of beam
m	=	element mass matrix
n	=	mode number of vibration
r	=	radius of gyration of beam cross-section
s	=	distance between supports
v	=	transverse displacement of beam
C	=	matrix of constants
CM	=	characteristic matrix
D	=	reduced system flexibility matrix
D_g	=	global system flexibility matrix
E	=	modulus of elasticity
G	=	shear modulus
I	=	area moment of inertia of beam cross-section
K	=	elastic modulus of Winkler foundation
K	=	reduced system stiffness matrix
K_g	=	global system stiffness matrix
L	=	length of beam
M	=	bending moment
M	=	reduced system mass matrix
P	=	axial load on beam
P_b	=	buckling load of beam
V	=	vertical force
X	=	system eigenvector
α	=	rotation of beam cross-section due to bending
β	=	rotation of beam cross section due to shear deformation
ϕ	=	stability function
λ	=	wave length of vibration
ω	=	frequency; natural frequency
ω_n	=	natural frequency for mode n
Φ_n	=	frequency reduction factor for mode n
Λ	=	wave number of vibration
Λ_b	=	buckling wave number

Chapter 1

Introduction

1.1 Objective

The primary objective of this thesis is to determine whether the compressive axial load and support stiffness of a prismatic Euler beam can be estimated from measurements of transverse vibrations. The method requires a model which can accurately predict modal frequencies for arbitrary combinations of axial load and support stiffness. The method developed applies to beams on multiple, evenly spaced elastic supports of identical linear stiffness. The method developed will be verified by comparison of predicted and applied loads for a test beam.

The first model presented approximates the stiffness of supports as a uniform stiffness distributed over a continuous foundation. This model applies to waves propagated in an infinite beam as well as standing waves in a finite beam. The second model is a finite element model which represents a finite beam on discrete elastic supports. The third model gives the exact solution for a finite Euler beam on discrete elastic supports.

1.2 Literature Review

The method developed in this thesis is directly applicable to the determination of compressive axial forces in the rails of railroad tracks. From a neutral stress state, a temperature increase of ΔT causes a continuous welded rail (CWR) to experience an axial load increase of

$$\Delta P = EA\alpha \cdot \Delta T \quad (1.1)$$

where E is the elastic modulus of the rail, A is the cross-sectional area of the rail, and α is the coefficient of thermal expansion. If the temperature increase becomes great enough (usually in the early afternoon on hot summer days), the increase in axial load is sufficient to cause lateral or vertical buckling of the track. To anticipate buckling, it is necessary not only to know the buckling load or maximum temperature increase of the track, but also to have an estimate of the current load state.

Railroad track mechanics dates back to the 1800's when Winkler (1867, 1875) modeled track as a beam on a uniform elastic foundation. Timoshenko (1915, 1926, 1932) successfully applied Winkler's model to track laid on transverse ties (a.k.a. sleepers). According to Kerr (1974), vertical track buckling analyses by Corini (1936), Huber (1941), and Engel (1960) extended the Winkler model to include the effect of axial load. Much work has been presented by Kerr (1974, 1975, 1976, 1978, 1979, 1980,

1986) on the mechanics of lateral and vertical track buckling including the effects of rail-tie interaction, bilinear lateral stiffness of ballast, and rail-vehicle interaction.

Grassie et al. (1982) investigated the dynamic response of track to lateral excitation in the 50-1500 Hz range. Measurement showed the presence of a ‘pinned-pinned’ mode of vibration around 350 Hz for which the wavelength of vibration is equal to twice the support spacing. This mode is not predicted by modeling the supports as an elastic foundation because the mode is due to the discrete nature of the supports. It was determined that wooden sleepers track is adequately modeled using an elastic foundation except near the pinned-pinned resonance. At frequencies above 300 Hz, the rail head was found to vibrate laterally on the flexibility of the rail web.

Grassie et al. (1982) also investigate the response of track to vertical excitation in the 50-1500 Hz range. The pinned-pinned mode of vertical vibration was measured at about 700 Hz. The elastic foundation model was found to be accurate for vertical vibration of wooden sleepers track, except around the pinned-pinned resonance. The elastic foundation model was found to be inaccurate for concrete sleepers track because of the flexibility of the rail pad.

Knothe and Grassie (1993) identify a number of sub-systems for the dynamic modeling of track and vehicle-track interaction:

1. Vehicle, including car body, bogie, and wheel set.
2. Wheel-rail contact and representation of excitation.
3. Rail.
4. Fastening system, including rail fastening and rail pad.
5. Sleeper (tie).
6. Sleeper support, including ballast and substrate.

For this thesis, systems 1-2 are not relevant since it is the free vibration response that is of interest. Knothe and Grassie claim that rail responses due to vertical excitation can be adequately represented by Bernoulli beam theory for frequencies less than about 500 Hz. Above 500 Hz, Timoshenko theory is required and above 2.5 kHz a simple Timoshenko beam is inaccurate because significant warping of the rail cross-section occurs. Knothe et al. (1994) compare various one, two, and three dimensional rail models including finite element models for the beam cross-section. They conclude that a finite element model is the best for the high frequency vibration of a rail on discrete supports.

Lusignea et al. (1979) perform tests in the high frequency range (500-20,000 Hz) on a free segment of rail. They claim that the high frequency range is best for the determination of axial load because frequencies in this range are less dependent on the rail fastener, tie, ballast, and subgrade. Measurements in the 1-10 kHz range showed significant warping of the rail cross-section.

Livingston (1993) develops a parameter estimation technique for determining the axial load and support stiffness of an Euler beam supported at both ends and subjected to a tensile axial load. The method developed in this thesis is similar to that of Livingston, but formulated for a member with intermediate elastic supports.

Chapter 2

Winkler Foundation Model

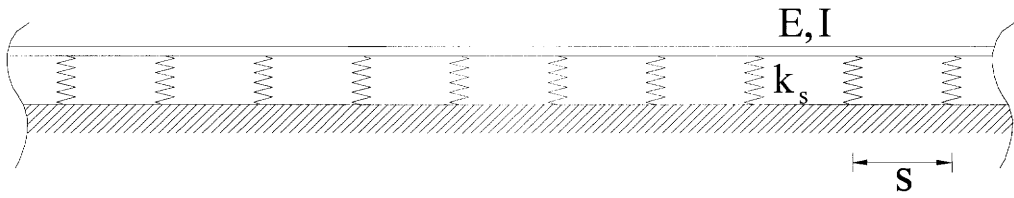


Fig.(2.1) Infinite Beam on Elastic Supports

2.1 Governing Equation

Consider a beam resting on equally spaced elastic supports of identical stiffness as in Fig.(2.1). If one considers wavelengths of vibration which are large compared to support spacings then the stiffnesses of the discrete supports can be modeled by an equivalent stiffness per unit length of beam. The beam is then referred to as resting on an elastic foundation or a Winkler foundation (Winkler, 1867). The distributed stiffness of the foundation is given by

$$K = k_s / S \quad (2.1)$$

where k_s is the support stiffness, s is the support spacing, and K is the stiffness per unit length of the elastic foundation.

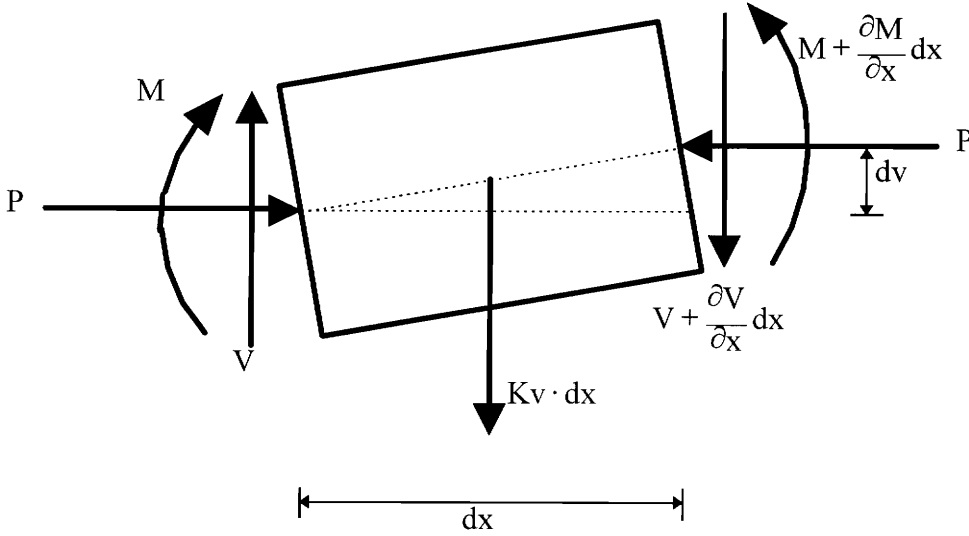


Fig.(2.2) Free Body Diagram of Winkler Model Beam Segment

If the effects of shear deformation and rotatory inertia are considered negligible, then the summation of vertical forces for the differential beam segment of Fig.(2.1) gives

$$m \frac{\partial^2 v}{\partial t^2} dx = V - (V + \frac{\partial V}{\partial x} dx) - K v \cdot dx \quad (2.2)$$

where m is the mass per unit length of beam, v is the transverse deflection of the element, and V is the vertical force on the end of the element. (Note that V is not properly called a shearing force since it does not act perpendicular to the neutral axis of the element.)

Simplifying gives

$$m \frac{\partial^2 v}{\partial t^2} + \frac{\partial V}{\partial x} + Kv = 0. \quad (2.3)$$

Summing moments about the right end of the element at the centroid gives

$$mr^2 \frac{\partial^2 \alpha}{\partial t^2} = 0 = (M + \frac{\partial M}{\partial x} dx) - M - V \cdot dx + Kv \cdot dx \cdot \frac{dx}{2} + P \cdot dv \quad (2.4)$$

As $dx \rightarrow 0$, this gives

$$V = \frac{\partial M}{\partial x} + P \frac{\partial v}{\partial x}. \quad (2.5)$$

Substituting equation (2.5) into equation (2.3) and using $M = EI \frac{\partial^2 v}{\partial x^2}$ results in

$$m \frac{\partial^2 v}{\partial t^2} + EI \frac{\partial^4 v}{\partial x^4} + P \frac{\partial^2 v}{\partial x^2} + Kv = 0. \quad (2.6)$$

Equation (2.6) is the differential equation of motion for the free transverse vibration of an axially loaded Euler beam on a Winkler foundation.

2.2 Infinite Beam

If a sinusoidal displacement of the form

$$v(x, t) = [A \sin(\Lambda x) + B \cos(\Lambda x)] \sin(\omega t) \quad (2.7)$$

is assumed, where ω is frequency and $\Lambda = 2\pi/\lambda$ is the wave number, then substitution into equation (2.6) gives the dispersion relation

$$\omega = \left[\frac{1}{m} (EI\Lambda^4 - P\Lambda^2 + K) \right]^{\frac{1}{2}}. \quad (2.8)$$

Equation (2.8) describes the relation between the frequency and wave length of vibration for an infinite beam. If E , I , and m are known, then P and K can be determined from the measurement of ω vs. Λ . By differentiating equation (2.8) with respect to Λ and solving for the lowest frequency (ω_{\min}) and corresponding wave number (Λ_{crit}), the following equations for P and K can be derived:

$$P = 2EI\Lambda_{\text{crit}}^2 \quad (2.9)$$

$$K = m\omega_{\min}^2 + EI\Lambda_{\text{crit}}^4 \quad (2.10)$$

Buckling of the infinite beam occurs when the lowest frequency of vibration becomes zero. By setting $\omega_{\min} = 0$ in equation (2.10) the buckling load of the infinite beam is determined to be

$$P_b = 2\sqrt{KEI} \quad (2.11)$$

with a corresponding wave number of

$$\Lambda_b = \left(\frac{K}{EI}\right)^{\frac{1}{4}} \quad (2.12)$$

Fig.(2.3) depicts the dispersion relation of an infinite S4x7.7 beam for various axial loads. The elastic foundation corresponds to 2.7 kip/in. elastic supports spaced at 2 ft. intervals. It can be seen that the presence of axial load has little effect on frequencies corresponding to small wave numbers (i.e., large wave lengths). In fact, the frequency corresponding to $\Lambda=0$ is independent of axial load. The $\Lambda=0$ mode of vibration

Frequency vs. Wave Number for Various Axial Loads

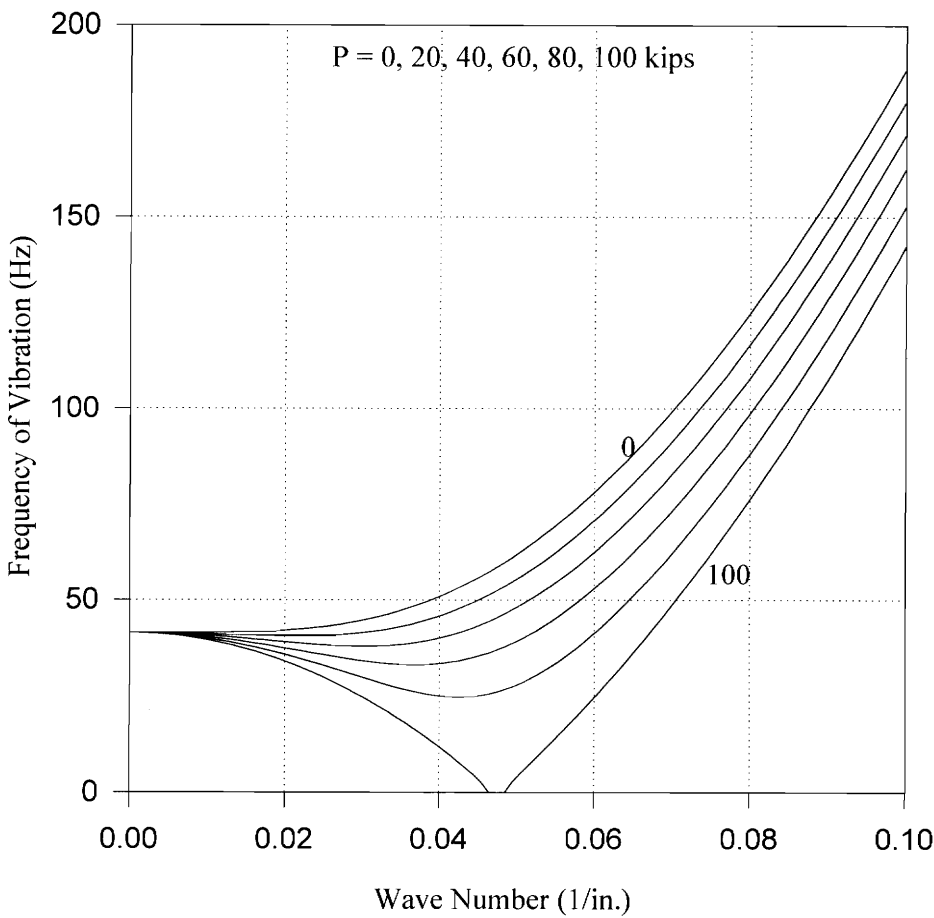


Fig.(2.3) Dispersion Plot for Various Axial Loads

corresponds to an infinite wave length which implies that the entire beam undergoes a rigid body motion on the elastic foundation. Thus, as Fig.(2.3) implies, to observe the effect of axial load, frequency measurements must be taken for wave lengths for which bending is significant.

2.3 Finite Beam

In examining the vibrations of a finite beam on a Winkler foundation, the present investigation will use the case of a pinned-pinned beam. For a pinned-pinned beam, equation (2.7) must satisfy the following boundary conditions:

$$\begin{aligned}
 v(0, t) &= 0 \\
 v(L, t) &= 0 \\
 M(0, t) &= EI \left. \frac{\partial^2 v}{\partial x^2} \right|_{x=0} = 0 \\
 M(L, t) &= EI \left. \frac{\partial^2 v}{\partial x^2} \right|_{x=L} = 0
 \end{aligned} \tag{2.13}$$

Applying the first boundary condition to equation (2.7) requires that $B=0$. Rejecting the trivial cases of $A=0$ and $\omega t=0$ leaves the condition that

$$\sin(\Lambda L) = 0 \tag{2.14}$$

which can occur only for

$$\Lambda = \frac{n\pi}{L} \tag{2.15}$$

where n is an integer. The transverse displacement of the beam is then given by

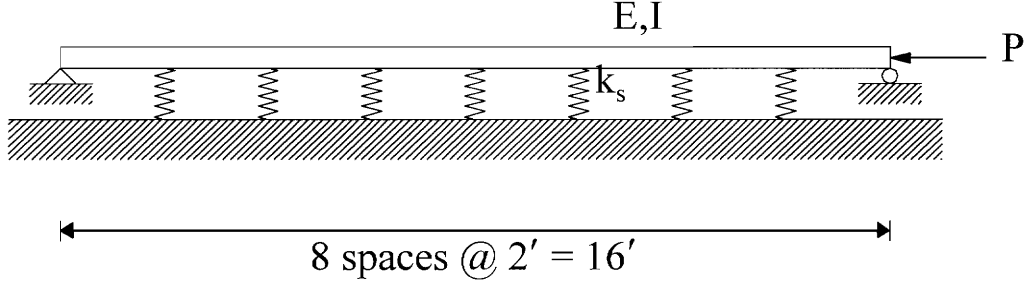


Fig.(2.4) Finite Beam on Elastic Supports

$$v(x, t) = A \sin\left(\frac{n\pi}{L} x\right) \sin(\omega t) \quad (2.16)$$

which also satisfies the last two boundary conditions of equation (2.13). Equation (2.15) implies that the only possible wave lengths of vibration are those satisfying

$$\lambda = \frac{2L}{n} ; \quad n = 1, 2, 3, \dots \quad (2.17)$$

Substituting equation (2.15) into equation (2.8) gives the dispersion relation for a pinned-pinned beam on a Winkler foundation:

$$\omega_n = \left(\frac{1}{m} \left[EI \left(\frac{n\pi}{L} \right)^4 - P \left(\frac{n\pi}{L} \right)^2 + K \right] \right)^{\frac{1}{2}} \quad n = 1, 2, 3, \dots \quad (2.18)$$

An equivalent form of equation (2.18) was derived by Lusignea et al. (1979).

Fig.(2.5) shows frequency vs. axial load for the first 8 modes of a 16 ft. S4x7.7 beam with 2.7 kip/in. springs at 2 ft. spacings (Fig.(2.4)). The frequencies correspond

Frequency vs. Axial Load for Modes 1-8

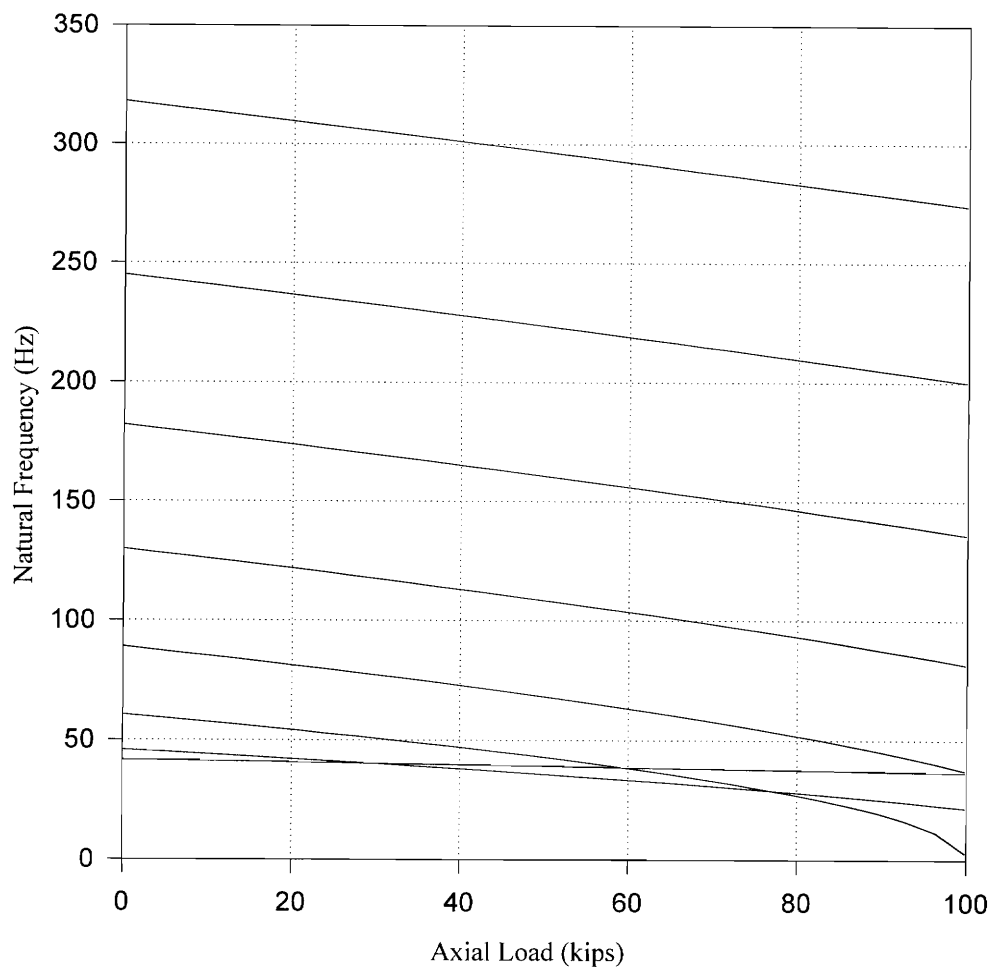


Fig.(2.5) Winkler Model Frequencies vs. Axial Load

to weak axis, transverse vibrations. The given springs and spacings correspond to a foundation stiffness of $K=0.113$ ksi. For no axial load the mode shapes are ranked in ascending order (i.e., first mode corresponds to lowest frequency, second mode corresponds to second lowest frequency, etc.). However, when sufficient axial load is present, the modal frequencies will cross. This phenomenon makes it no longer possible to distinguish modes by the order of the frequencies. The mode shapes must be measured to distinguish the frequencies of different modes.

2.4 Limitations of Model

Several factors limit the applicability of the Winkler foundation model for the determination of axial loads. As previously mentioned, the lower modes of vibration are affected very little by the presence of axial load. Deflections corresponding to these lower modes involve mostly elastic support displacements and very little beam flexure which makes these modes most suitable for determining support stiffnesses. To determine axial load it is better, if not necessary, to measure frequencies of higher modes where beam flexure becomes significant.

While higher modes of vibration are more strongly affected by axial load, there is also the possibility that the Winkler foundation model assumptions are no longer accurate. As the mode number increases, the wave length of vibration decreases. As the wave length approaches the elastic support spacing, the assumption of an elastic

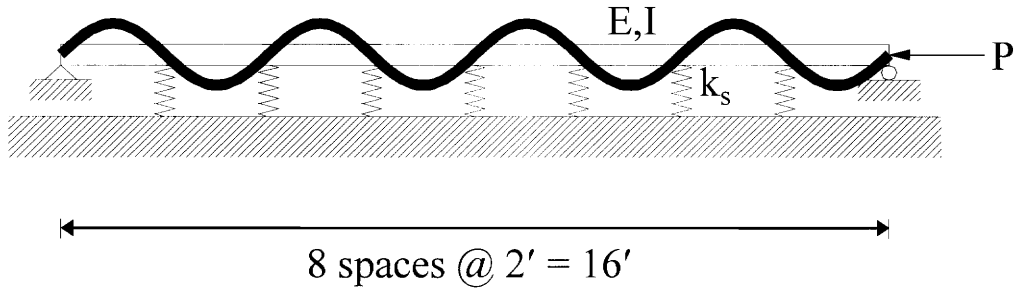


Fig.(2.6) Pinned-Pinned Mode of Vibration

foundation becomes less accurate. A clear example of this phenomenon can be given by considering the $n=8$ mode of vibration for the beam of Fig.(2.4). For this mode the mode shape has a node (i.e., no displacement) at each of the intermediate supports (Fig.(2.6)) (Hereafter, this mode will be referred to as the “pinned-pinned” mode). Since there are no displacements at any of the elastic supports, the support stiffnesses should have no effect on the frequency of the pinned-pinned mode; however, according to equation (2.18), the frequency of the $n=8$ mode is a function of the foundation stiffness (K). For the pinned-pinned mode, equation (2.18) would only give the correct frequency if K were equal to zero.

Another limit on the applicability of the Winkler foundation model is the possibility of shear deformation and rotatory inertia. When the wave length of vibration becomes sufficiently short, shear deformation contributes significantly to the beam deflection. Also, differential segments of the beam will have not only transverse inertia,

but also rotational inertia in the plane of vibration. Both of these effects will reduce the frequency of transverse vibration. When these effects are significant, Bernoulli-Euler beam theory is no longer adequate to describe the vibration of the beam; the beam must instead be modeled using Timoshenko beam theory (Timoshenko et al., 1990).

The number of modes which can accurately be described by the Winkler foundation model and which of the above described factors will limit its applicability are functions of several parameters. Bending stiffness, support stiffness, support spacing, and radius of gyration are all variables which determine the applicability of the model. Consequently, these factors will also limit the accuracy with which the Winkler foundation model can be used to determine axial load.

Chapter 3

Discrete Mass Model of Beam on Elastic Supports

3.1 Eigenvalue Equation

An alternative to the Winkler foundation model is to model the beam as a series of discrete or “lumped” masses connected by beam elements. Although a discrete mass model can be used only for the case of a finite beam, it has an advantage over the Winkler foundation model in that it does not need to approximate the elastic supports by an elastic foundation. Thus, a discrete mass model can be more accurate for higher modes of vibration.

The frequencies and mode shapes of the discrete mass system are determined by solving for the eigenvalues and eigenvectors of the system. The natural frequencies are found by solving the matrix equation

$$\det(\mathbf{K} - \omega^2 \mathbf{M}) = 0 \quad (3.1)$$

where \mathbf{K} and \mathbf{M} are the system stiffness and system mass matrices, respectively, and ω is the natural frequency of vibration. If \mathbf{K} and \mathbf{M} are $n \times n$ matrices, then equation (3.1) will yield n values of ω . The mode shapes of vibration are then determined by solving

$$\mathbf{K}\mathbf{X} = \omega^2 \mathbf{M}\mathbf{X} \quad (3.2)$$

for \mathbf{X} , which is an $n \times 1$ vector of mass displacements. The displacements of \mathbf{X} are not unique displacements; rather, they are displacements relative to one another which describe the shape, but not magnitude, of vibration corresponding to a given value of ω .

3.2 Mass Matrix

The mass matrix of equation (3.1) is assembled from the mass matrices of each of the discrete beam elements. These element mass matrices can be either lumped mass matrices or consistent mass matrices. The mass influence coefficients of a consistent mass matrix are given by

$$m_{ij} = \int_0^L m(x) \Psi_i(x) \Psi_j(x) \cdot dx \quad (3.3)$$

where $m(x)$ is the mass per unit length of the beam and $\Psi_i(x)$ and $\Psi_j(x)$ are interpolation functions for beam degrees of freedom i and j (Clough and Penzien, 1975). A lumped mass matrix typically ignores rotatory inertia and can be written as

$$\mathbf{m} = \frac{ml}{2} \begin{bmatrix} 1 & 0 & 0 & 0 \\ 0 & 0 & 0 & 0 \\ 0 & 0 & 1 & 0 \\ 0 & 0 & 0 & 0 \end{bmatrix} \quad (3.4)$$

where m is the mass per unit length of the element and l is the element length. Although the consistent mass matrix generally yields more accurate results, the lumped mass matrix will be used for two reasons: (1) rotatory inertia will be neglected in the discrete mass

model and (2) the lumped mass matrix can be reduced to eliminate rotational degrees of freedom.

Once the element mass matrices are assembled into a system mass matrix, it is convenient to reduce the matrix such that it only contains degrees of freedom corresponding to transverse displacements. Since the lumped mass matrix does not have mass coupling, reduction requires only the removal of all rows and columns corresponding to rotational degrees of freedom. For the example of a beam consisting of three equal beam elements, the reduced system mass matrix, \mathbf{M} , is given by

$$\mathbf{M} = \frac{mL}{6} \begin{bmatrix} 1 & 0 & 0 & 0 \\ 0 & 2 & 0 & 0 \\ 0 & 0 & 2 & 0 \\ 0 & 0 & 0 & 1 \end{bmatrix} \quad (3.5)$$

where L is the total length of the beam.

3.3 Stiffness Matrix

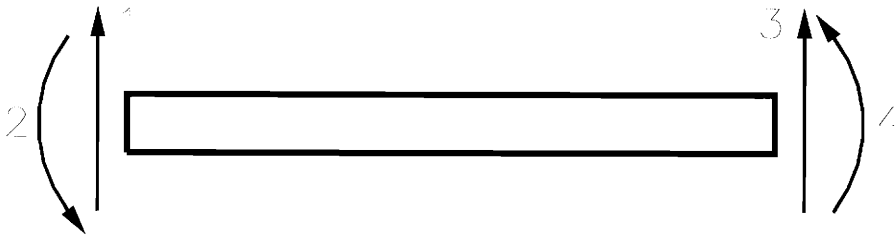


Fig.(3.1) Degrees of Freedom of Beam Element

Consider the beam element of Fig.(3.1). To account for the effect of a compressive axial load, the beam element stiffness matrix can be modified by stability functions so that

$$\mathbf{k} = \frac{EI}{l} \begin{bmatrix} \frac{12}{l^2} \phi_1 & \frac{6}{l} \phi_2 & -\frac{12}{l^2} \phi_1 & \frac{6}{l} \phi_2 \\ & 4\phi_3 & -\frac{6}{l} \phi_2 & 2\phi_4 \\ & & \frac{12}{l^2} \phi_1 & -\frac{6}{l} \phi_2 \\ \text{sym.} & & & 4\phi_3 \end{bmatrix} \quad (3.6)$$

where

$$\phi_1 = \frac{(\gamma l)^3 \sin \gamma l}{12\phi_c} \quad (3.7a)$$

$$\phi_2 = \frac{(\gamma l)^2 (1 - \cos \gamma l)}{6\phi_c} \quad (3.7b)$$

$$\phi_3 = \frac{\gamma l (\sin \gamma l - \gamma l \cos \gamma l)}{4\phi_c} \quad (3.7c)$$

$$\phi_4 = \frac{\gamma l (\gamma l - \sin \gamma l)}{2\phi_c} \quad (3.7d)$$

$$\phi_c = 2 - 2 \cos \gamma l - \gamma l \sin \gamma l \quad (3.7e)$$

$$\gamma = \sqrt{\frac{P}{EI}} \quad (3.7f)$$

(Ellyin, 1983). Each stability function is a function of the compressive axial load. It can be shown, by use of L' Hopital's Rule, that in the limit as the axial load approaches zero, the stability functions approach unity and the beam element stiffness matrix returns to its unmodified form.

The modified stiffness matrices can be assembled into a global stiffness matrix. The intermediate support stiffnesses can then be added to the diagonal elements of the stiffness matrix which correspond to the appropriate degrees of freedom (this assumes that the number of elements has been chosen such that degrees of freedom lie at the support locations). Pinned or fixed beam supports can be accounted for by conditions of compatibility or by modeling the supports as very stiff transverse or rotational springs.

Unlike the mass matrix, the global stiffness matrix requires a more detailed reduction procedure because the translational and rotational stiffness coefficients are coupled. Using a flexibility method, we first consider a set of forces

$$\mathbf{f} = \mathbf{K}_g \mathbf{D}_g \quad (3.8)$$

where \mathbf{K}_g is the global stiffness matrix and \mathbf{D}_g is the matrix of displacements corresponding to \mathbf{f} . Using again the example of a three element beam, let

$$\mathbf{f} = \begin{bmatrix} 1 & 0 & 0 & 0 \\ 0 & 0 & 0 & 0 \\ 0 & 1 & 0 & 0 \\ 0 & 0 & 0 & 0 \\ 0 & 0 & 1 & 0 \\ 0 & 0 & 0 & 0 \\ 0 & 0 & 0 & 1 \\ 0 & 0 & 0 & 0 \end{bmatrix} \quad (3.9)$$

Note that each column of \mathbf{f} represents a unit force vector acting on a single transverse degree of freedom. If \mathbf{K}_g is an $n \times n$ matrix, then \mathbf{f} is an $n \times \frac{n}{2}$ matrix. The displacements corresponding to \mathbf{f} are

$$\mathbf{D}_g = \mathbf{K}^{-1} \mathbf{f} \quad (3.10)$$

where \mathbf{D}_g and \mathbf{f} have the same dimensions. If all rotational displacements are now removed from \mathbf{D}_g (i.e., all even numbered rows), the remaining matrix is the reduced flexibility matrix, \mathbf{D} , which relates only transverse forces and displacements. To get the reduced stiffness matrix, \mathbf{K} , one need only invert \mathbf{D} to get

$$\mathbf{K} = \mathbf{D}^{-1} \quad (3.11)$$

where \mathbf{K} is a square matrix containing stiffness coefficients relating transverse forces and displacements.

3.4 Frequencies and Mode Shapes

Having calculated both \mathbf{M} and \mathbf{K} , equations (3.1) and (3.2) can be solved for the natural frequencies and mode shapes of the system. Caution must be taken, however, in choosing the number of elements with which to model the beam. The element stiffness matrix used in this discrete mass model is based on static deflection of the beam; it is not a dynamic stiffness matrix. Thus, in order to achieve accurate frequencies and mode shapes, the element length should be chosen such that it is significantly shorter than the shortest wavelength of vibration which is of interest.

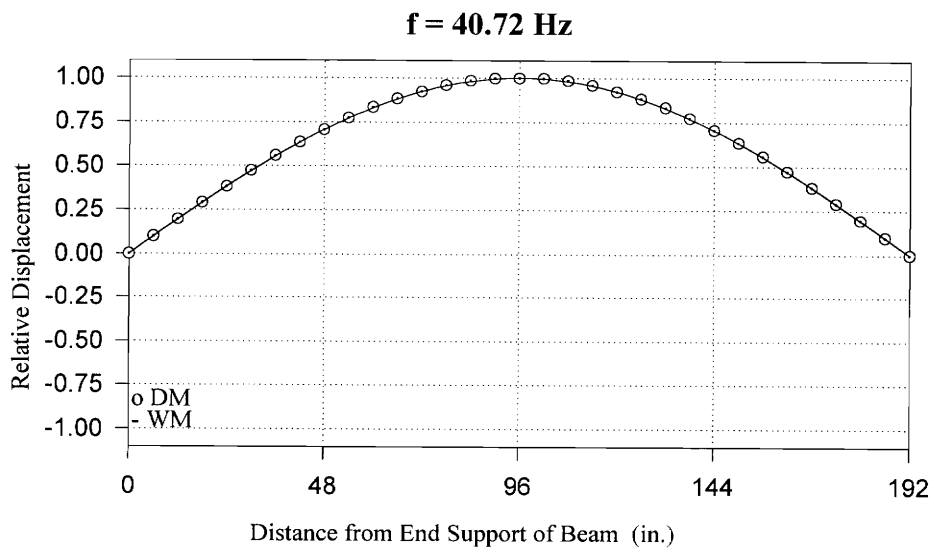


Fig.(2.2) Mode 1 Eigenvector for Discrete Mass Model

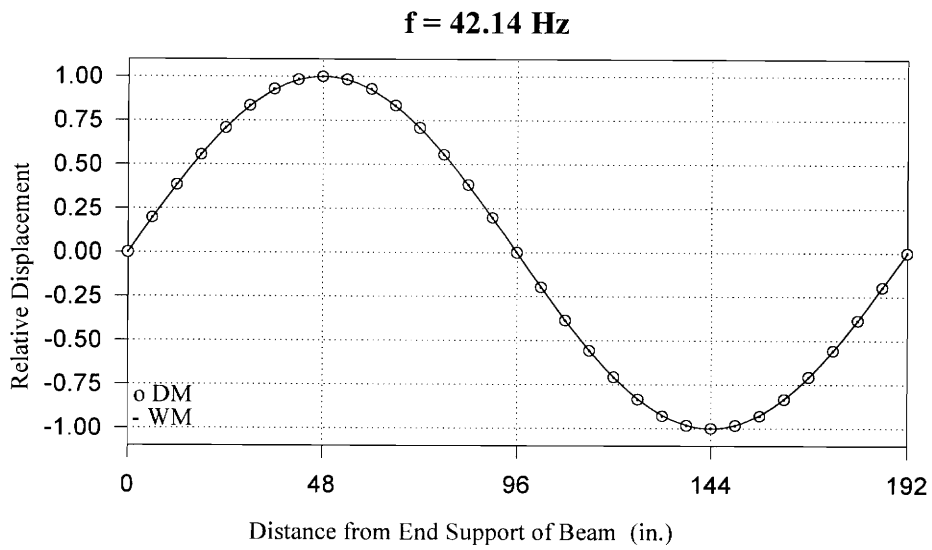


Fig.(2.3) Mode 2 Eigenvector for Discrete Mass Model

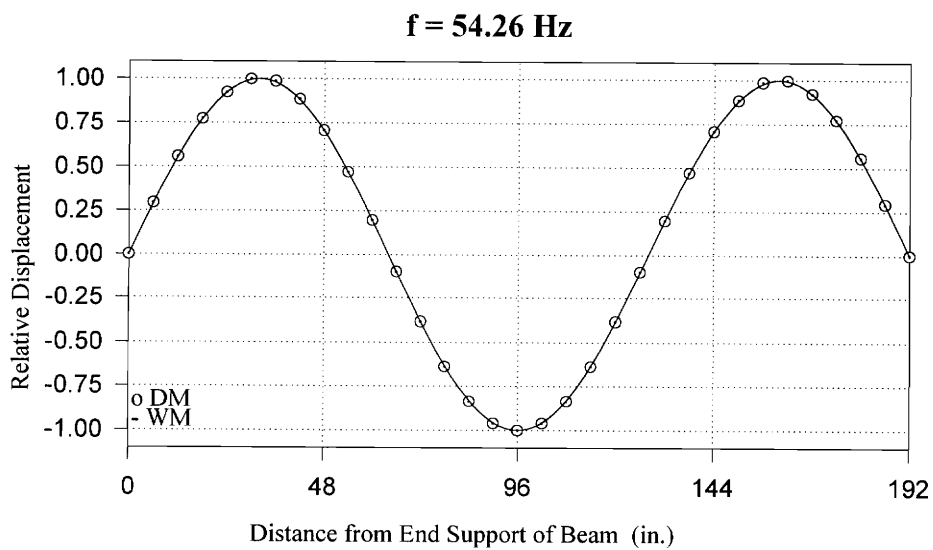


Fig.(2.4) Mode 3 Eigenvector for Discrete Mass Model

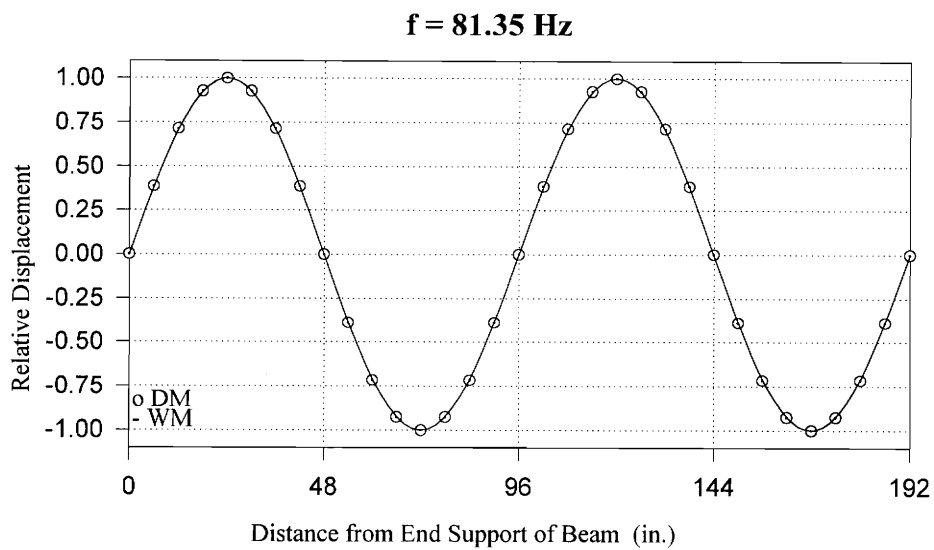


Fig.(2.5) Mode 4 Eigenvector for Discrete Mass Model

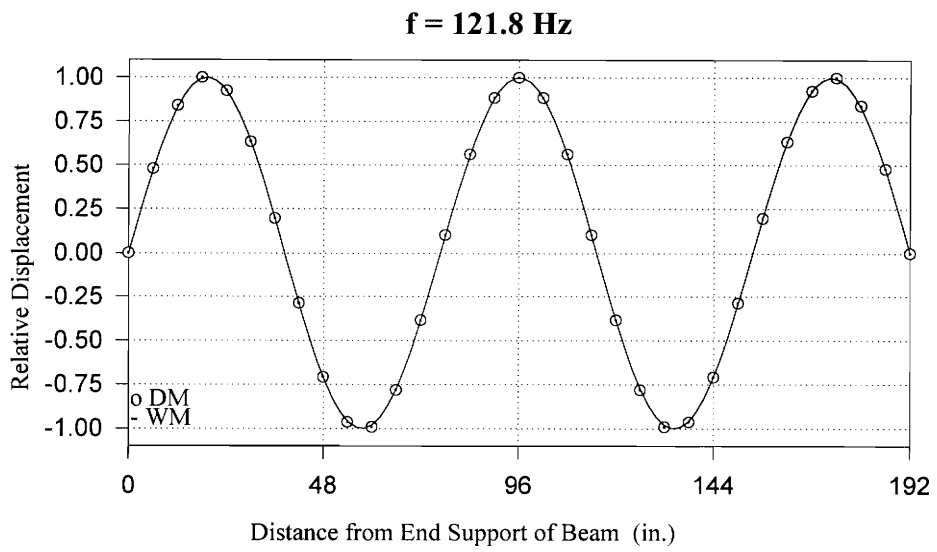


Fig.(2.6) Mode 5 Eigenvector for Discrete Mass Model

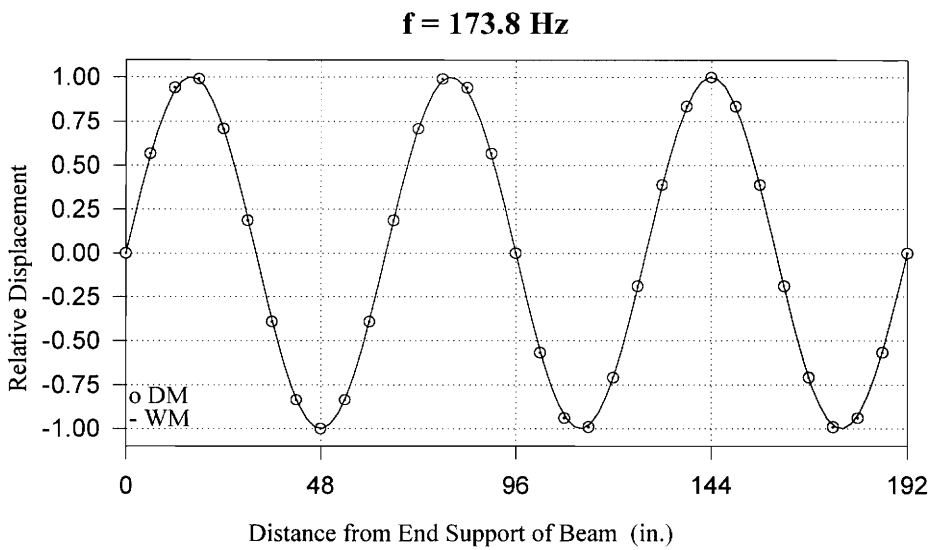


Fig.(2.7) Mode 6 Eigenvector for Discrete Mass Model

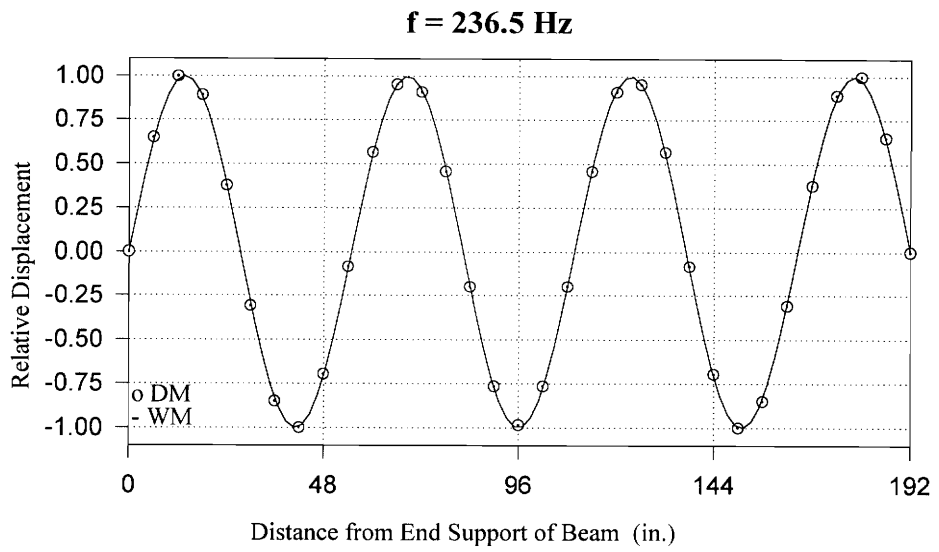


Fig.(2.8) Mode 7 Eigenvector for Discrete Mass Model

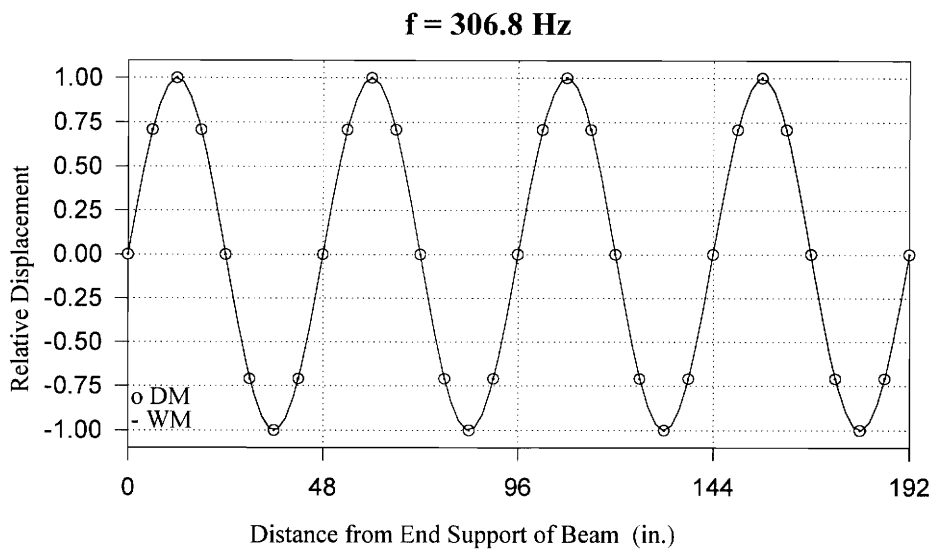


Fig.(2.9) Mode 8 Eigenvector for Discrete Mass Model

For the S4x7.7 section of Fig.(2.4) with an intermediate support stiffness of 2.7 kip/in. and axial load of 20 kips, the mode shapes of the first eight natural frequencies are plotted in Fig.(3.2) through Fig.(3.9). The model used divides the beam into 32 discrete beam elements. The mode shapes are plotted together with the sinusoidal mode shapes of the Winkler foundation model. The mode shapes of the two models are nearly identical.

3.5 Load and Stiffness Determination

If equations (3.1) and (3.2) are solved for a number of different axial loads, frequency vs. axial load curves can be plotted as in Fig.(3.10). For comparison, f vs. P is also plotted for the Winkler foundation model. For a support stiffness of 2.7 kip/in., the difference in the frequencies of the two models is very small except for the pinned-pinned mode. As expected, the frequencies for the pinned-pinned mode of vibration are the same as for the Winkler foundation frequencies when $K=0$ in equation (2.18).

If the frequency-load relationship is determined for a number of different support stiffnesses, then the frequency can be plotted versus both support stiffness and axial load as in Fig.(3.11) through Fig.(3.18). Each plot shows frequencies for a particular mode of vibration. A frequency of zero indicates buckling of the particular mode for the corresponding combination of P and k_s . Buckling of the beam occurs if any modal frequency for a particular combination of P and k_s is zero. Note again that the frequencies for the 8th mode of vibration are independent of k_s .

DM(-) and WM(--) Frequencies for Modes 1-8

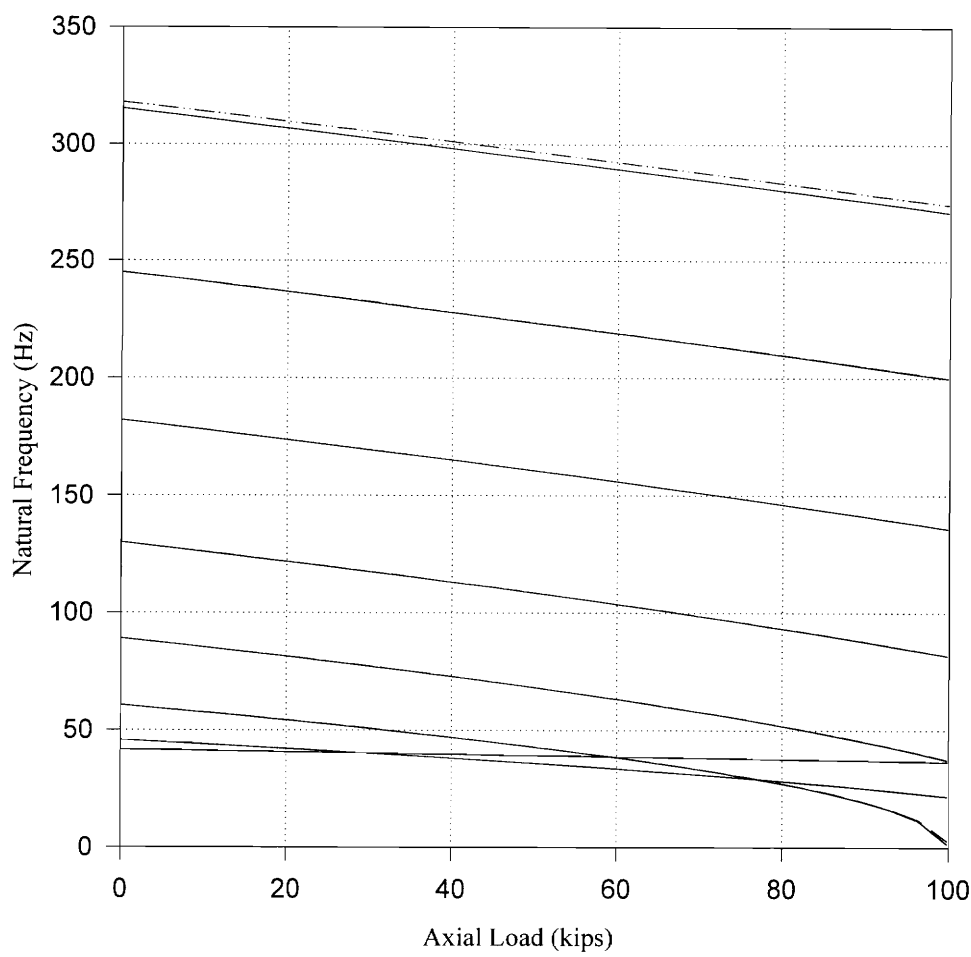


Fig.(3.10) Frequency vs. Axial Load for Discrete Model and Winkler Model

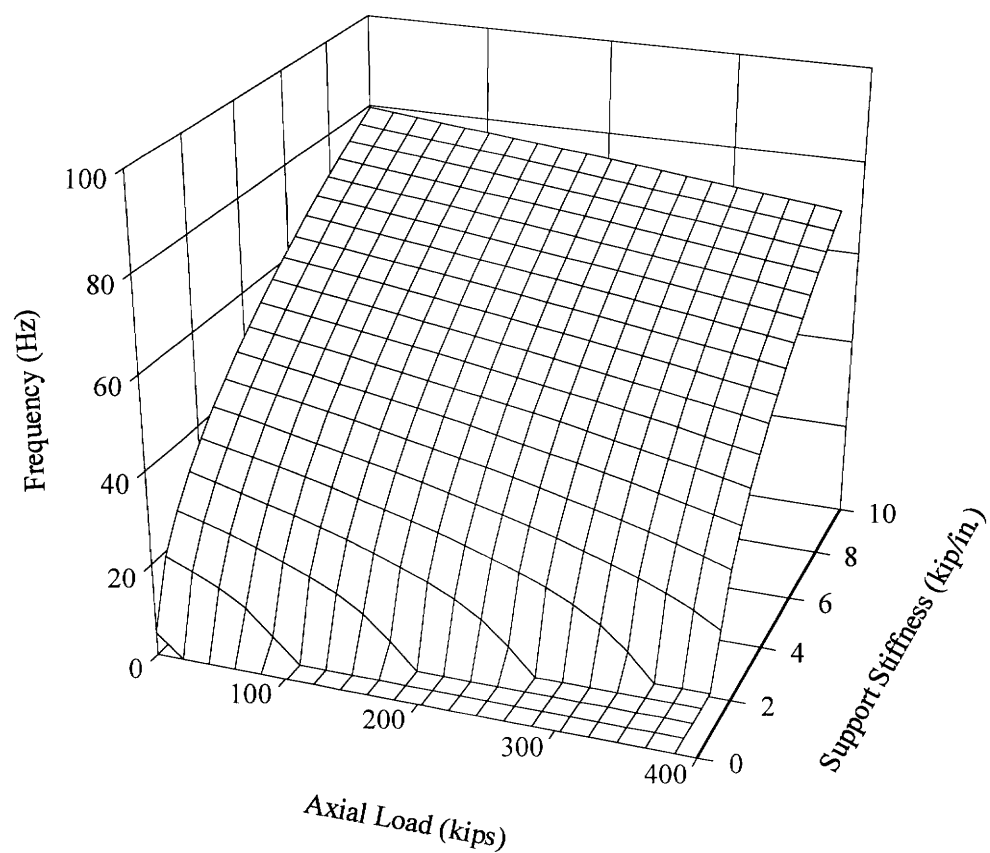


Fig.(3.11) Mode 1 Mesh Plot

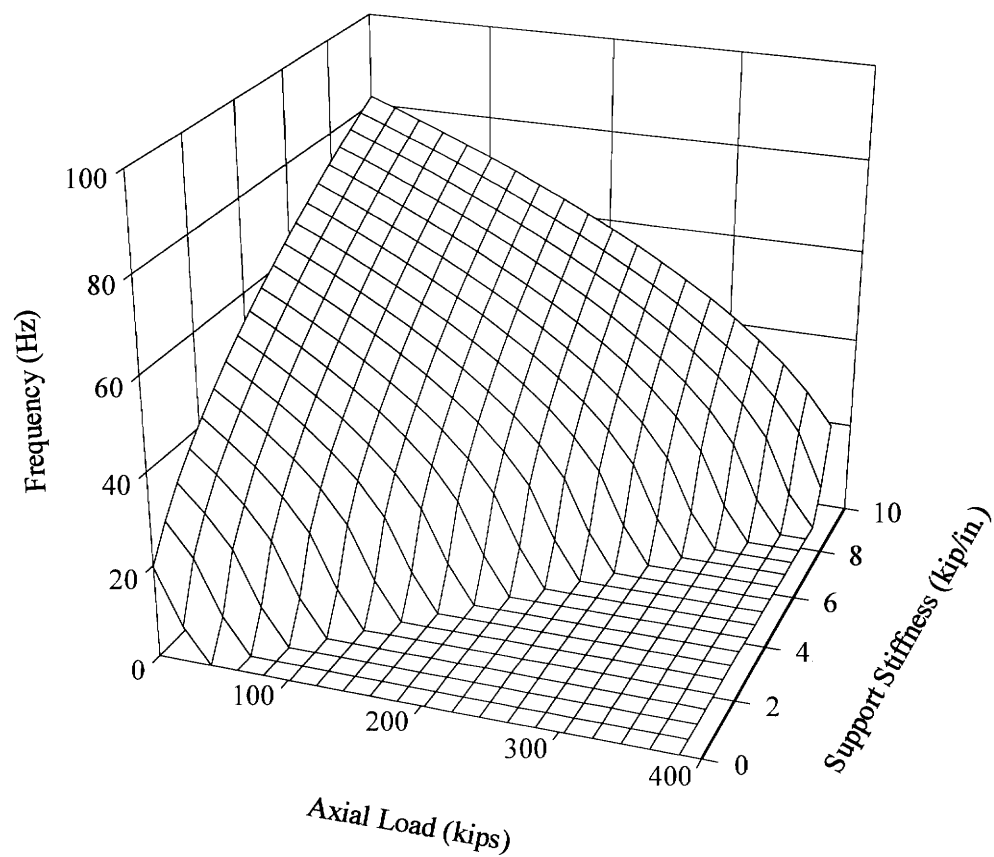


Fig.(3.12) Mode 2 Mesh Plot

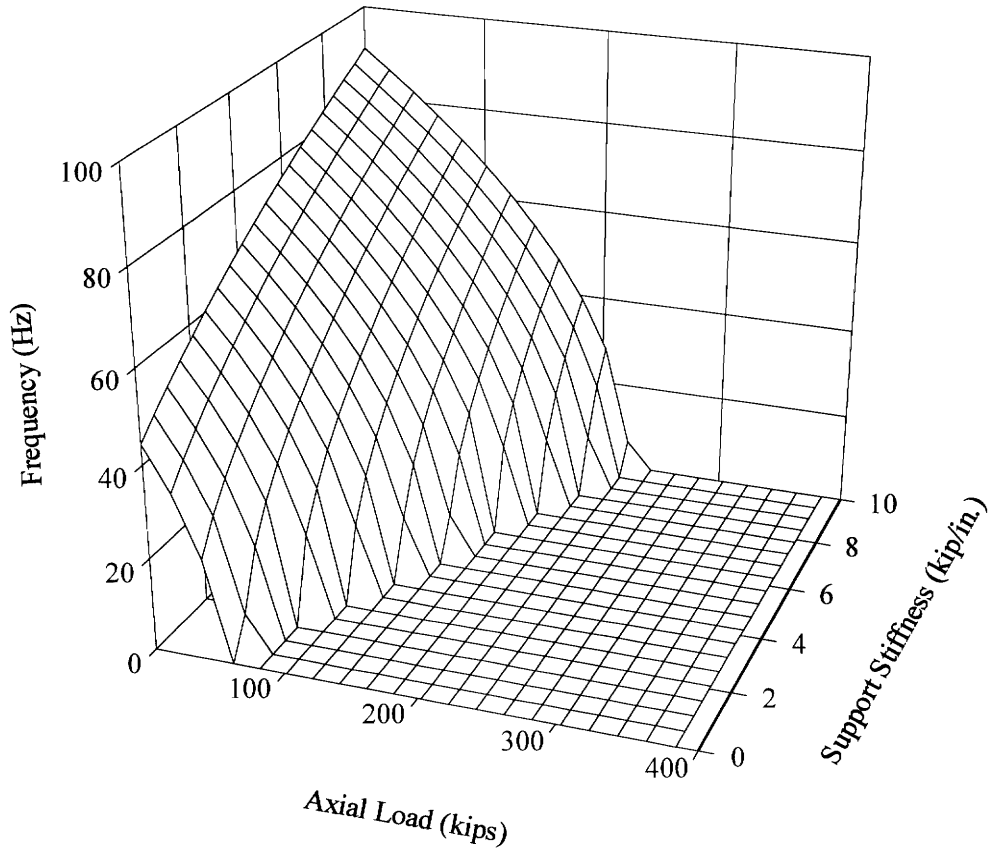


Fig.(3.13) Mode 3 Mesh Plot

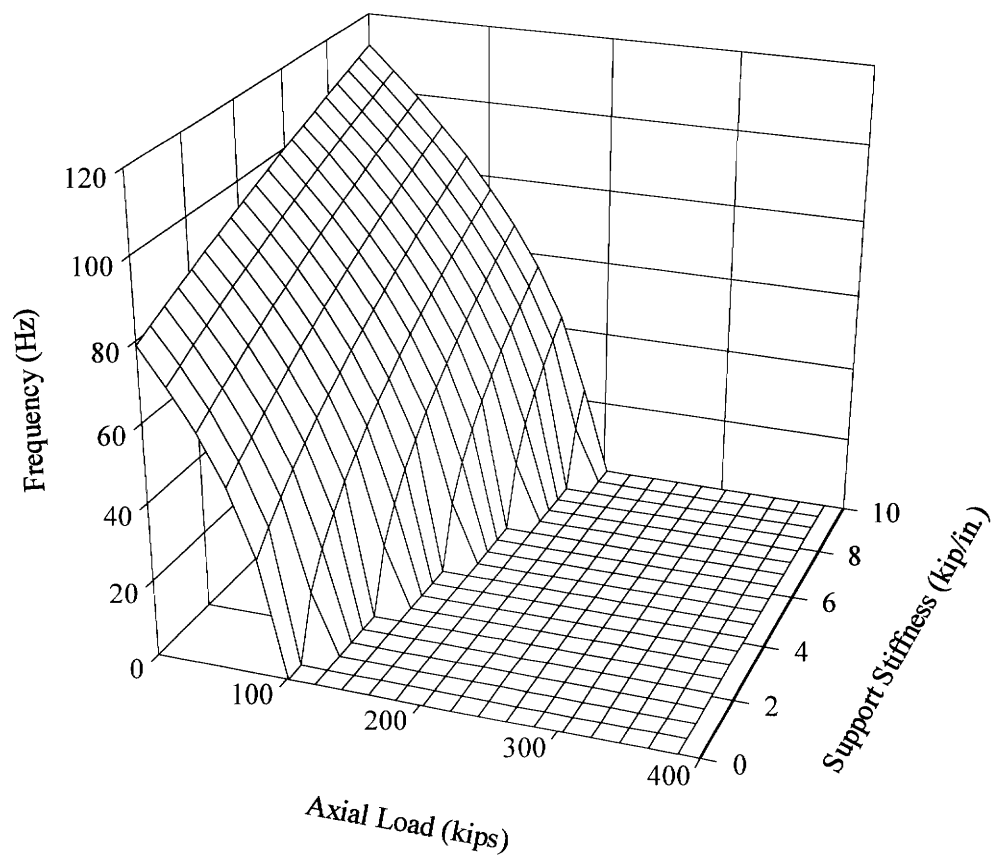


Fig.(3.14) Mode 4 Mesh Plot

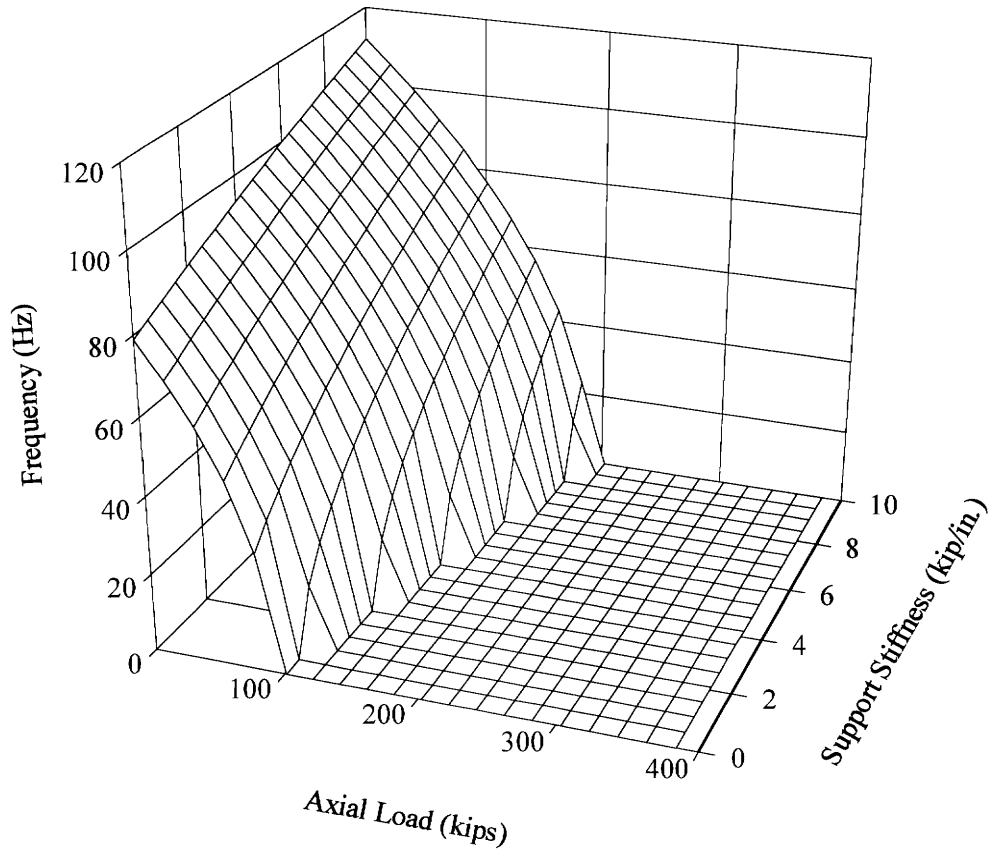


Fig.(3.15) Mode 5 Mesh Plot

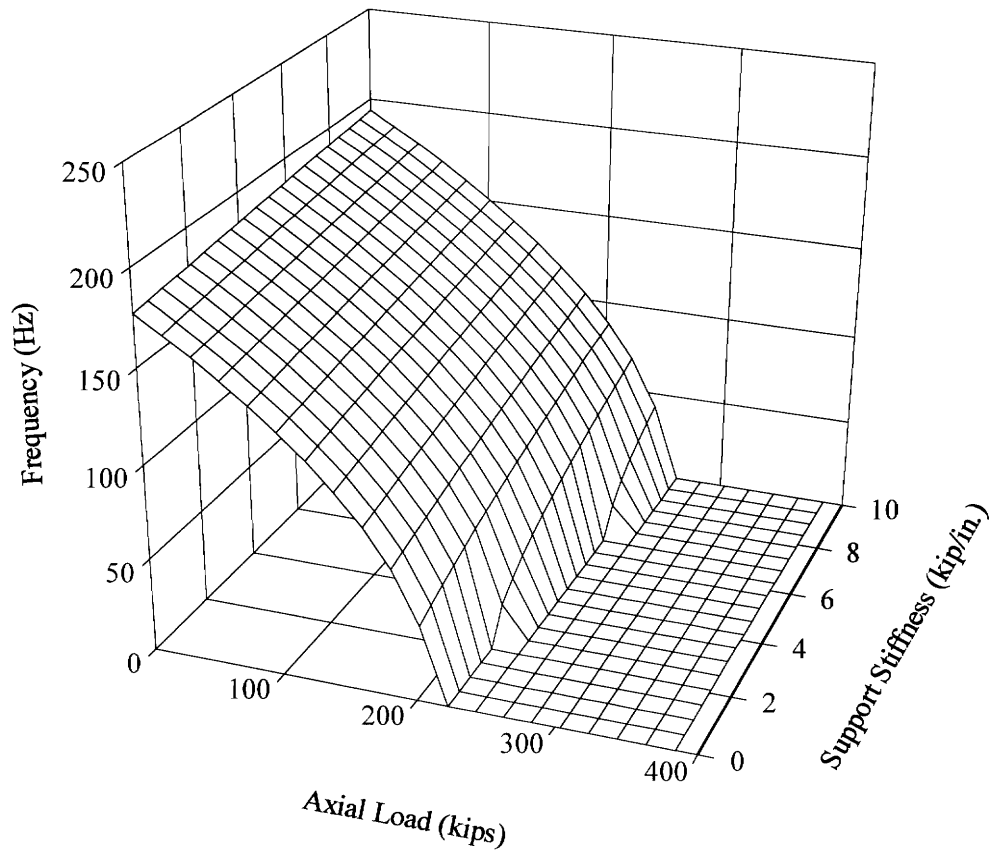


Fig.(3.16) Mode 6 Mesh Plot

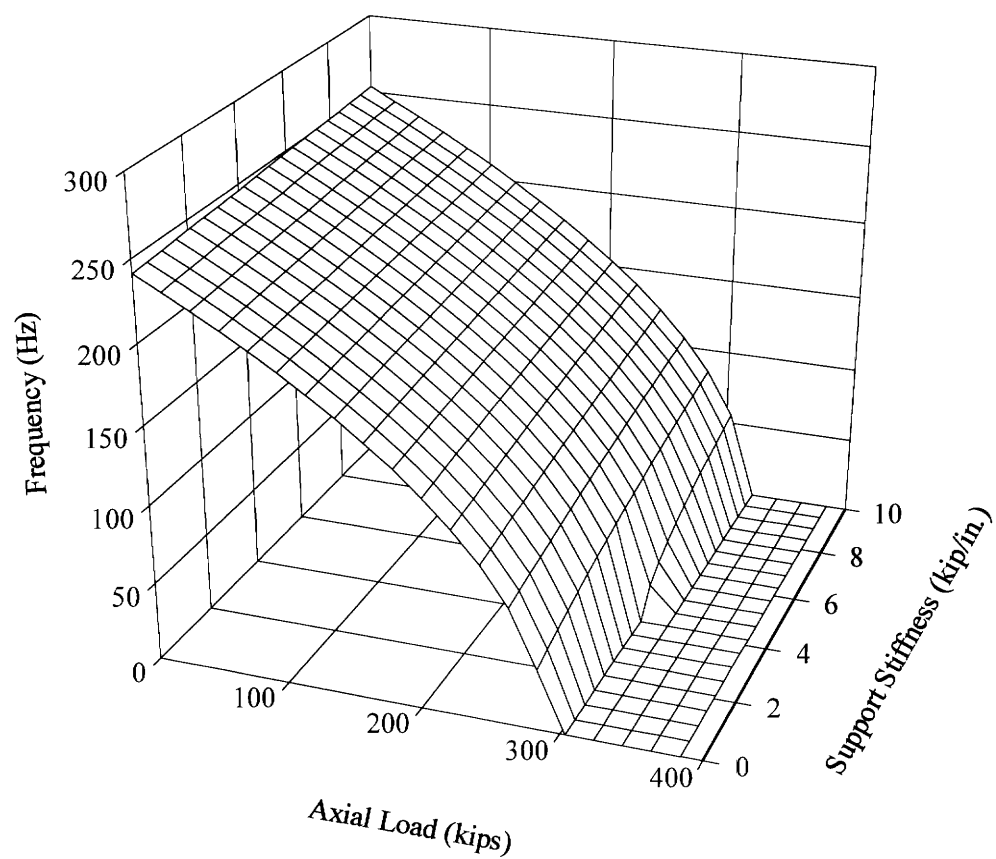


Fig.(3.17) Mode 7 Mesh Plot

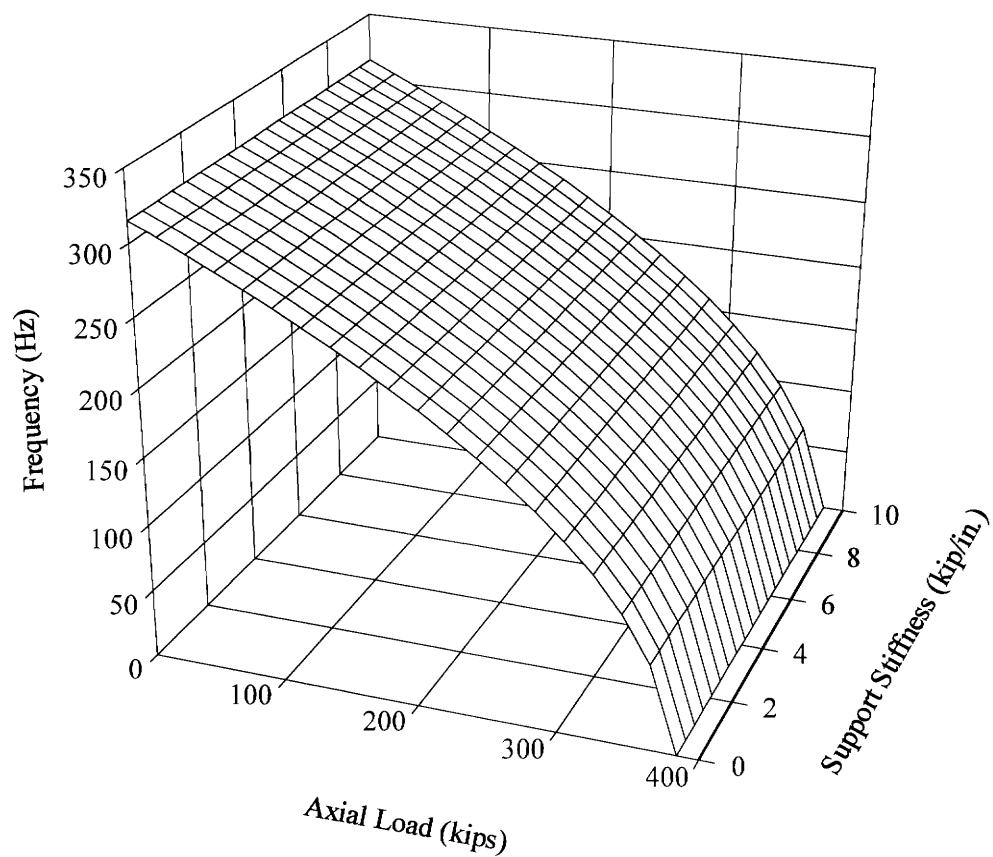


Fig.(3.18) Mode 8 Mesh Plot

For a beam with specific values of P and k_s , frequencies can be measured for the various modes. When the frequency corresponding to the first mode has been measured, Fig.(3.11) can be used to create a contour line which represents all combinations of P and k_s which would produce the measured frequency for the first mode. Similar contour lines for other measured modal frequencies can be superimposed on the same plot. For ideal measurement and interpolation, there will exist one point on the contour plot at which all the contour lines intersect. This point of intersection corresponds to the actual axial load and support stiffness of the beam. For example, suppose the S4x7.7 section of Fig.(2.4) has an intermediate support stiffness of 2.7 kip/in. and an axial load of 20 kips. The corresponding contour lines for modes 1 through 8 of the beam are shown in Fig.(3.19). As expected, the point of intersection of the contour lines corresponds to $P=20$ kips and $k_s=2.7$ kip/in..

Fig.(3.19) confirms the implication of the Winkler foundation model that lower modes are better for determining support stiffness whereas higher modes are better for determining axial load. For example, if a small error in measurement causes the contour line for mode 1 to be slightly displaced, then the intersection of modes 1 and 2 would result in a large error in the axial load; however, there would be a relatively small error in the support stiffness. On the other hand, a small displacement of the mode 8 contour line would cause the intersection of the mode 7 and mode 8 lines to give a large error in the support stiffness and a small error in the axial load.

Contour Lines for Modes 1-8

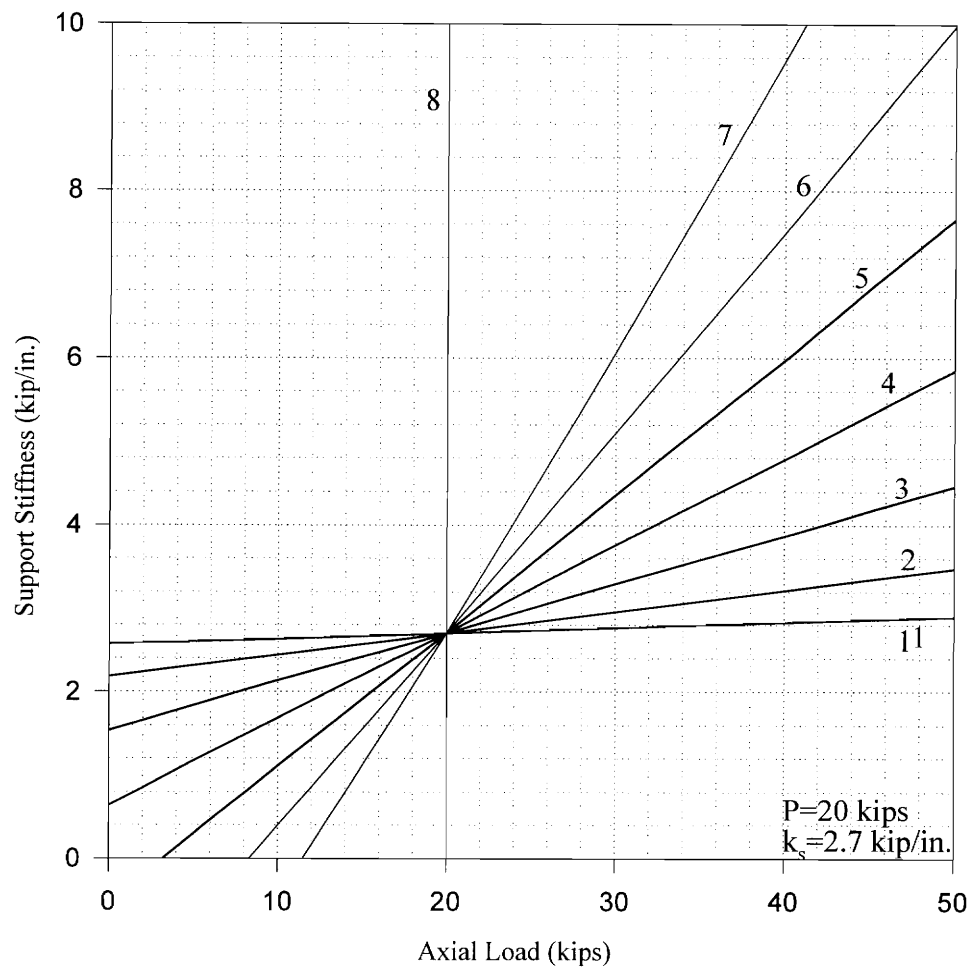


Fig.(3.19) Contour Plot for Load and Stiffness Determination

3.6 Effect of Shear and Rotatory Inertia

If the effects of shear deformation and rotatory inertia are considered, the vibration of a pinned-pinned beam subject to an axial load is given by

$$\omega_n = \Phi_n \cdot \left\{ \frac{1}{m} \left[EI \left(\frac{n\pi}{L} \right)^4 - P \left(\frac{n\pi}{L} \right)^2 \right] \right\}^{\frac{1}{2}} \quad (3.12)$$

where

$$\Phi_n = \left[1 + \left(\frac{n\pi r}{L} \right)^2 \left(1 + \frac{E}{k'G} \right) \right]^{-\frac{1}{2}} \quad (3.13)$$

is a frequency reduction factor which accounts for shear deformation and rotatory inertia (see Appendix A). In equation (3.13), n is the mode number of vibration, r is the radius of gyration of the beam section, G is the shear modulus, and k' is a shear factor dependent on the beam cross-section. The bracketed part of equation (3.12) represents the frequency of a pinned-pinned Bernoulli-Euler beam with an axial load (compare to equation (2.18) with $K=0$). As equation (3.13) indicates, the effect of shear and rotatory inertia increases with the mode number of vibration. Table (3.1) shows the effect for the weak axis vibration of a 16 ft. S4x7.7 with a 20 kip axial load. Values in the tables are based on a shear area factor of $k'=0.850$ (Cowper, 1966).

Solving equation (3.12) for P , letting $\Phi_n=1$, and differentiating with respect to ω_n gives

$$\frac{\partial P}{\partial \omega_n} = -2 \left(\frac{L}{n\pi} \right)^2 m \omega_n \quad (3.14)$$

Table (3.1) Error in Frequency and Predicted Load due to Shear and Rotatory Inertia

Mode	Euler Freq. (Hz)	Φ_n	Δf (Hz)	ΔP (kips)
2	7.804	0.999	-0.006	0.01
3	35.04	0.998	-0.058	0.11
4	69.97	0.997	-0.204	0.44
5	114.5	0.995	-0.521	1.17
6	168.7	0.993	-1.10	2.53
7	232.8	0.991	-2.06	4.81
8	306.6	0.988	-3.54	8.32

Using the Euler beam frequency given for mode 8 in Table (3.1), equation (3.14) gives

$$\frac{\partial P}{\partial \omega_8} = -0.375 \frac{\text{kip}}{\text{rad}} = -2.35 \frac{\text{kip}}{\text{Hz}} \quad (3.15)$$

If shear and rotatory inertia are not considered, then based on Table (3.1) and equation (3.15), an axial load predicted from the 8th mode frequency using Euler beam theory will have a corresponding error of

$$\Delta P = -\Delta f \cdot \frac{\partial P}{\partial \omega_8} = -(-3.54)(-2.35) = 8.32 \text{ kips} \quad (3.16)$$

The error is significant considering that the applied load was only 20 kips. The error due to shear deformation and rotatory inertia decreases with decreasing mode number as is indicated in Table (3.1); however, this should not be interpreted as an indication that lower modes are better for predicting axial load. Since the frequencies of the lower

modes are less sensitive to axial load, other errors associated with their measurement will cause significant errors in axial load predictions.

Since the 8th mode of vibration is unaffected by the intermediate supports, it behaves the same as the 8th mode of a pinned-pinned beam. Thus, the frequencies of this mode can be corrected for shear and rotatory inertia simply by multiplying by Φ_8 . The mode 6 and mode 7 frequencies are affected by the presence of the intermediate supports; however, since the effect is small (see Fig.(3.16) and Fig.(3.17)), it is a reasonable approximation for many cases to also modify these higher frequencies by Φ_n .

Chapter 4

Continuous Model of Finite Beam on Elastic Supports

A general equation of motion can be derived for a beam subject to axial load with arbitrary end conditions. With the use of boundary conditions, an exact model can be formulated for a finite Bernoulli-Euler beam on elastic supports. By using a general equation of motion for the section of the continuous beam between each pair of supports and by applying the appropriate boundary conditions, a set of equations can be determined which exactly describes the mode shapes of the beam.

4.1 General Equation of Motion

Considering a differential segment of a beam similar to that of Fig.(2.2) without the presence of an elastic foundation, summation of moments and vertical forces and use

of $M = EI \frac{\partial^2 v}{\partial x^2}$ leads to the following equations:

$$V = EI \frac{\partial^3 v}{\partial x^3} + P \frac{\partial v}{\partial x} \quad (4.1)$$

$$m \frac{\partial^2 v}{\partial t^2} + EI \frac{\partial^4 v}{\partial x^4} + P \frac{\partial^2 v}{\partial x^2} = 0 \quad (4.2)$$

If a displacement of the form

$$v(x, t) = A \cdot \exp(i\omega t + \Lambda x) \quad (4.3)$$

is assumed, where $i = \sqrt{-1}$, then equation (4.2) gives

$$[-m\omega^2 + EI\Lambda^4 + P\Lambda^2]A \cdot \exp(i\omega t + \Lambda x) = 0 \quad (4.4)$$

Using the quadratic equation and solving for Λ^2 gives

$$\Lambda^2 = \frac{1}{2EI} \left(-P \pm \sqrt{P^2 + 4mEI\omega^2} \right) \quad (4.5)$$

This allows four possible roots for Λ :

$$\begin{aligned} \Lambda_{1,2} &= \pm \sqrt{\frac{1}{2EI} \left(-P + \sqrt{P^2 + 4mEI\omega^2} \right)} \\ \Lambda_{3,4} &= \pm \sqrt{\frac{1}{2EI} \left(-P - \sqrt{P^2 + 4mEI\omega^2} \right)} \end{aligned} \quad (4.6)$$

Taking into account all four roots of Λ , v can be written in a general form as

$$v_i(x, t) = [A_i \exp(\Lambda_1 x) + B_i \exp(\Lambda_2 x) + C_i \exp(\Lambda_3 x) + D_i \exp(\Lambda_4 x)] \exp(i\omega t) \quad (4.7)$$

where the subscript i signifies the i th segment of the beam and A_i, B_i, C_i , and D_i are constants to be determined by boundary conditions. The coordinate x is measured from the left end support of the beam.

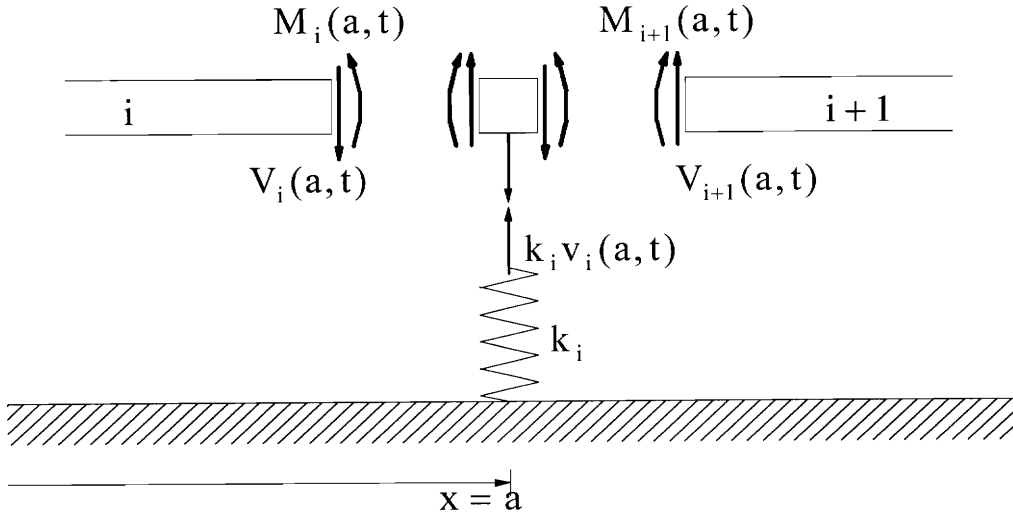


Fig.(4.1) Free Body Diagram of Beam Segment at an Intermediate Support

4.2 Characteristic Matrix

At an interior support, as in Fig.(4.1), four boundary conditions can be imposed:

$$1) \quad v_i(a, t) - v_{i+1}(a, t) = 0 \quad (4.8a)$$

$$2) \quad \left. \frac{\partial v_i}{\partial x} \right|_{x=a} - \left. \frac{\partial v_{i+1}}{\partial x} \right|_{x=a} = 0 \quad (4.8b)$$

$$3) \quad V_i(a, t) - V_{i+1}(a, t) - k_i v_i(a, t) = 0 \quad (4.8c)$$

$$\text{where } V = EI \frac{\partial^3 v}{\partial x^3} + P \frac{\partial v}{\partial x}$$

$$4) \quad M_i(a, t) - M_{i+1}(a, t) = 0 \quad (4.8d)$$

$$\text{where } M = EI \frac{\partial^2 v}{\partial x^2}$$

If end supports are also modeled as springs, shear and moment boundary conditions can be imposed at each end support. If end supports are modeled as pinned supports, displacement and moment boundary conditions can be imposed.

If there are a total of s supports on the beam, there will be $n=s-1$ beam segments along the length of the beam. By applying four boundary conditions at each intermediate support and two at each end support, there will be a total of $4n$ equations of compatibility. These equations of compatibility can be arranged in matrix form as

$$\mathbf{CM} \cdot \mathbf{C} = \mathbf{0} \quad (4.9)$$

where

$$\mathbf{C}^T = \{A_1 \quad B_1 \quad C_1 \quad D_1 \quad A_2 \quad B_2 \quad C_2 \quad \bullet \quad \bullet \quad \bullet \quad B_n \quad C_n \quad D_n \quad (4.10)$$

\mathbf{C} is the matrix of coefficients and \mathbf{CM} is the $4n$ by $4n$ characteristic matrix of the system.

4.3 Natural Frequencies and Mode Shapes

Equation (4.9) is satisfied when $\mathbf{C}=\mathbf{0}$ or

$$\det(\mathbf{CM}) = 0 \quad (4.11)$$

If all beam and support properties are known and the applied axial load is specified, then \mathbf{CM} is a function only of ω . Each natural frequency of the system, ω_n , is a value of ω for which equation (4.11) is satisfied. Thus, natural frequencies of the beam can be determined through an iterative process by calculating $\det(\mathbf{CM})$ for incremental values of ω until equation (4.11) is satisfied. Unlike the discrete mass model, the continuous

beam model yields an infinite number of eigenfrequencies and is limited only by the limits of Bernoulli-Euler beam theory.

For each natural frequency, the corresponding mode shape is determined by solving equation (4.9) for \mathbf{C} . Similar to the eigenvalue solution of the discrete mass model, the constants of \mathbf{C} are only defined relative to each other. By assuming a value for one constant, the corresponding values of the other constants can then be determined. Once the constants have been determined, each consecutive set of four constants will describe the mode shape of the beam over a corresponding beam segment, using equation (4.7).

The first 8 mode shapes of the S4x7.7 section of Fig.(2.4) with 2.7 kip/in. intermediate supports and a 20 kip axial load are plotted in Fig.(4.2) through Fig.(4.9) along with the discrete mass model and Winkler foundation model mode shapes. The mode shapes of the continuous model are nearly identical to the sinusoidal mode shapes of the Winkler foundation model.

The predicted frequencies of the continuous beam model are compared to the discrete mass model in Fig.(4.10) for various axial loads. For the parameters and modes chosen for the plot, the frequencies of the two models are in excellent agreement. The maximum discrepancy is approximately 0.1 Hz, which occurs for the 8th mode with low axial load. The discrepancy decreases with decreasing mode number and with increasing axial load.

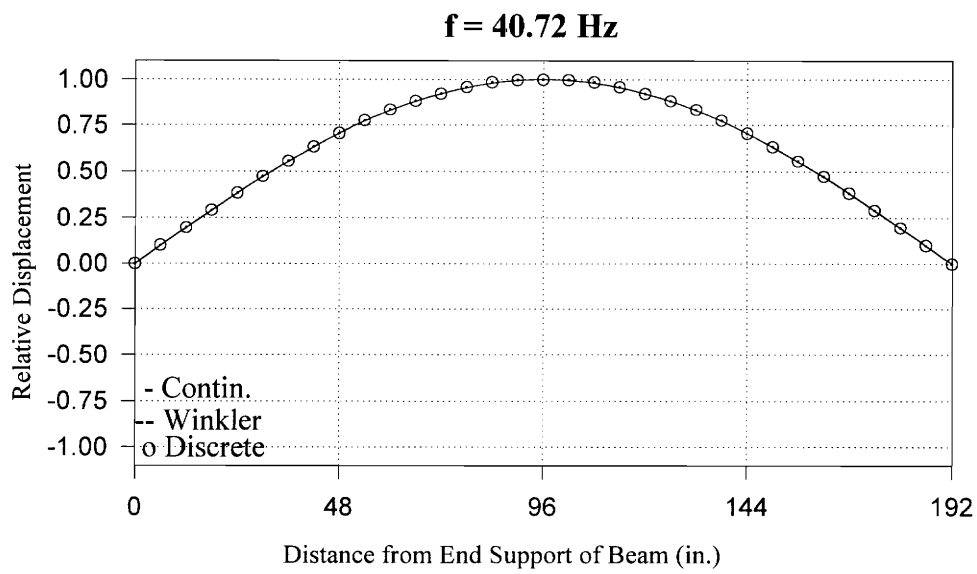


Fig.(4.2) Mode 1 Shape for Continuous, Discrete, and Winkler Model

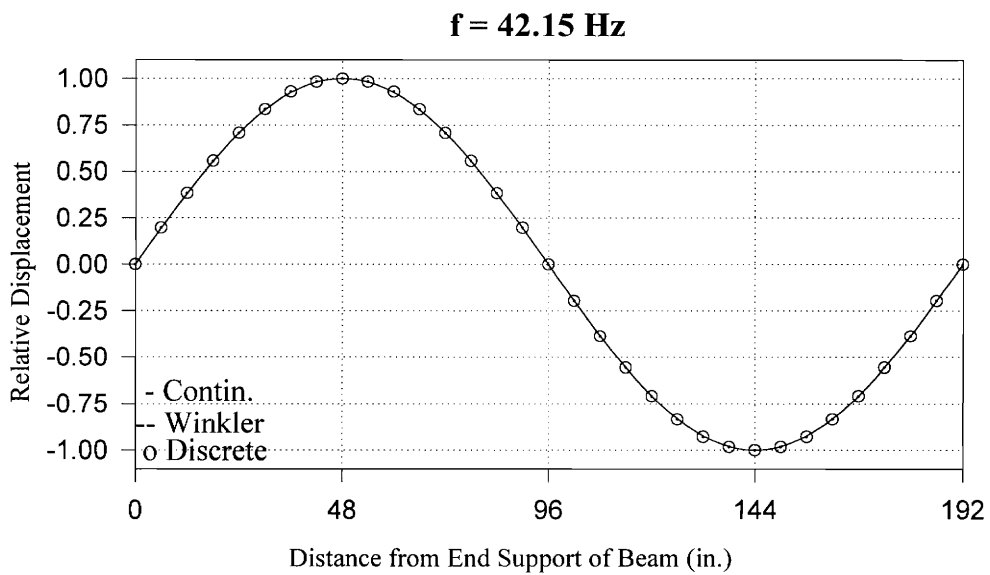


Fig.(4.3) Mode 2 Shape for Continuous, Discrete, and Winkler Model

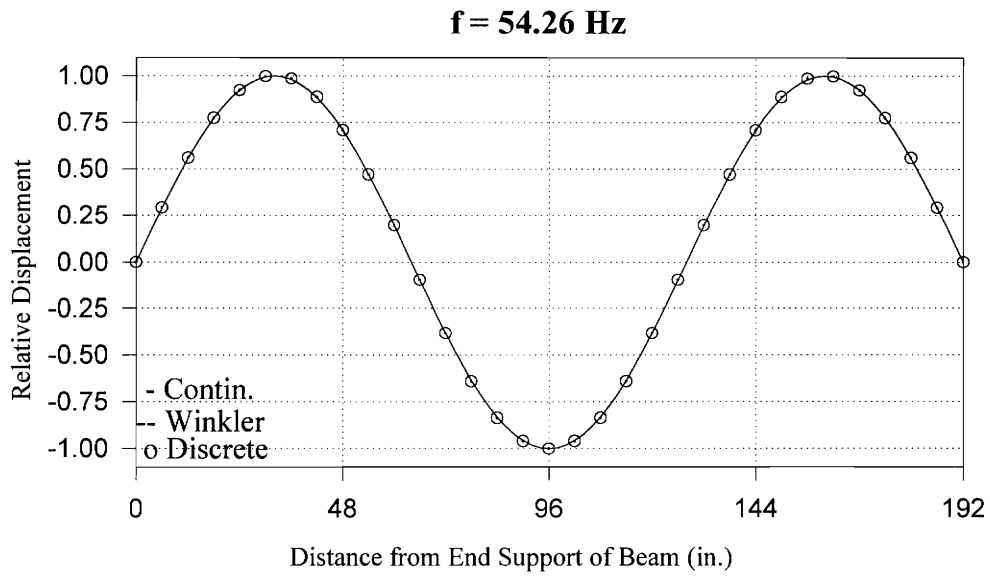


Fig.(4.4) Mode 3 Shape for Continuous, Discrete, and Winkler Model

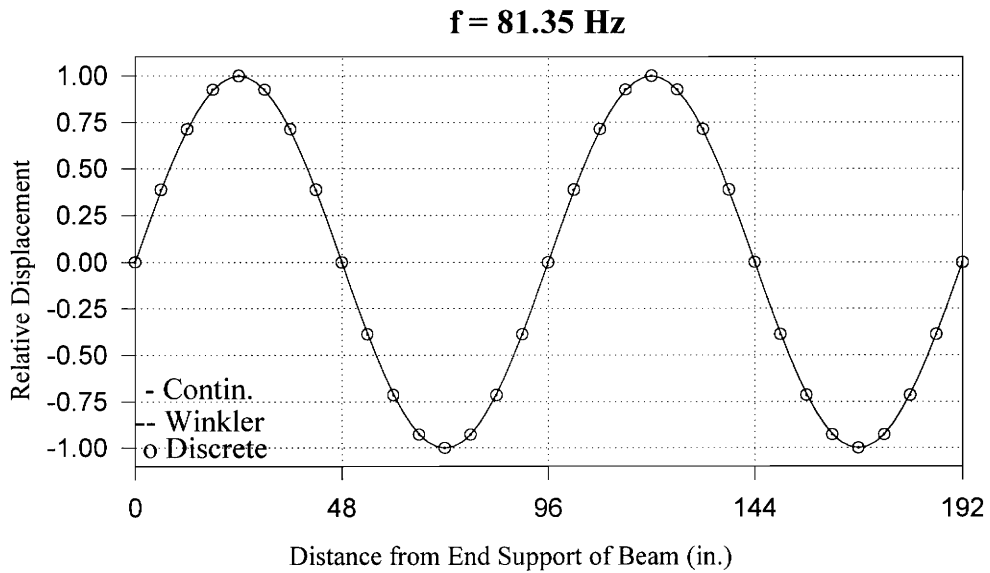


Fig.(4.5) Mode 4 Shape for Continuous, Discrete, and Winkler Model

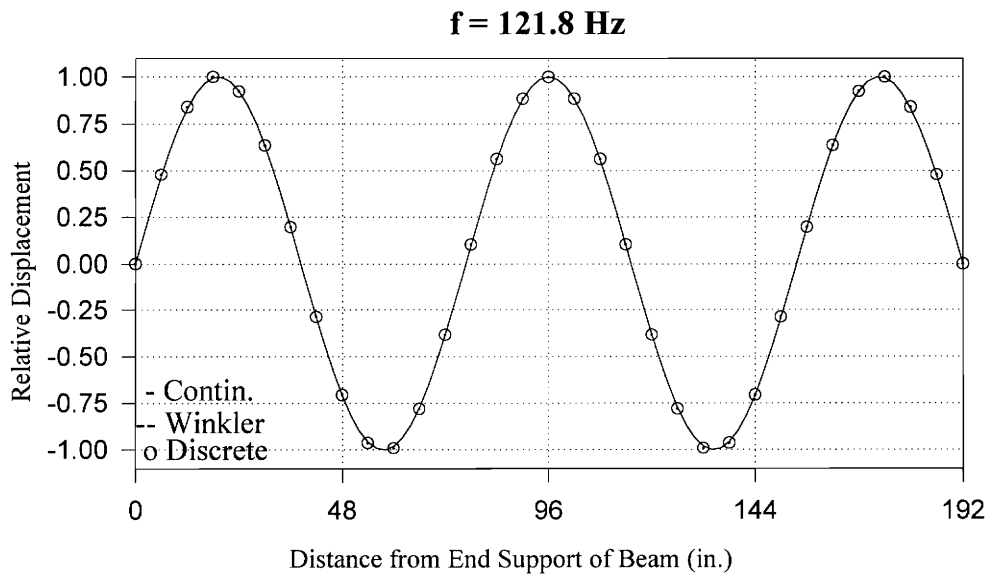


Fig.(4.6) Mode 5 Shape for Continuous, Discrete, and Winkler Model

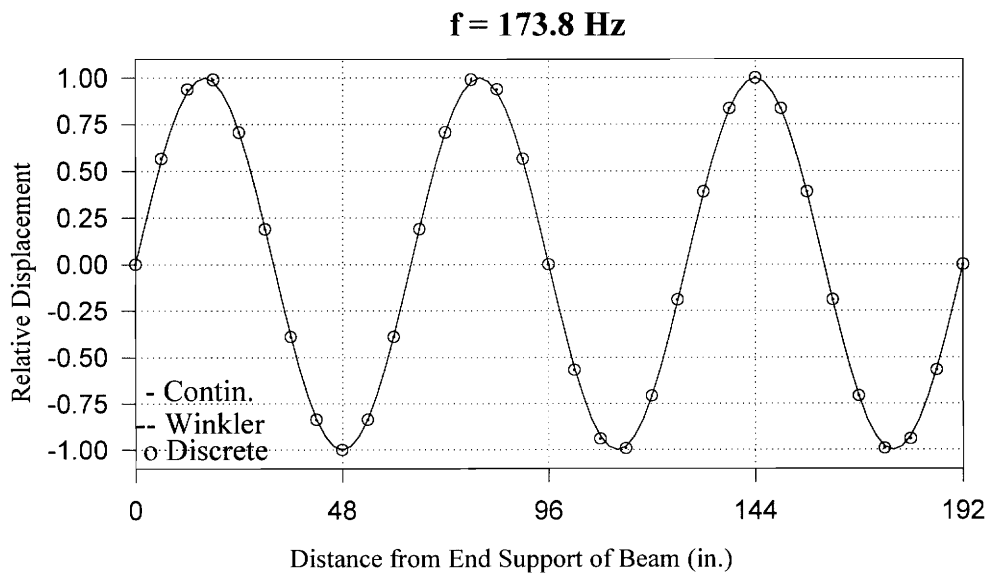


Fig.(4.7) Mode 6 Shape for Continuous, Discrete, and Winkler Model

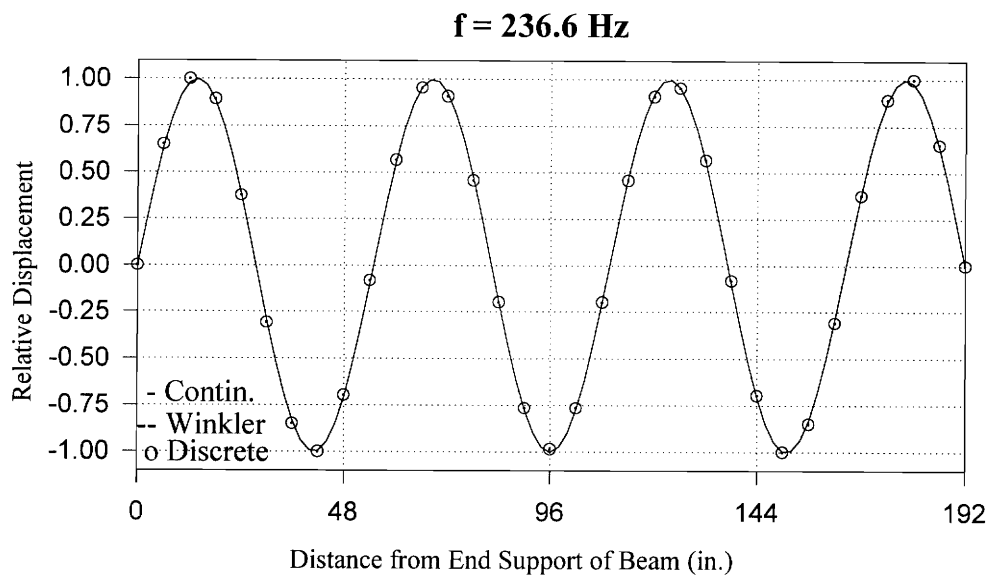


Fig.(4.8) Mode 7 Shape for Continuous, Discrete, and Winkler Model

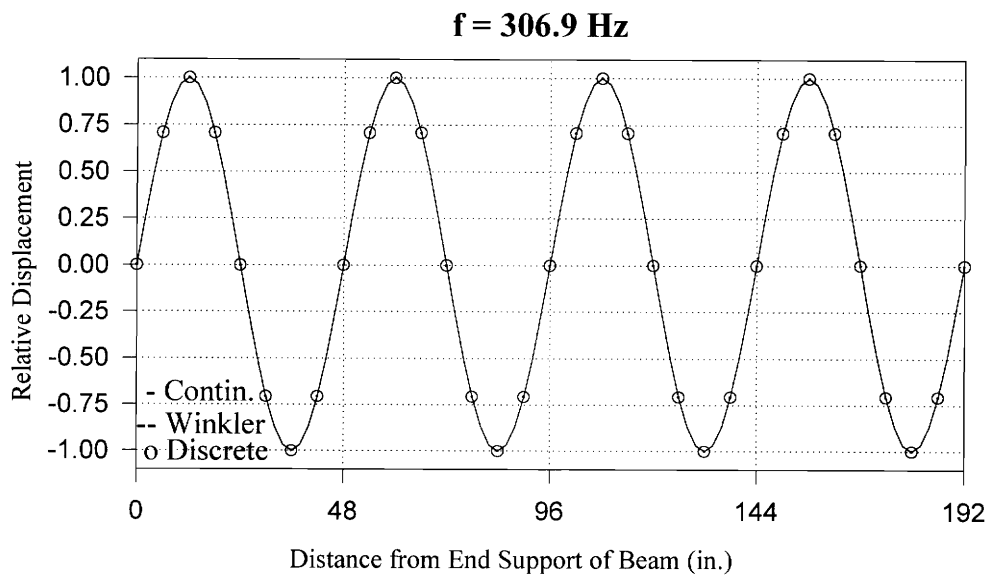


Fig.(4.9) Mode 8 Shape for Continuous, Discrete, and Winkler Model

CM(-) and DM(--) Frequencies for Modes 1-8

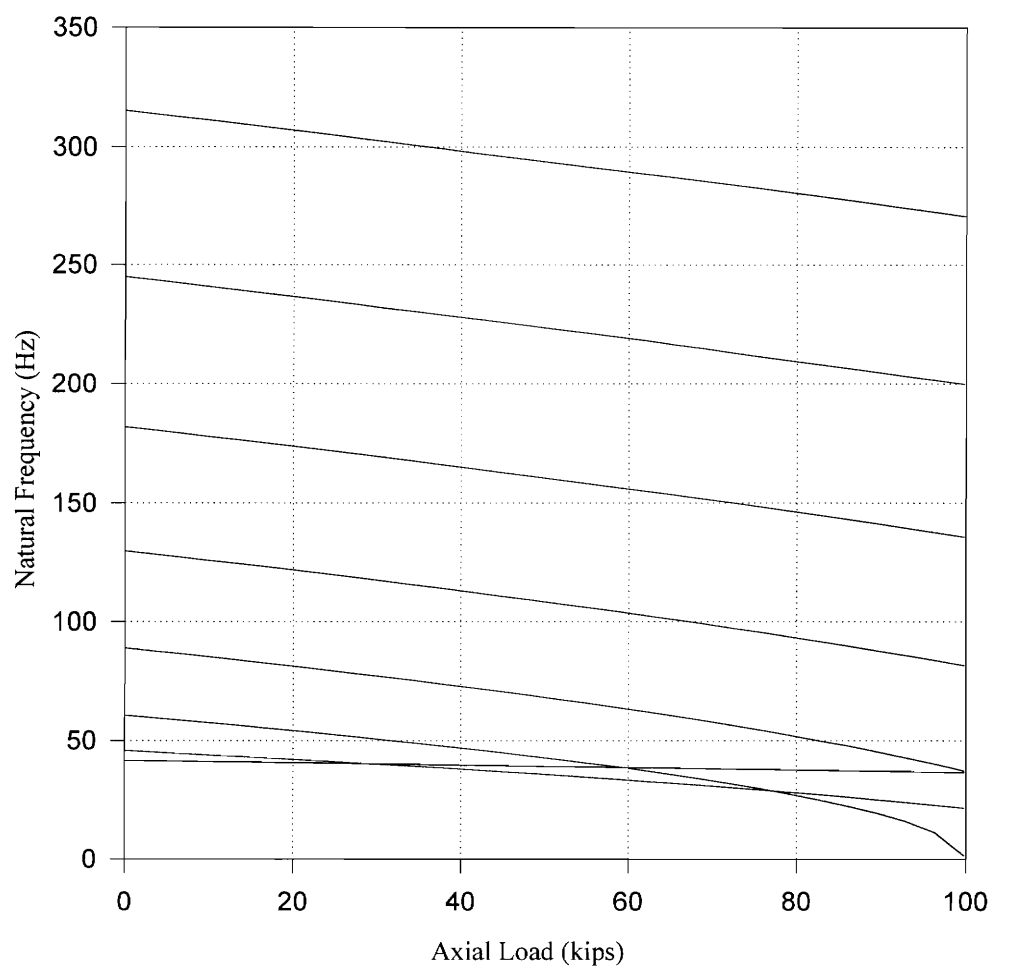


Fig.(4.10) Frequency vs. Axial Load for Continuous Model and Discrete Model

The frequencies and mode shapes predicted by the continuous model and the discrete model are in close agreement. By determining the continuous beam model frequencies for various axial loads and intermediate support stiffnesses, the load and stiffness of an actual beam can be predicted in the same manner as for the discrete mass model (Chapter 3). Given the agreement of the two models, the axial load and lateral stiffness predicted by the two models will be nearly the same.

Chapter 5

Experiment and Analysis

5.1 Introduction

Modal impact tests were performed on a 16 ft. S4x7.7 section to determine mode shapes and natural frequencies for various axial loads. The beam was supported by two end supports and seven elastic intermediate supports spaced evenly at 2 ft. intervals along the length of the beam. The beam was excited with an impact hammer equipped with a load transducer and the vibration of the beam was measured with an accelerometer. Hammer and accelerometer measurements were used to determine the frequency response of the beam.

The objective of the tests was to verify the frequency-load relationships and mode shapes predicted by the analytical models. A second objective was to estimate the applied axial load and support stiffness based on modal data and to compare the estimates to the actual values.

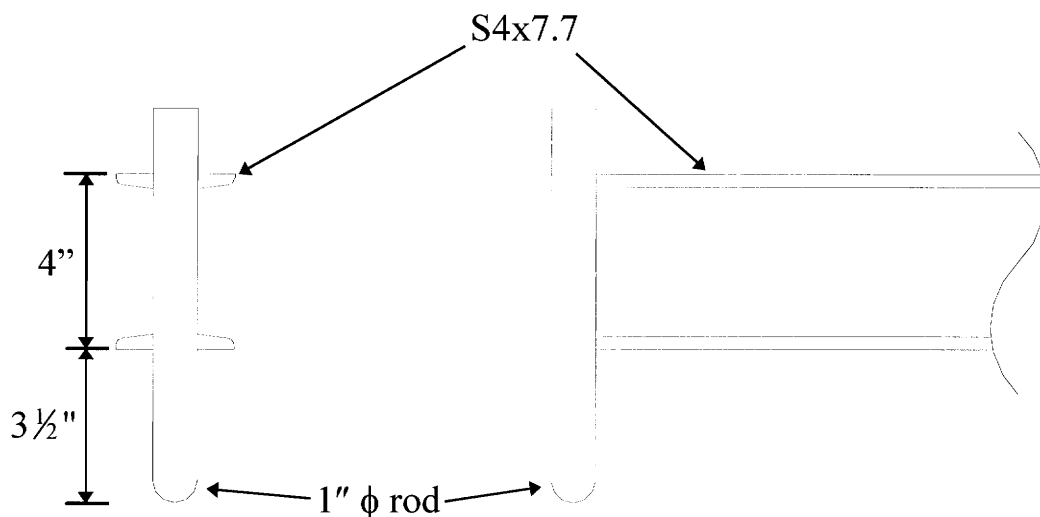


Fig.(5.1) End of Test Beam

1.2 Test Setup

The specimen tested was a 16ft A36 steel S4x7.7 section with 1 in. diameter steel rods welded along the web at each end (Fig.(5.1)). The rods were rounded on one end to provide minimal friction due to gravity loading against the reaction floor. Each of the rods was supported by two thrust bearings - one below the bottom flange and the other above the top flange of the beam. The thrust bearings were used to allow the application of axial load with minimal moment resistance at the end supports of the beam. Figs. (5.2) and (5.3) show the two end supports of the beam. All supports were bolted to the top flange of a reaction beam which is embedded in a concrete floor slab. Bolts were wedged

Section A-A

Section B-B

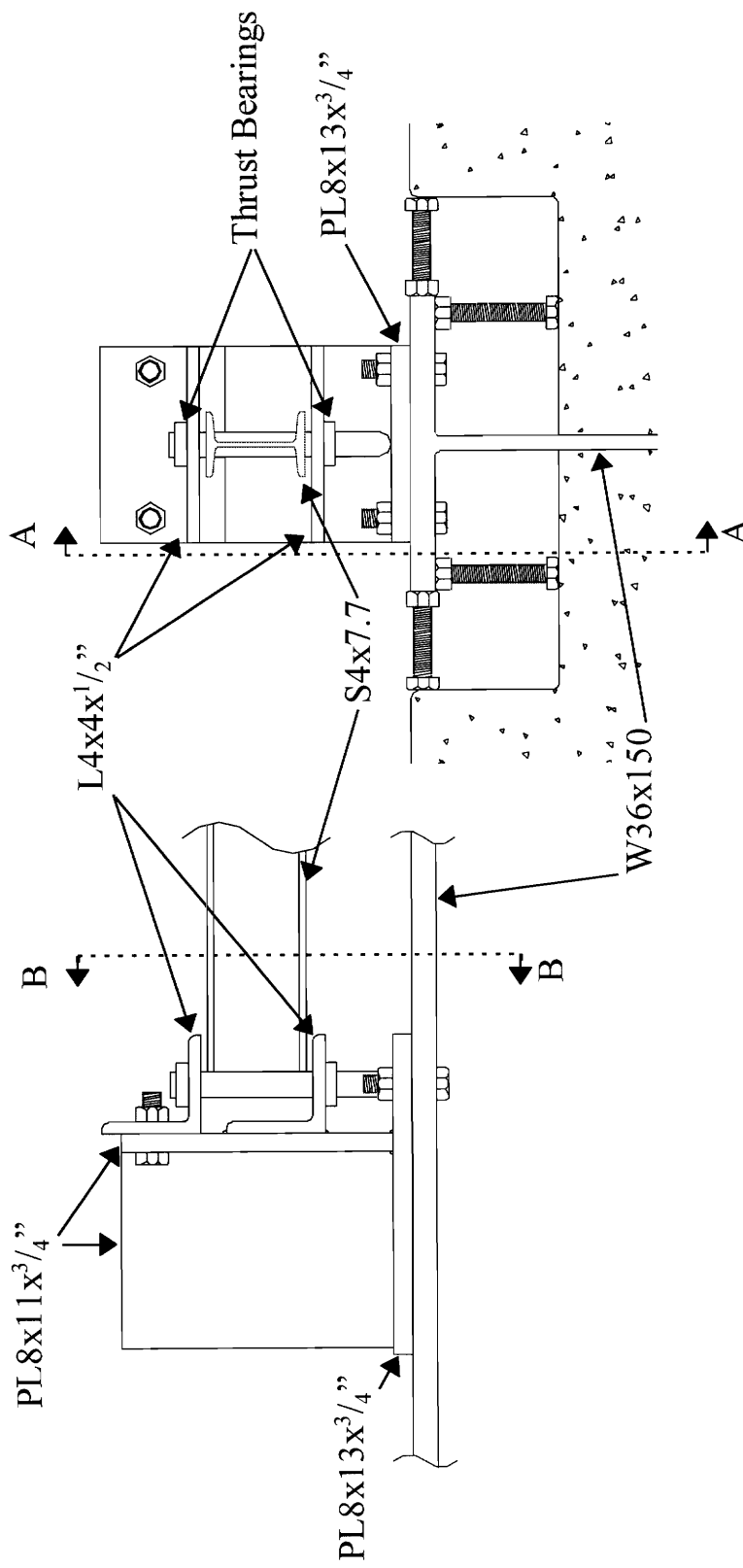


Fig.(5.2) Left End Support

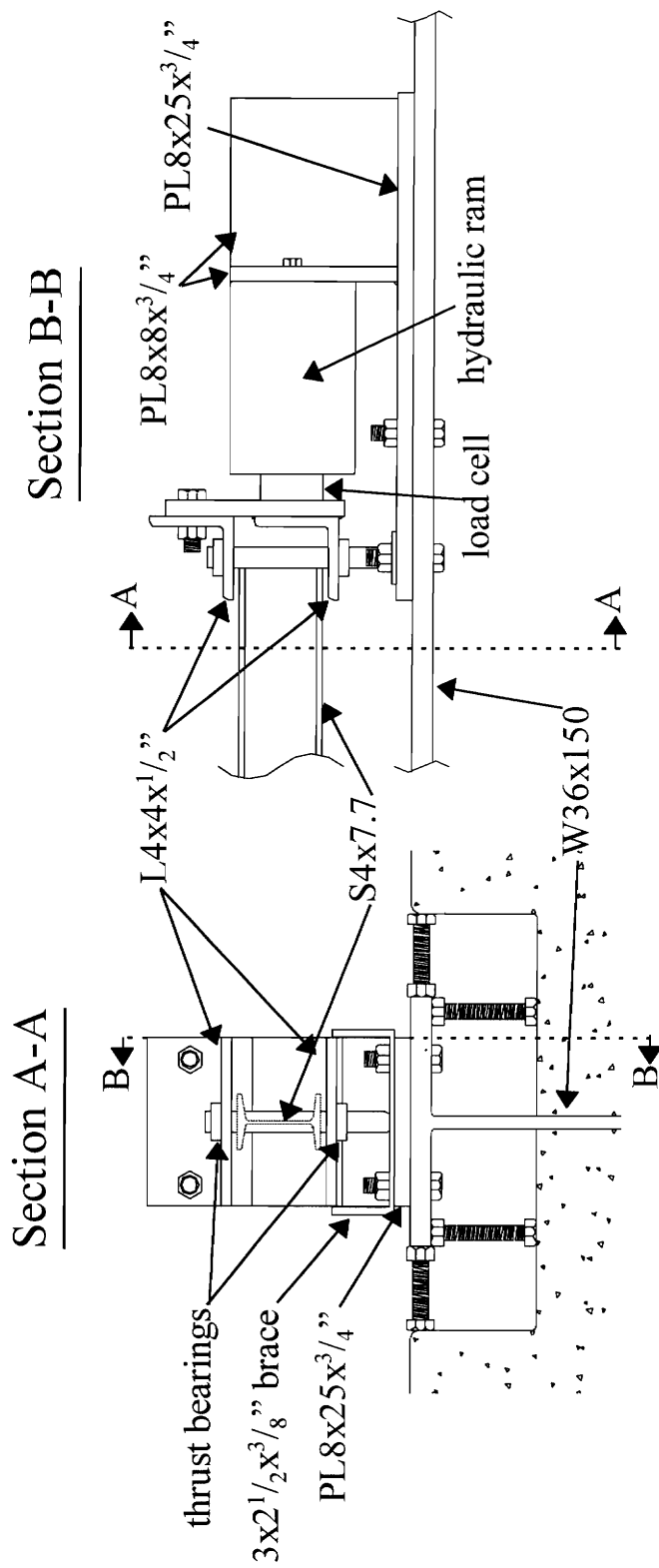


Fig.(5.3) Right End Support

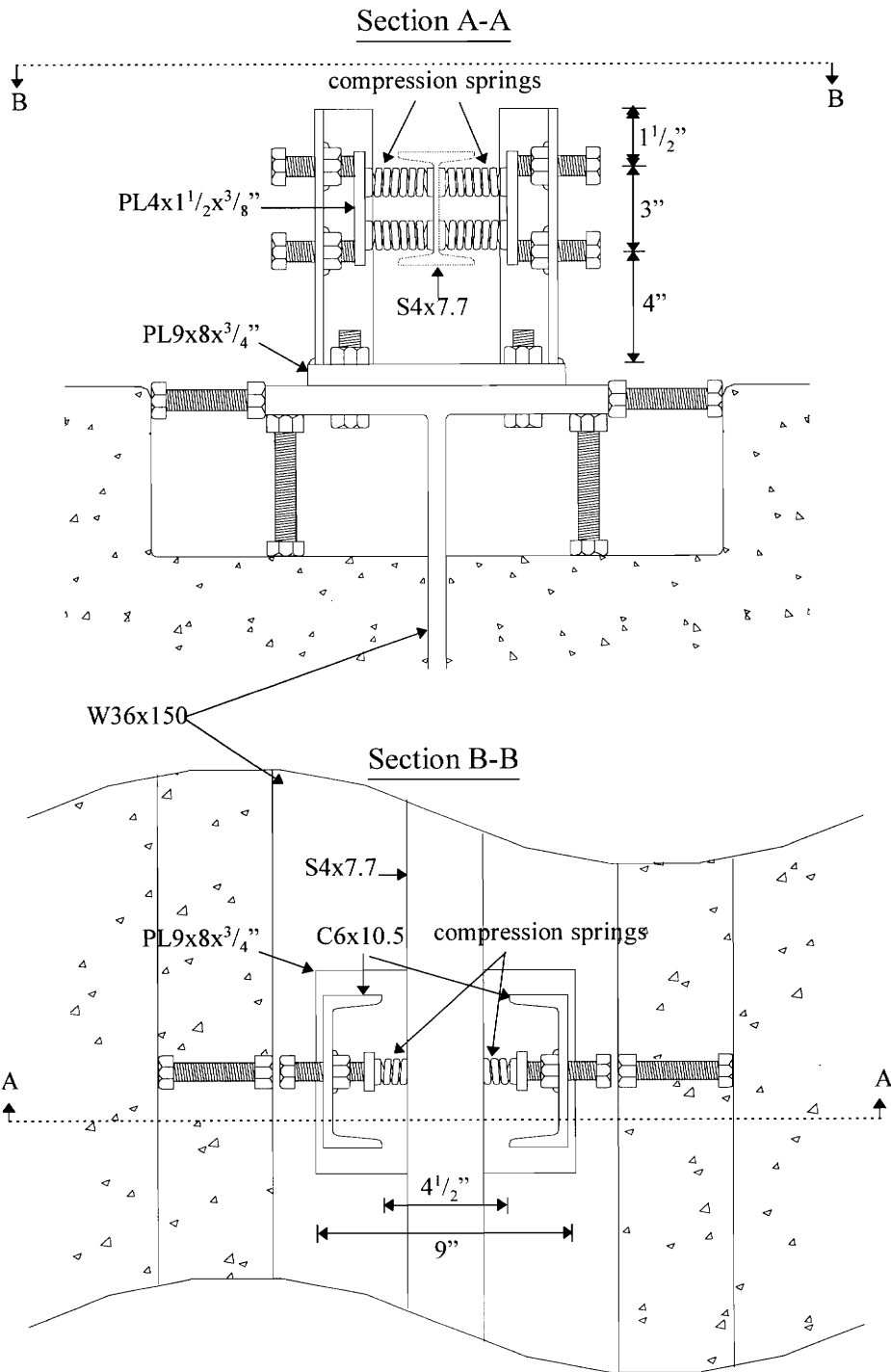


Fig.(5.4) Intermediate Support

between the reaction beam flange and floor slab so as to prevent transverse or rotational vibration of the reaction beam flange on its web.

The intermediate supports were designed to hold compression springs against the web of the beam. Each intermediate support consisted of C6x10.5 channel sections welded to a 3/4 in. plate. Each channel had two holes threaded through its web so that bolts could be screwed through to compress springs against the web of the test beam (Fig.(5.4)). The channels were chosen such that the lateral stiffness of the support was governed by the stiffness of the springs alone. The springs were compressed against each side of the web so that the lateral stiffness of the support was equal to twice the stiffness of the individual sides.

The springs used were Century Springs stock #B17-189 compression springs, which have a nominal stiffness of 1.469 kip/in. 2-1/8 in. free length, 1.84 in. solid height, and an outer diameter of 1.00 in.. Load-deflection tests were performed on four springs to determine the spring stiffness. The average stiffness was determined to be approximately 1.35 kip/in.. Tests were performed for two support stiffnesses. The first test used four springs at each intermediate support ($k_s=5.4$ kip/in) and the second used two springs at each intermediate support ($k_s=2.7$ kip/in). During the first test, springs were compressed against the beam web just beneath the top flange and just above the bottom flange on each side of the web. During the second test, a single spring was compressed against each side of the web at the centroid. The springs were compressed between the

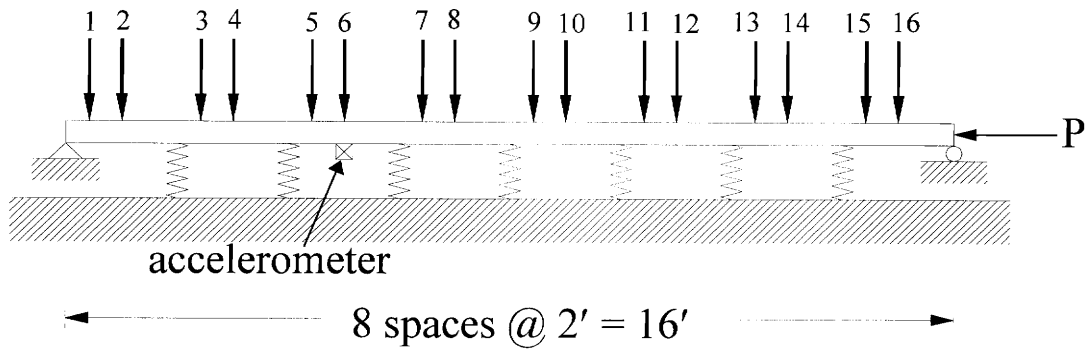


Fig.(5.5) Hammer Impact Locations

beam web and $4 \times 1\frac{1}{2} \times \frac{3}{8}$ in. plates which spanned between the ends of the compressing bolts.

5.3 Data Acquisition

Data were recorded using a Hewlett Packard 35660A Dynamic Signal Analyzer. Channel 1 of the analyzer recorded the hammer impact and channel 2 recorded the accelerometer response. Channel 1 and channel 2 ranges were both set to 1.998 V. The frequency range of the analyzer was set to 400 Hz. The time records were 1 second and the frequency resolution was 1 Hz. The channel 2 window was set to Force Exponential. The frequency responses recorded are averages of three impact responses.

The accelerometer used was a PCB 308b accelerometer which was magnetically attached to the web of the beam at the centroid midway along the third span. The

accelerometer was connected to a PCB Model 480D06 Power Unit which was connected to channel 2 of the analyzer. The gain of the power unit was set to 1.

The beam was excited with a PCB 205M08 impact hammer. The impact hammer had four removable heads of various stiffnesses which could be used. The second to stiffest head (the red one) was chosen for the test because the spectrum response of impacts with this head began to die off around 400 Hz (the highest frequency of interest was about 315 Hz). The hammer was connected to a PCB Model 480D06 Power Unit, set to a gain of 10, which was connected to channel 1 of the analyzer.

For each of the two support stiffnesses tested, frequency responses were recorded for hammer impacts at 16 locations along the length of the beam (Fig.(5.5)). Impacts were made at midspan, between each pair of supports, and 5 in. to the right of each support. Impacts were made at the centroid of the web on the side of the beam opposite the accelerometer.

Before collecting data for either of the support stiffnesses, several cyclic loads between 0 and 26 kips were applied to the beam to seat the supports. It was necessary several times to adjust the positions of some of the springs because of slippage and because of compression of the beam as the load was applied.

5.4 Results

Figures (5.6) through (5.9) show a typical hammer impact, hammer impact spectrum, accelerometer response, and accelerometer frequency response function (FRF),

Hammer Impact Time Signal

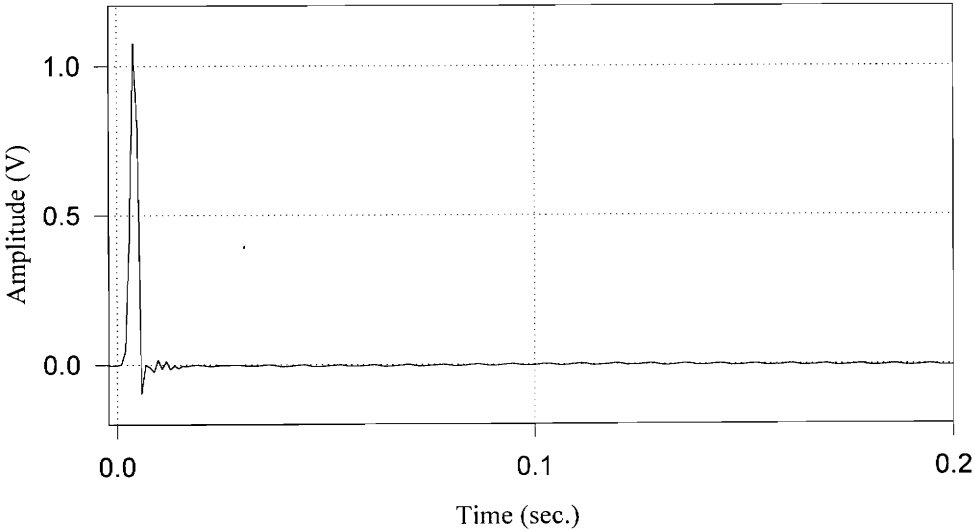


Fig.(5.6) Typical Hammer Impact Excitation

Hammer Impact Spectrum

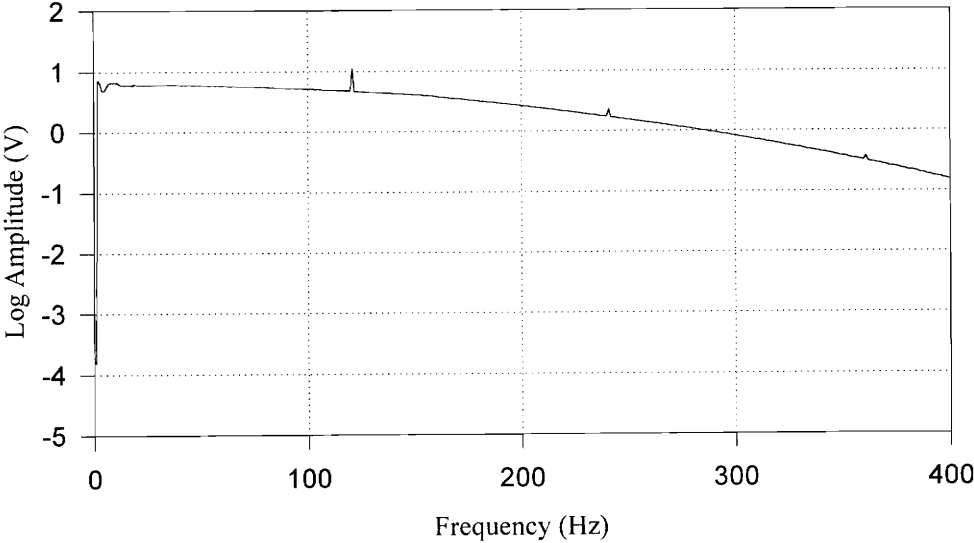


Fig.(5.7) Typical Hammer Impact Spectrum

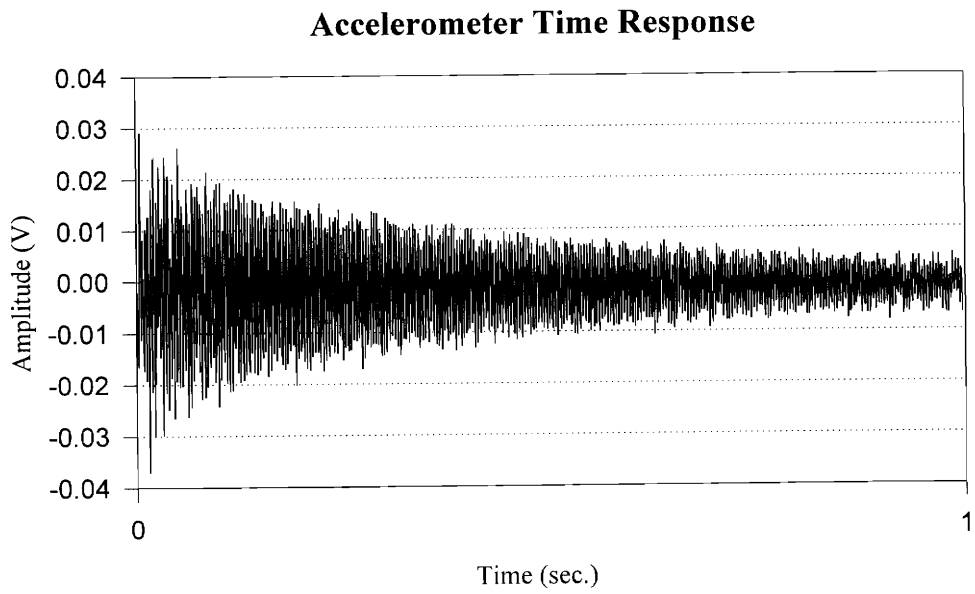


Fig.(5.8) Typical Accelerometer Response

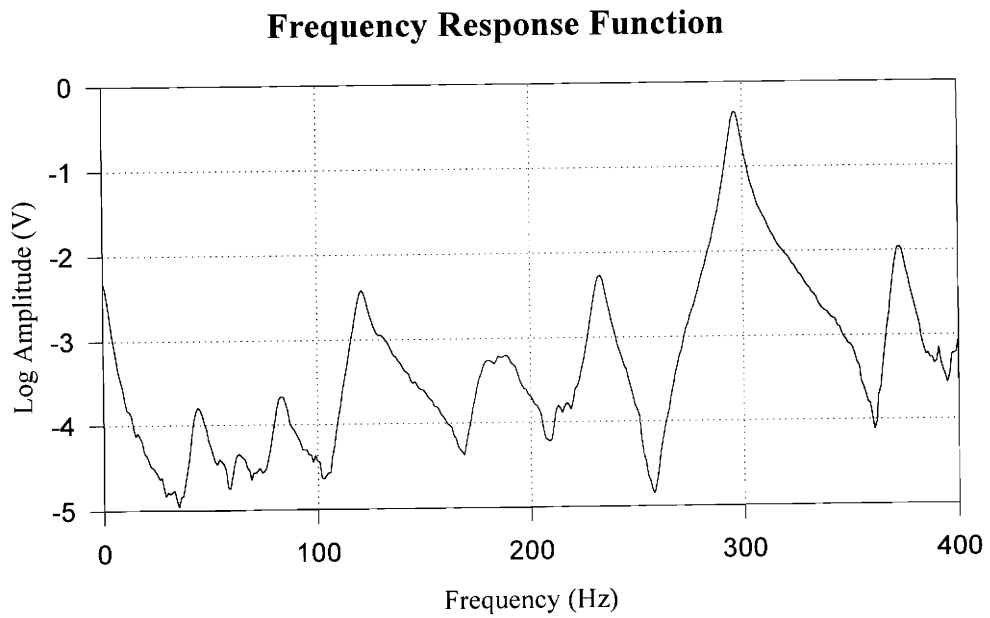


Fig.(5.9) Typical FRF

respectively. Fig.(5.6) represents the acceleration of the hammer over the time of impact. The response spectrum of the accelerometer is an FFT of the accelerometer time response which is then normalized by the hammer impact spectrum.

To determine the mode shape corresponding to each natural frequency of the beam, it is necessary to examine the phase of the frequency responses. Ideally, for a given mode, the phase for an excitation at a given location is equal to, or 180° different than, the phase at any other location. Equal phases imply that deflections at the two locations for the given mode occur in the same transverse direction; a 180° phase difference implies that the two deflections occur in opposite directions. The frequency response and phase define the relative amplitude and relative direction of the mode shape, respectively. By calculating the response amplitude and phase for a series of excitations along the length of the beam, the mode shape of a natural frequency can be determined.

Table (5.1) lists the phase and magnitude of the frequency response for measurements taken with $k_s=2.7$ kip/in. and $P=20$ kips. The data in the table correspond to modes 1, 4, 5, 7, and 8, respectively. The frequencies listed in the table are the frequencies for the driving point FRF (excitation at accelerometer location). The frequencies corresponding to resonant peaks shifted approximately ± 2 Hz depending on the excitation location. This phenomenon generally did not occur for the 8th mode. Mode 2 was not measured because its frequency was so close to the mode 1 frequency

that it was not discernible. Modes 3 and 6 were not used because the accelerometer location was near a node for these modes, which made data for these modes inaccurate.

For the higher modes, phase shifts were near 180° whereas phase shifts for the lower modes tended to vary more. Figures (5.10) through (5.14) show mode shapes plotted from the data in Table (5.1). The mode shape of Fig.(5.10) appears to be a combination of the Mode 1 and Mode 2 eigenvectors. Phase shifts for this lowest resonance generally were not near 180° . This phenomenon is due to the small difference in the Mode 1 and Mode 2 frequencies and is also due to the frequency resolution of the spectrum analyzer (1 Hz). Eigenvectors for modes 4, 5, 7, and 8 are all very similar to

Table (5.1) Magnitude and Phase of Driving Point FRF for $k_s=2.7$ kip/in., $P=20$ kips

	f = 45 Hz		f = 85 Hz		f = 122 Hz		f = 234 Hz		f = 298 Hz	
Loc.	Mag.	Phase	Mag.	Phase	Mag.	Phase	Mag.	Phase	Mag.	Phase
1	4.3	-126	11.8	-144	38.2	171	121	5	532	-11
2	7.9	-90	23.3	-142	65.3	171	218	1	772	-13
3	18.1	-81	30.2	-146	47.0	177	40	140	460	159
4	18.5	-42	26.6	-136	19.6	-137	166	-174	743	167
5	25.7	-53	12.0	-55	72.8	-22	79	-122	419	-22
6	25.1	-32	22.9	-42	75.9	-20	110	-30	700	-11
7	24.5	-54	32.7	-55	21.8	-91	148	-40	478	175
8	19.5	-46	28.9	-54	46.9	-152	31	-143	762	168
9	12.9	-59	12.3	-127	60.1	162	186	148	477	-14
10	11.3	-83	20.8	179	36.5	178	57	133	764	-12
11	12.7	-143	26.2	141	60.6	15	207	-33	483	174
12	16.3	-158	21.3	138	79.2	9	134	-32	774	170
13	17.8	-167	8.3	-8	28.0	-32	199	152	411	-8
14	15.6	-173	21.3	-21	20.6	-141	176	163	743	-9
15	14.1	159	27.1	-42	72.3	180	155	-29	418	170
16	11.5	-161	18.8	-52	58.1	172	202	-28	744	170

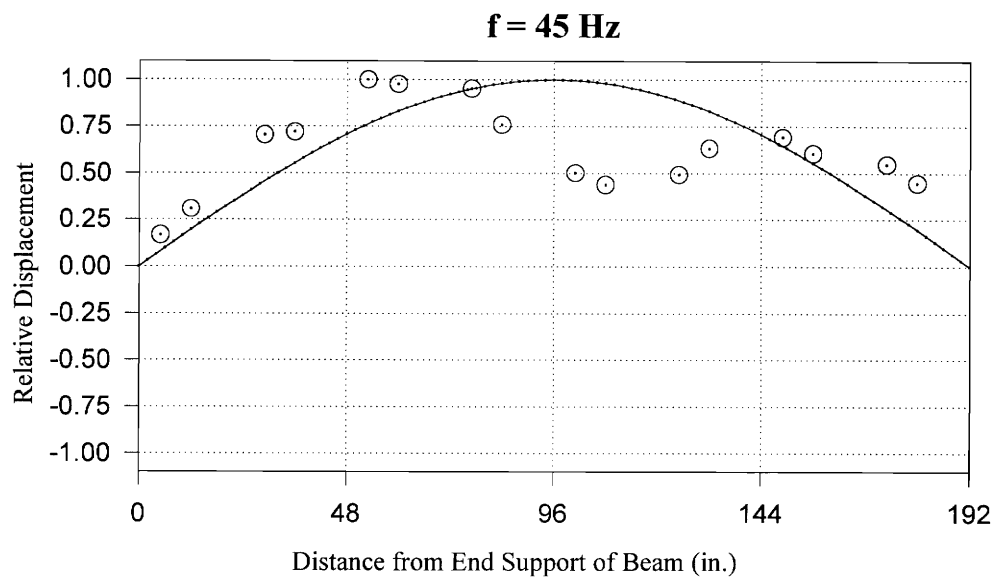


Fig.(5.10) Mode 1 Eigenvector

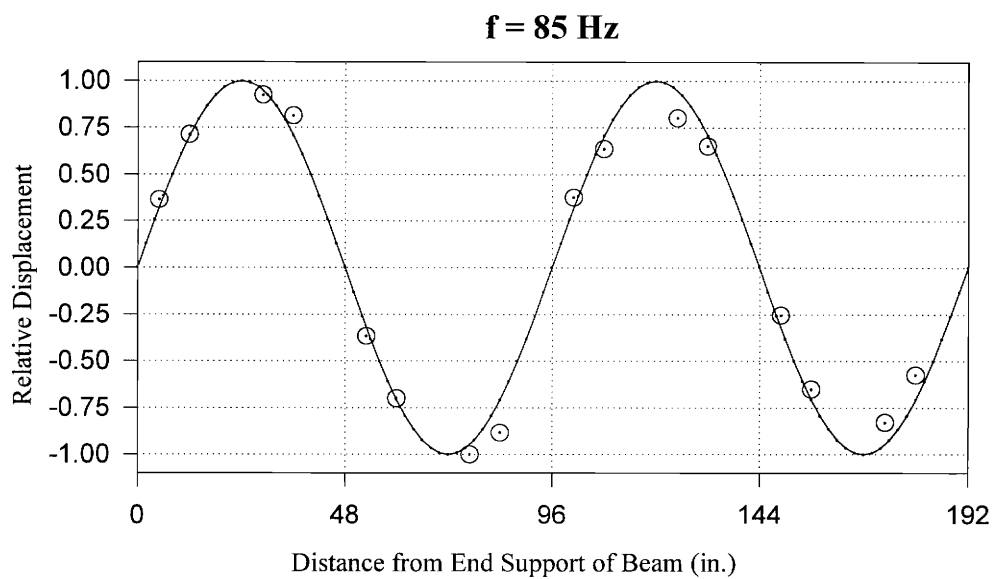


Fig.(5.11) Mode 4 Eigenvector

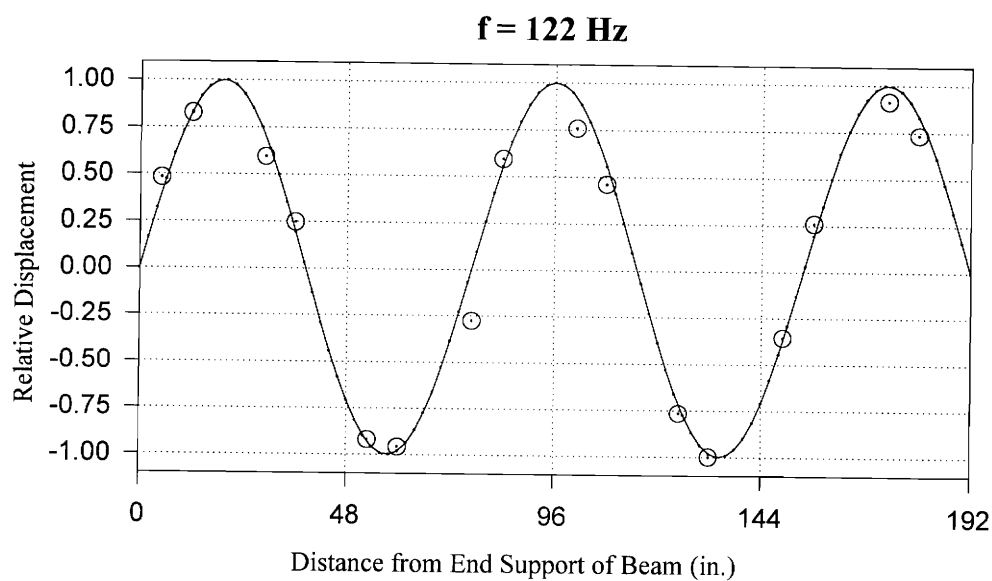


Fig.(5.12) Mode 5 Eigenvector

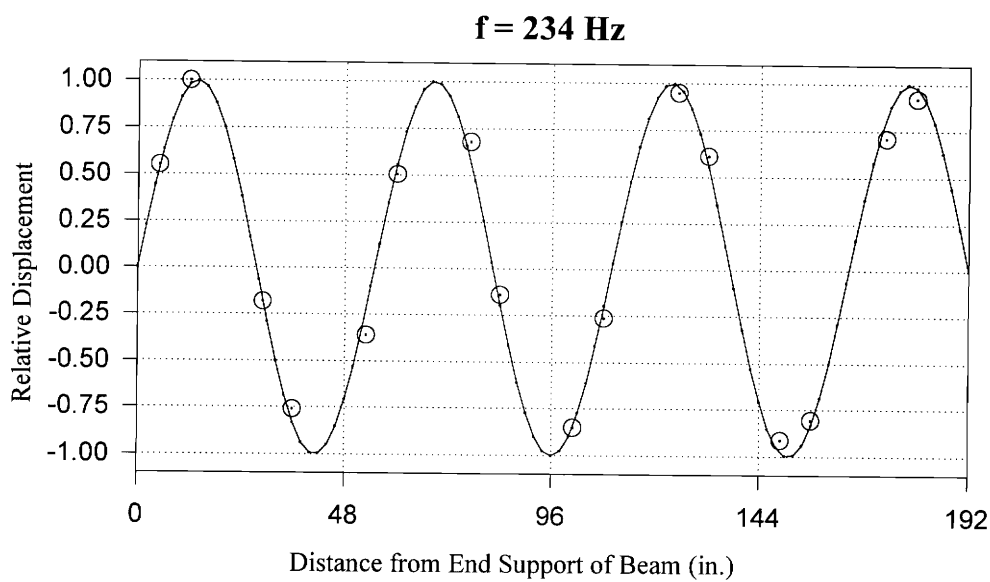


Fig.(5.13) Mode 7 Eigenvector

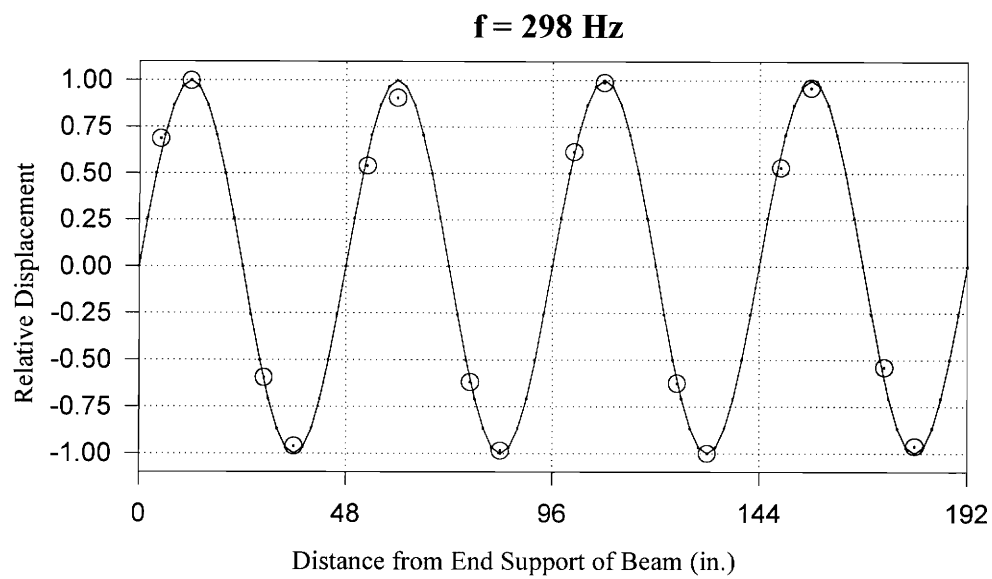


Fig.(5.14) Mode 8 Eigenvector

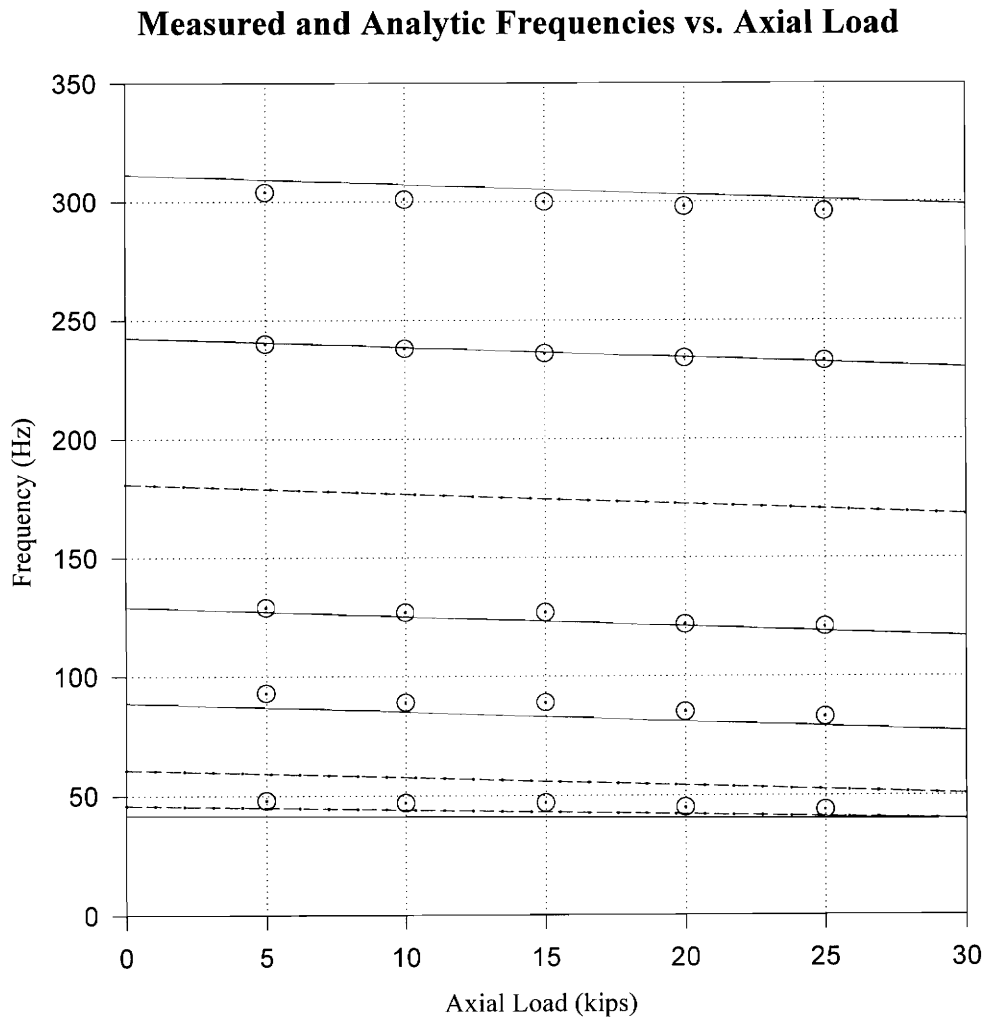


Fig.(5.15) Measured Frequencies vs. Axial Load for $k_s=2.7$ kip/in.

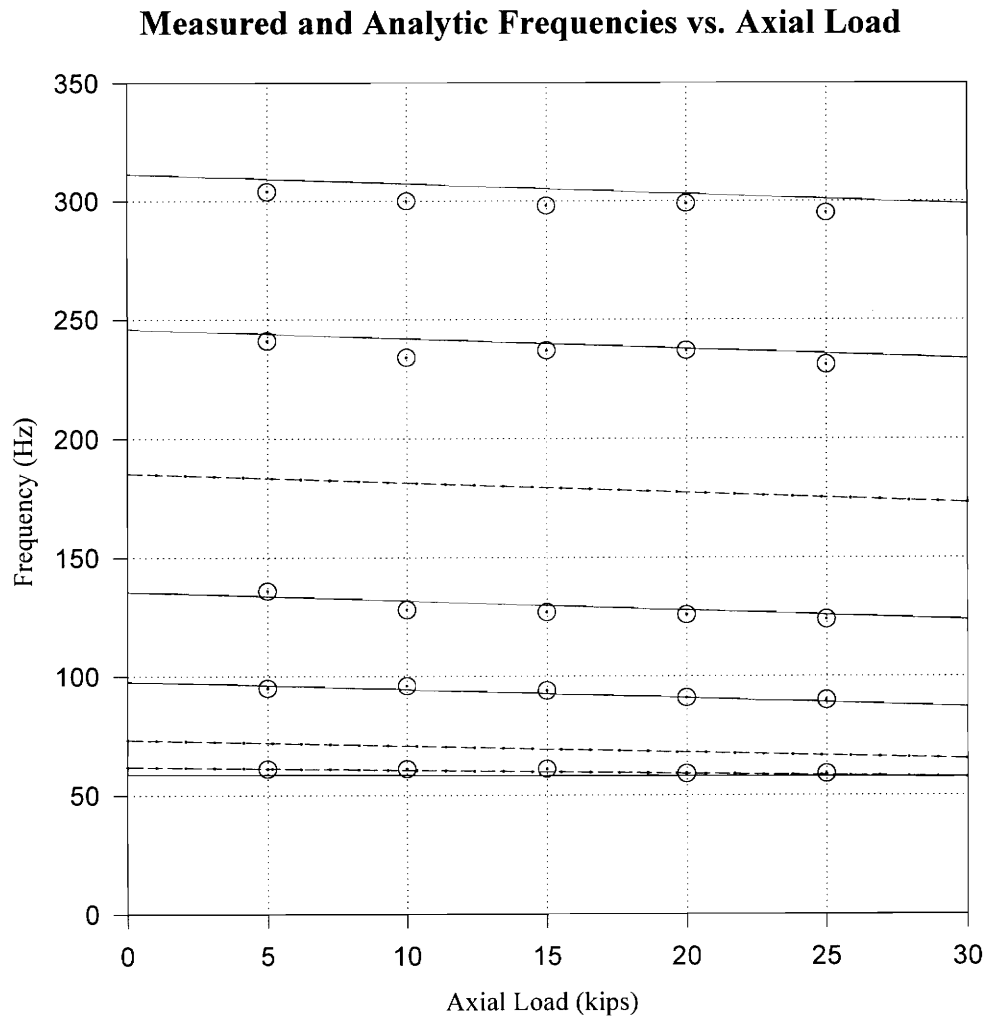


Fig.(5.16) Measured Frequencies vs. Axial Load for $k_s=5.4$ kip/in.

the analytically predicted mode shapes. Fig.(5.15) and Fig.(5.16) show the measured frequencies of the different modes vs. axial load for both spring stiffnesses used. The frequencies are compared to the analytic frequencies of the discrete mass model which include the shear factors in Table (4.1).

Axial loads and support stiffnesses were estimated from contour plots generated using the discrete mass model. Frequencies generated from the discrete model were modified by the shear factors given in Table (3.1). The loads and stiffnesses were estimated based on the intersection of mode 1 and mode 8 contour lines. Figures (5.17) to (5.26) show the contour lines for all five axial loads and for both stiffnesses. Table (5.2) lists the loads and stiffnesses estimated from the contour plots. Estimated loads are plotted vs. applied loads in Figures (5.27) and (5.28).

Table (5.2) Estimated Loads and Stiffnesses

Support Stiffness (kip/in.)	Applied Load (kips)	Estimated Stiffness (kips/in.)	Estimated Load (kips)
2.7	5	3.7	18.0
2.7	10	3.6	25.1
2.7	15	3.6	27.5
2.7	20	3.4	32.1
2.7	25	3.3	36.8
5.4	5	5.9	18.0
5.4	10	6.0	27.5
5.4	15	6.1	32.1
5.4	20	5.7	29.8
5.4	25	5.7	39.1

Contour Lines for Modes 1-8

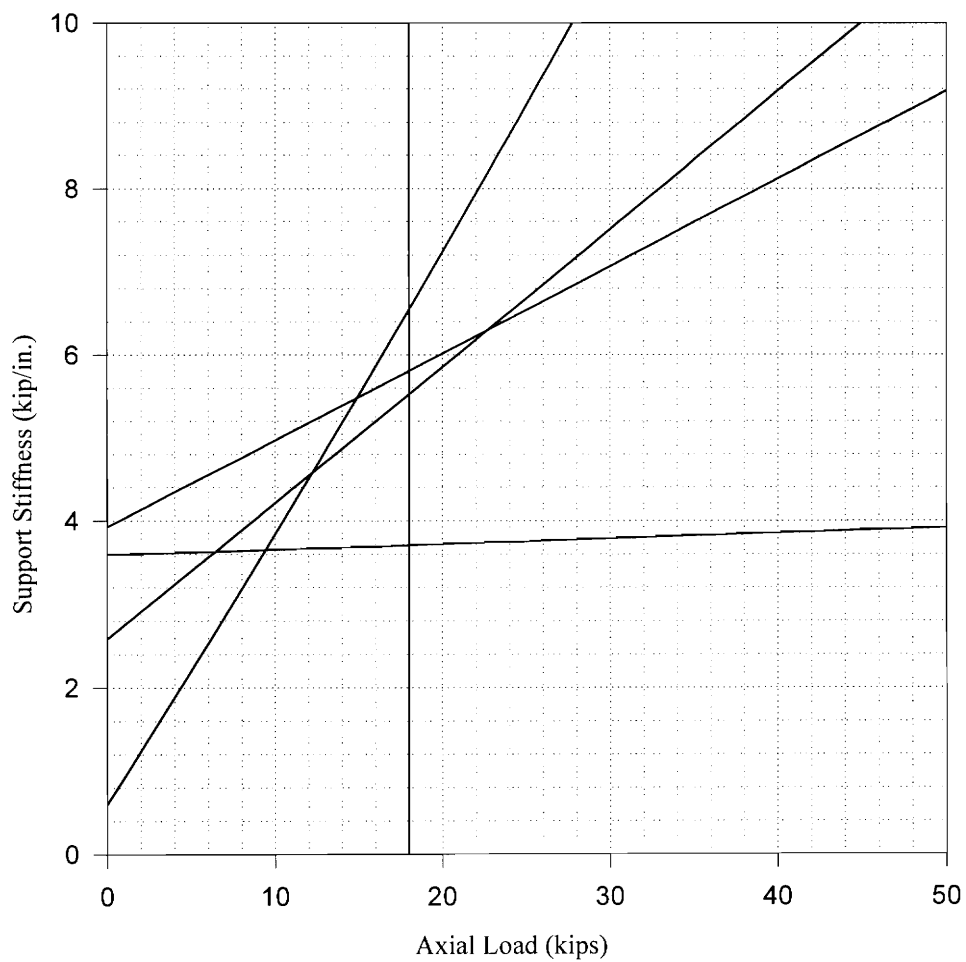


Fig.(5.17) Contour Plot for $k_s=2.7$ kips/in. , $P=5$ kips

Contour Lines for Modes 1-8

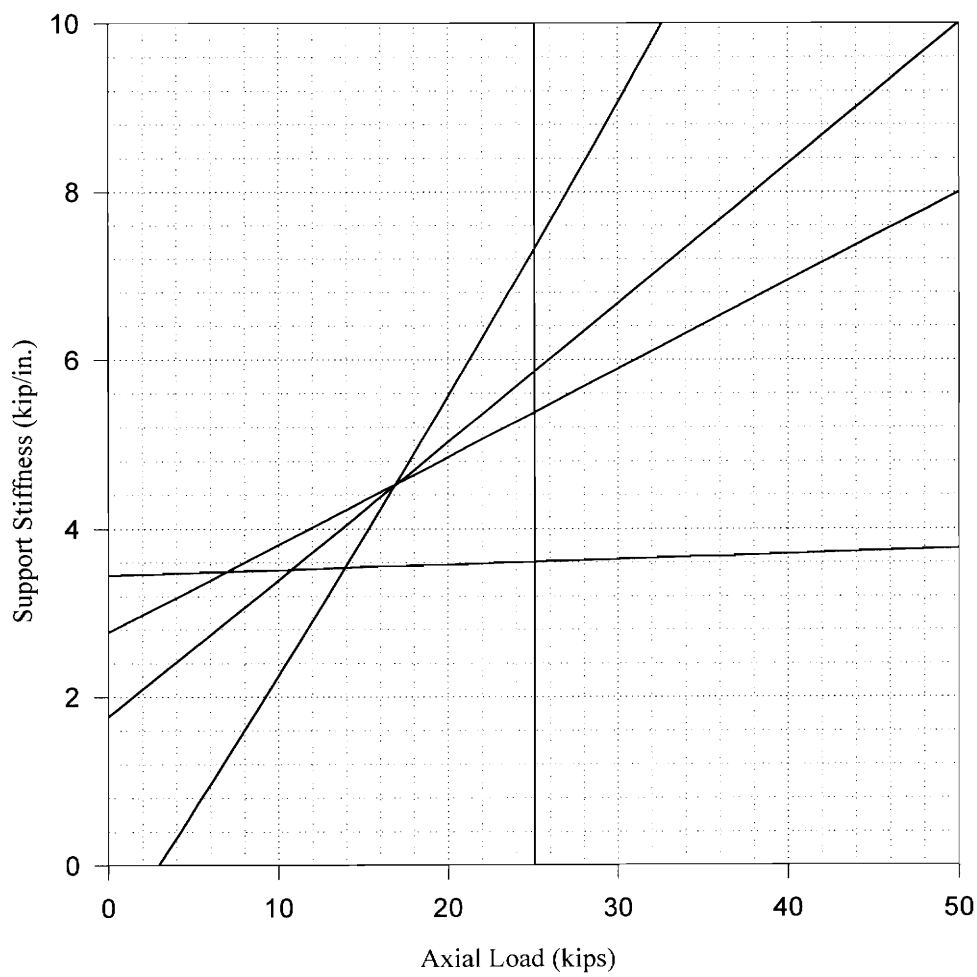


Fig.(5.18) Contour Plot for $k_s=2.7$ kip/in. , $P=10$ kips

Contour Lines for Modes 1-8

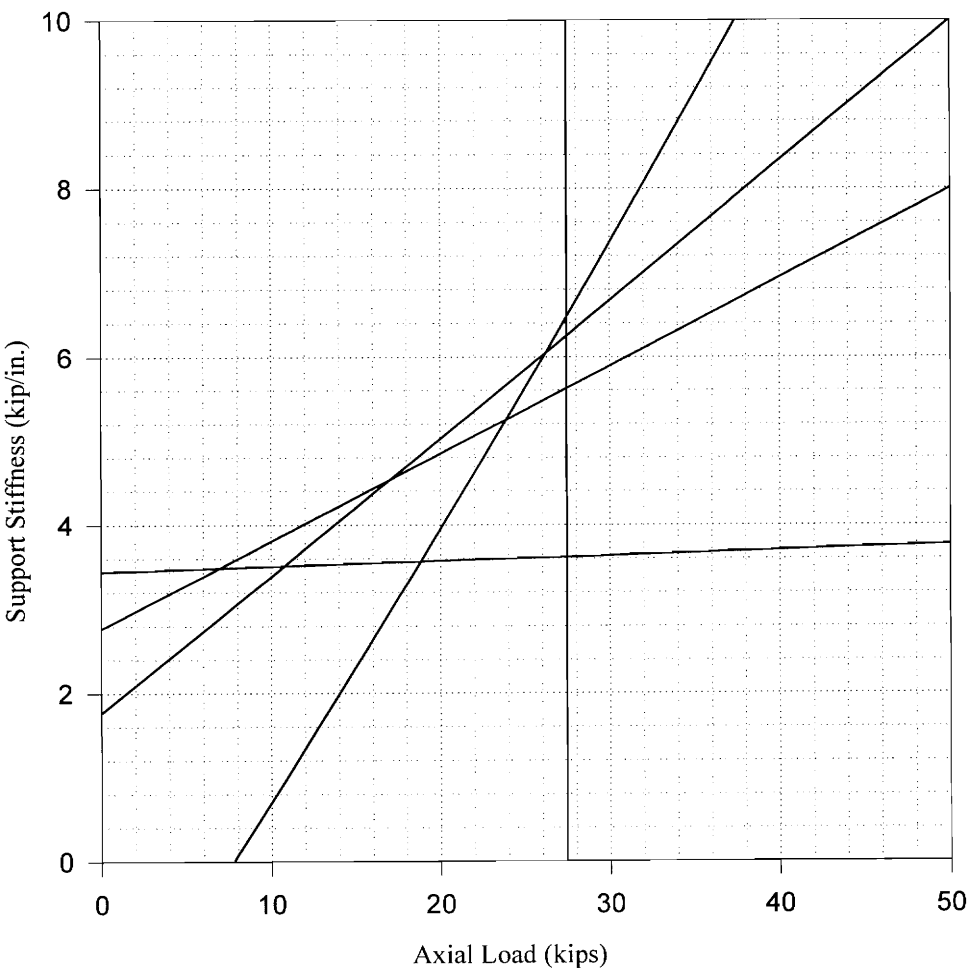


Fig.(5.19) Contour Plot for $k_s=2.7$ kip/in. , $P=15$ kips

Contour Lines for Modes 1-8

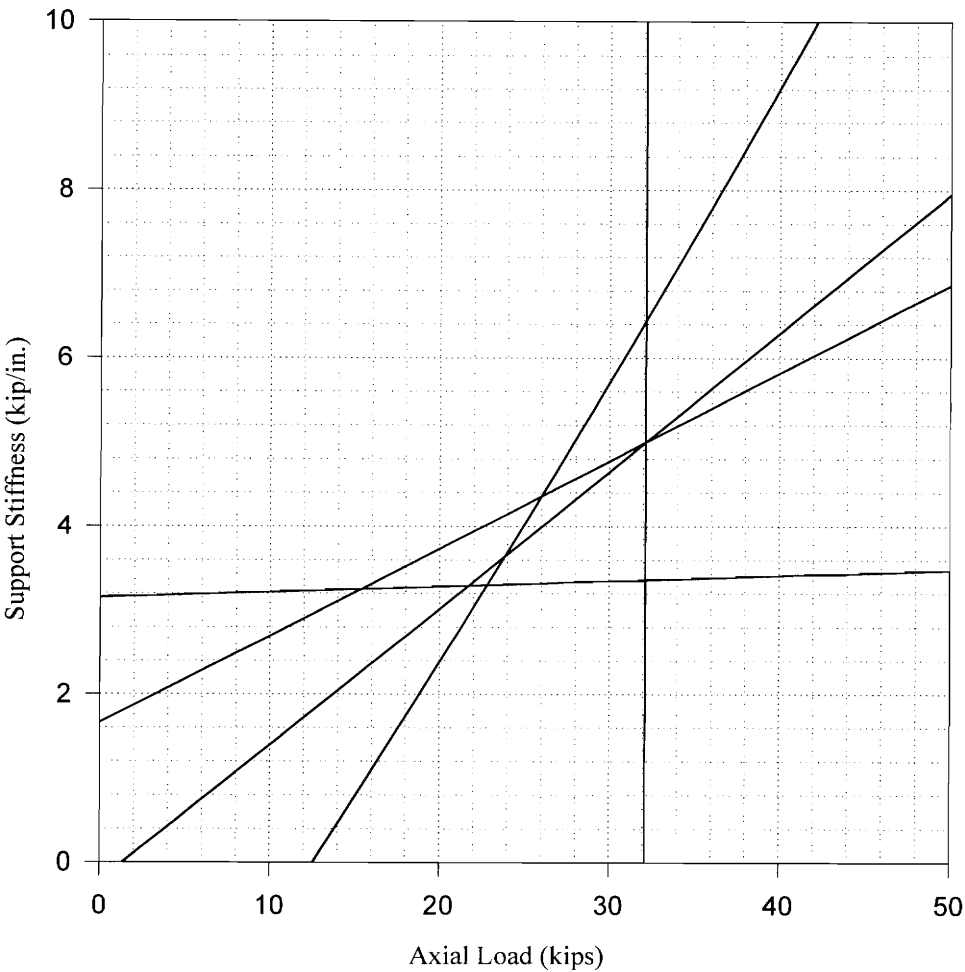


Fig.(5.20) Contour Plot for $k_s=2.7$ kip/in. , $P=20$ kips

Contour Lines for Modes 1-8

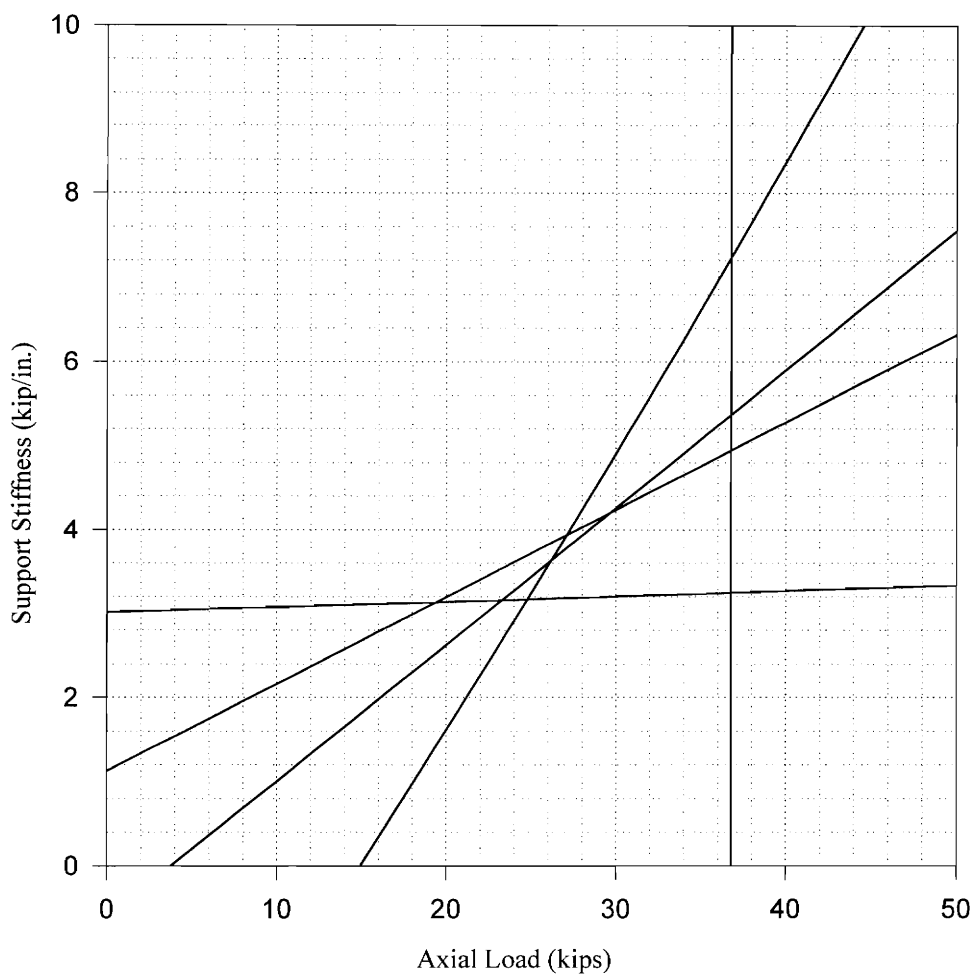


Fig.(5.21) Contour Plot for $k_s=2.7$ kip/in. , $P=25$ kips

Contour Lines for Modes 1-8

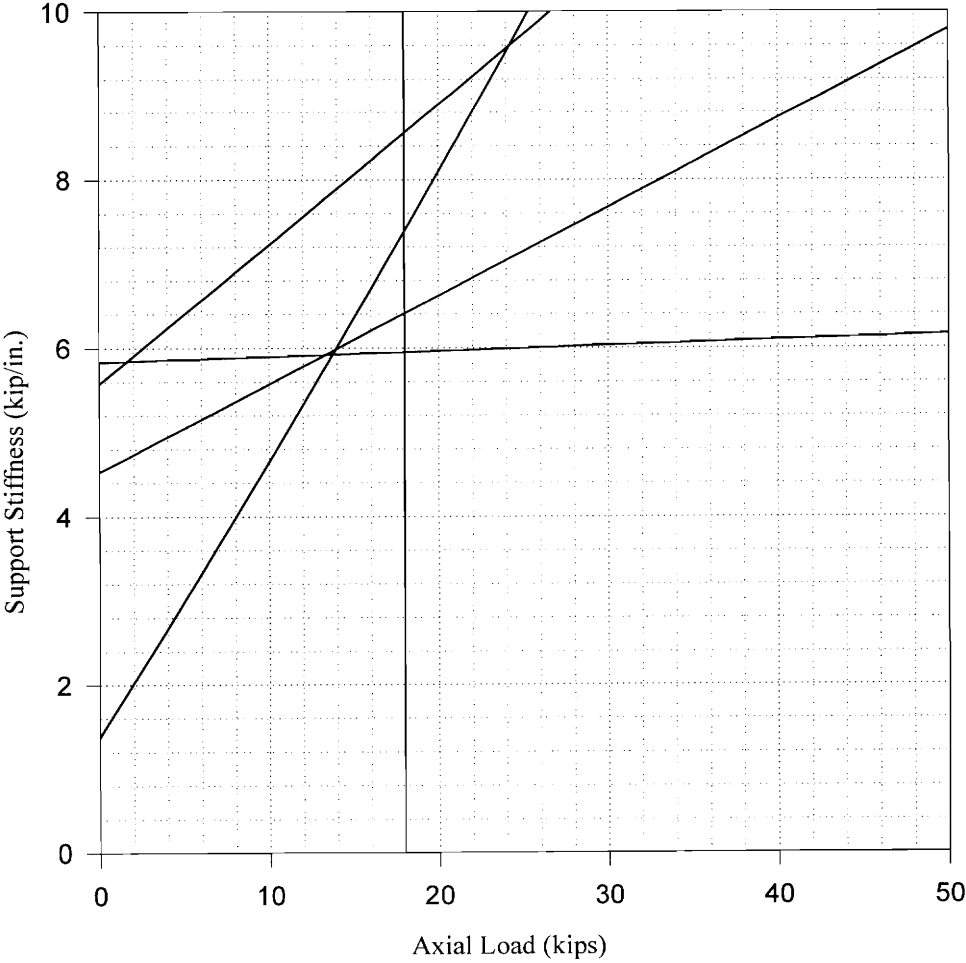


Fig.(5.22) Contour Plot for $k_s=5.4$ kip/in. , $P=5$ kips

Contour Lines for Modes 1-8

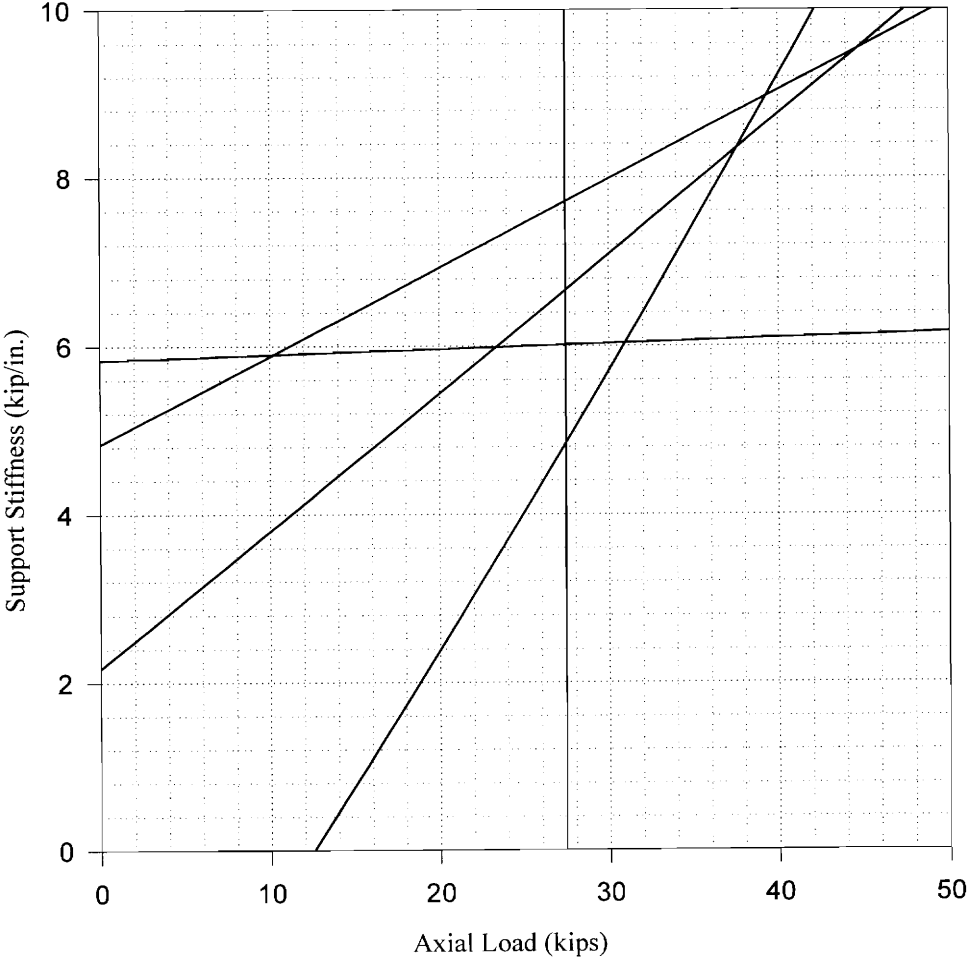


Fig.(5.23) Contour Plot for $k_s=5.4$ kip/in. , $P=10$ kips

Contour Lines for Modes 1-8

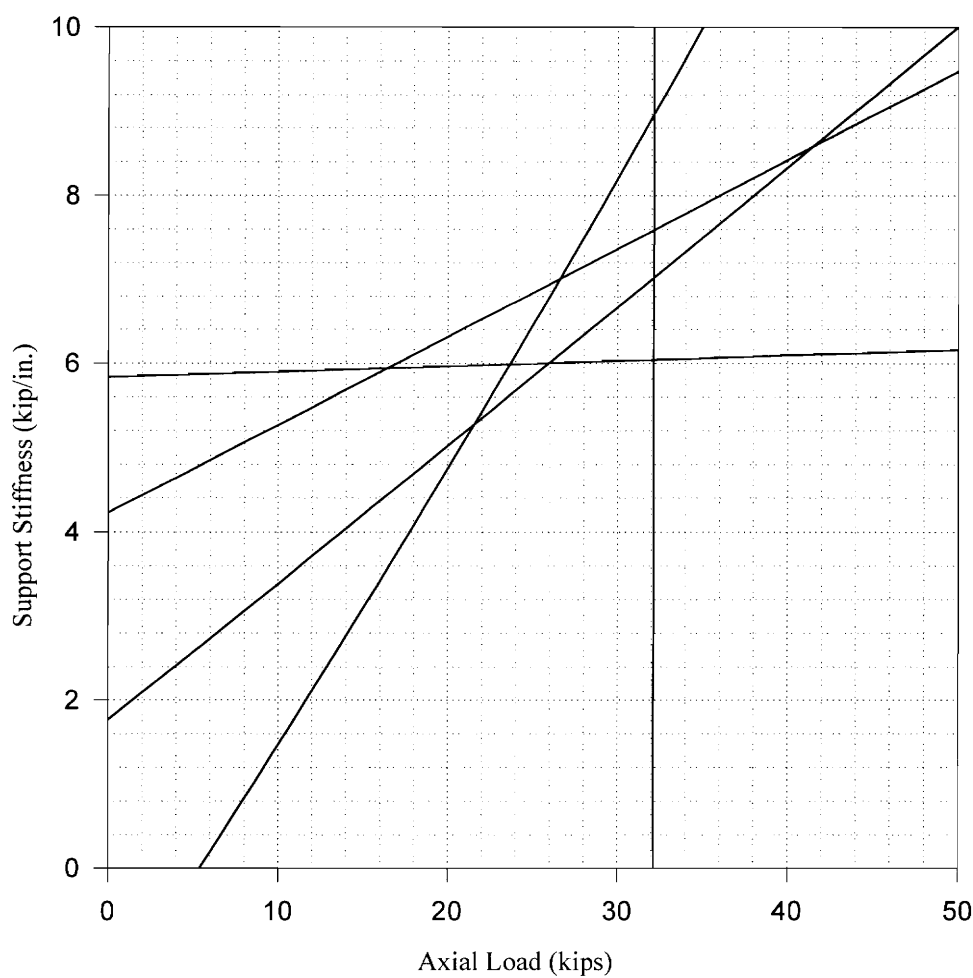


Fig.(5.24) Contour Plot for $k_s=5.4$ kip/in. , $P=15$ kips

Contour Lines for Modes 1-8

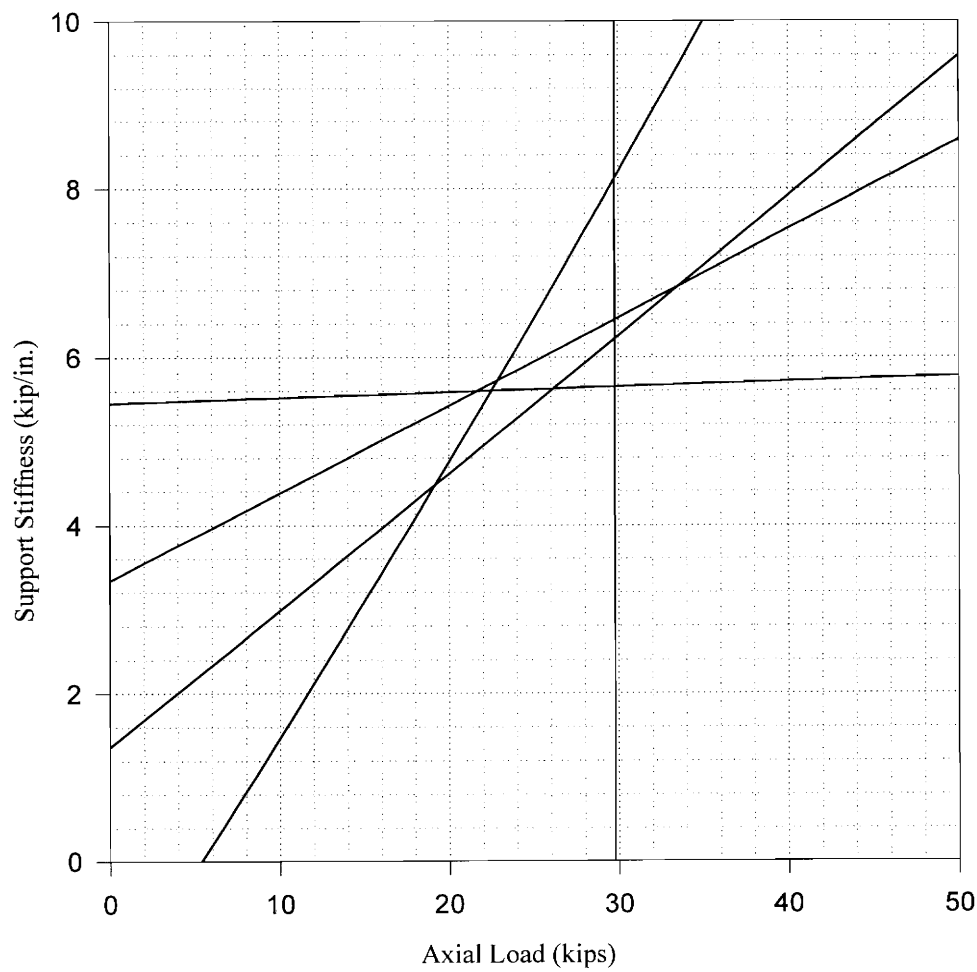


Fig.(5.25) Contour Plot for $k_s=5.4$ kip/in. , $P=20$ kips

Contour Lines for Modes 1-8

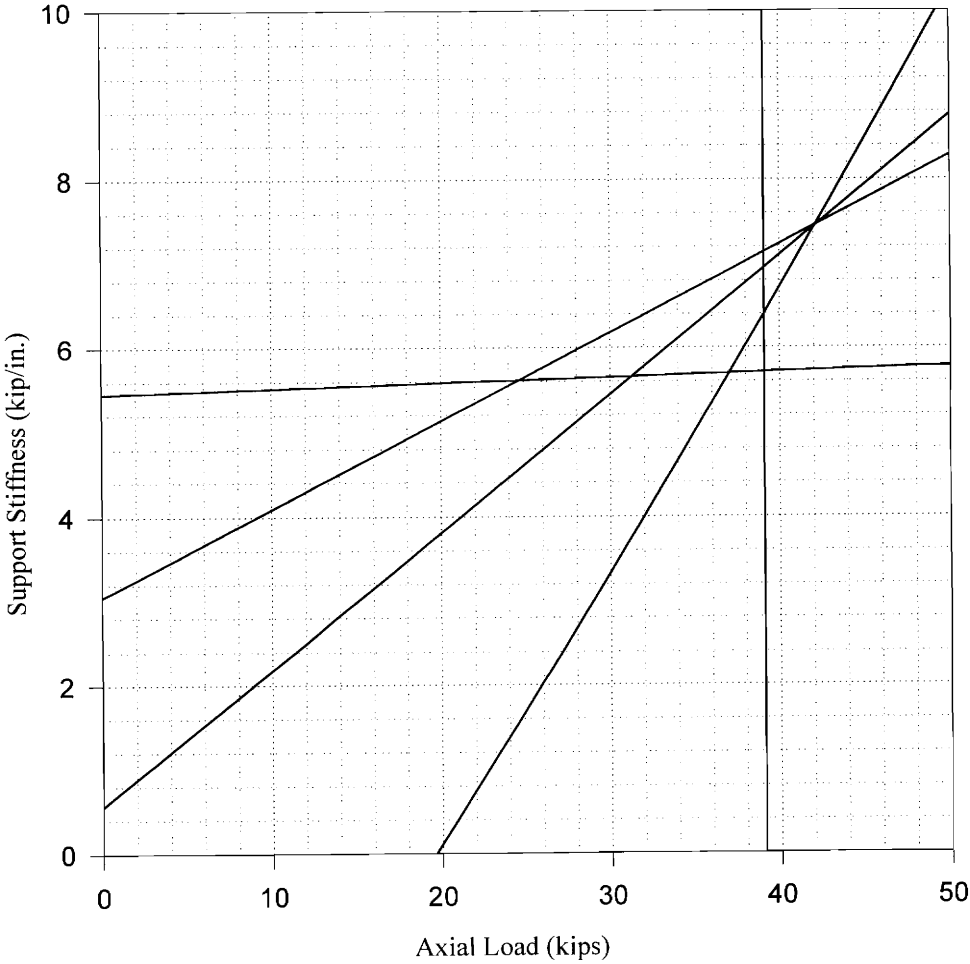


Fig.(5.26) Contour Plot for $k_s=5.4$ kip/in. , $P=25$ kips

Estimated Loads vs. Applied Loads

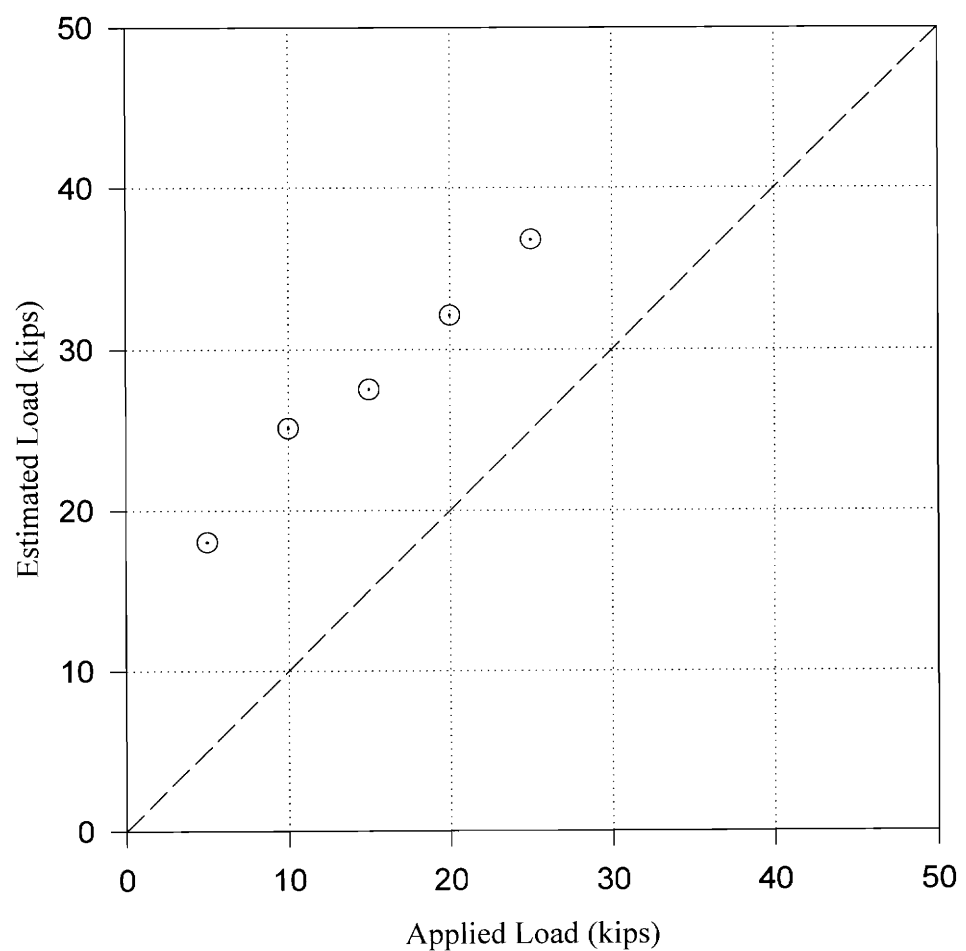


Fig.(5.27) Estimated vs. Applied Axial Load for $k_s=2.7$ kips/in.

Estimated Loads vs. Applied Loads

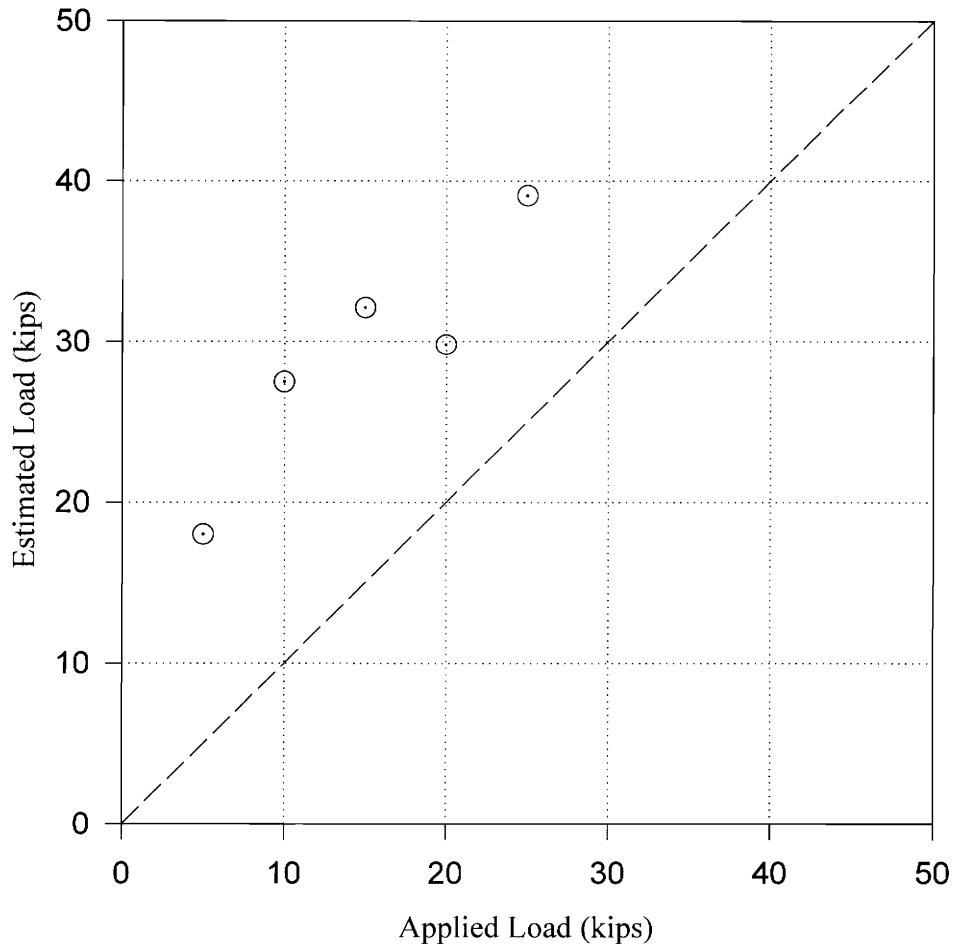


Fig.(5.28) Estimated vs. Applied Axial Load for $k_s=5.4$ kips/in.

5.5 Possible Effect of End Support Stiffness

The deviations between the estimated and applied axial loads are all around 12-15 kips. The estimated loads plotted in Figures (5.27) and (5.28) lie along lines having nearly the same slope as the ideal curves with a 12-15 kip offset. Referring to Figures (5.15) and (5.16), the errors in the estimated loads are equal to the horizontal distances between the measured 8th mode frequencies and the theoretical 8th mode curves.

A possible source of error could be that the lateral stiffness of the end support at the hydraulic ram may have been significantly lower than expected. A low end support stiffness would have little effect on lower modes of vibration, but would have an increasing effect for higher modes. Fig.(5.29) shows the effect that the stiffness of one end support has on the frequency of the 8th mode for an axial load of 21 kips. The figure assumes that the other end support has an infinite stiffness and that the intermediate supports have 2.7 kip/in. stiffness. For stiffnesses above 300 kip/in., the support acts similarly to a pinned support; however, for stiffnesses less than 300 kip/in., the Mode 8 frequency is greatly affected by the end support.

If it were assumed that a low end support stiffness was the cause of the error in estimated axial loads, the stiffness of the support could be estimated using the known values of axial load and intermediate support stiffness. If a plot as in Fig.(5.29) were created for an applied axial load, the estimated end support stiffness would be the stiffness corresponding to the measured mode 8 frequency. The average end support

Mode 8 Frequency vs. Ram End Support Stiffness

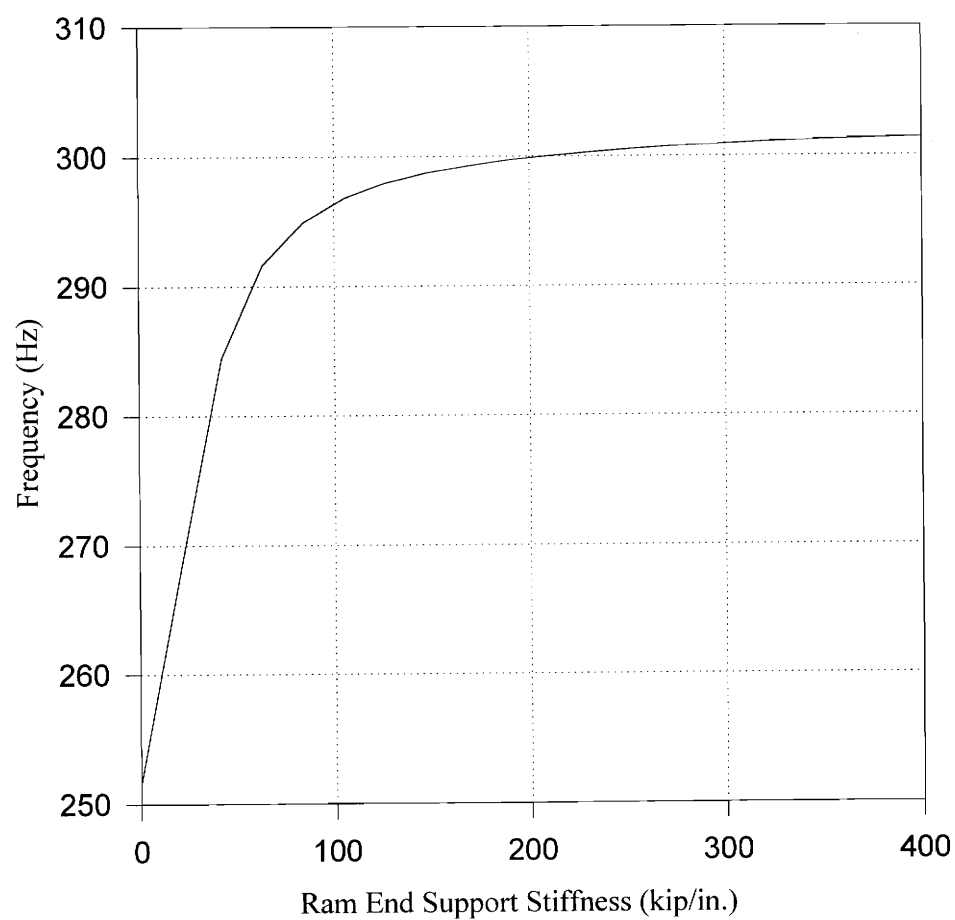


Fig.(5.29) Effect of Ram End Support Stiffness on Mode 8 Frequency

stiffness which would result in the measured mode 7 and mode 8 frequencies for all ten tests performed is 110 kip/in. Supposing that 110 kip/in. is the stiffness of the support, the stiffness can be included in the discrete model to see its effect on the estimated loads. Figures (5.30) to (5.39) show contour plots for the measured data using an end support stiffness of 110 kip/in.. Table (5.3) shows the loads and intermediate support stiffnesses estimated based on these contour plots.

Table (5.3) Estimated Loads and Stiffnesses for Assumed End Support Stiffness

Support Stiffness (kip/in.)	Applied Load (kips)	Estimated Stiffness (kips/in.)	Estimated Load (kips)
2.7	5	3.6	3.4
2.7	10	3.5	11.1
2.7	15	3.5	13.6
2.7	20	3.3	18.6
2.7	25	3.2	23.7
5.4	5	5.9	3.6
5.4	10	5.9	13.8
5.4	15	6.0	18.8
5.4	20	5.6	16.3
5.4	25	5.6	26.3

Modified Model Contour Lines for Modes 1-8

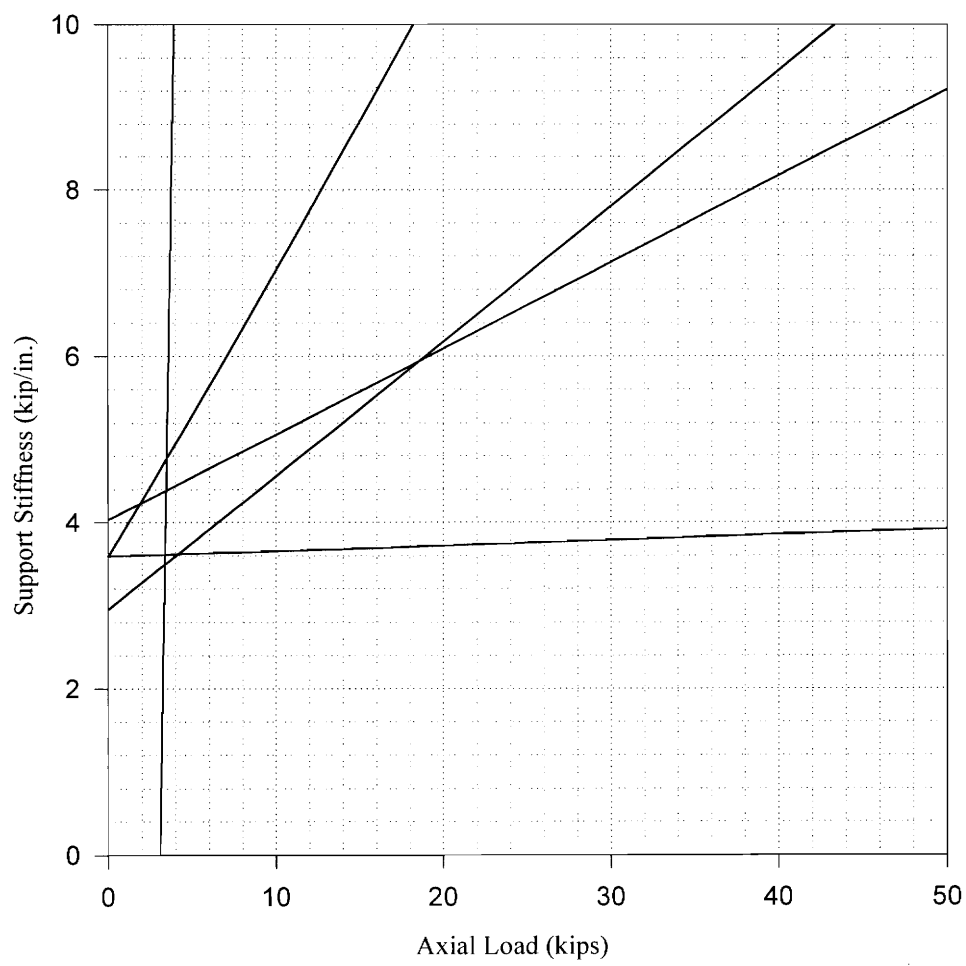


Fig.(5.30) Modified Model Contour Plot for $k_s=2.7$ kip/in. , $P=5$ kips

Modified Model Contour Lines for Modes 1-8

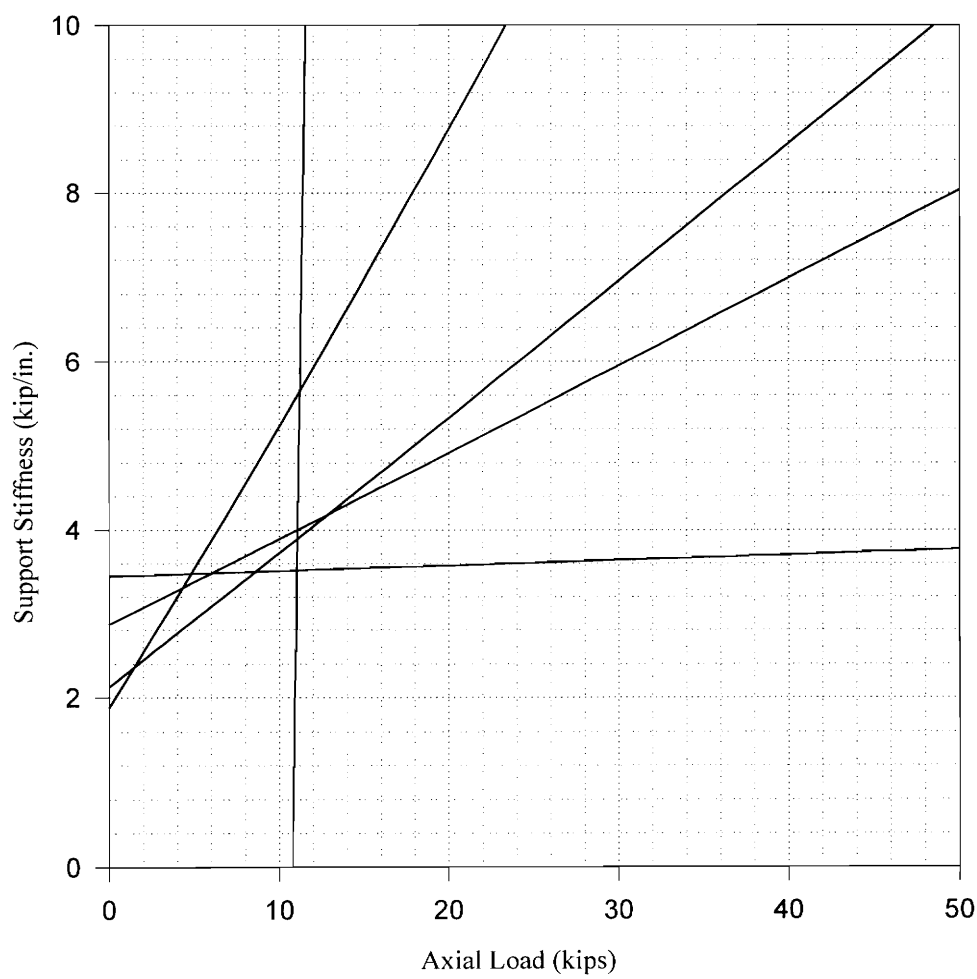


Fig.(5.31) Modified Model Contour Plot for $k_s=2.7$ kip/in. , $P=10$ kips

Modified Model Contour Lines for Modes 1-8

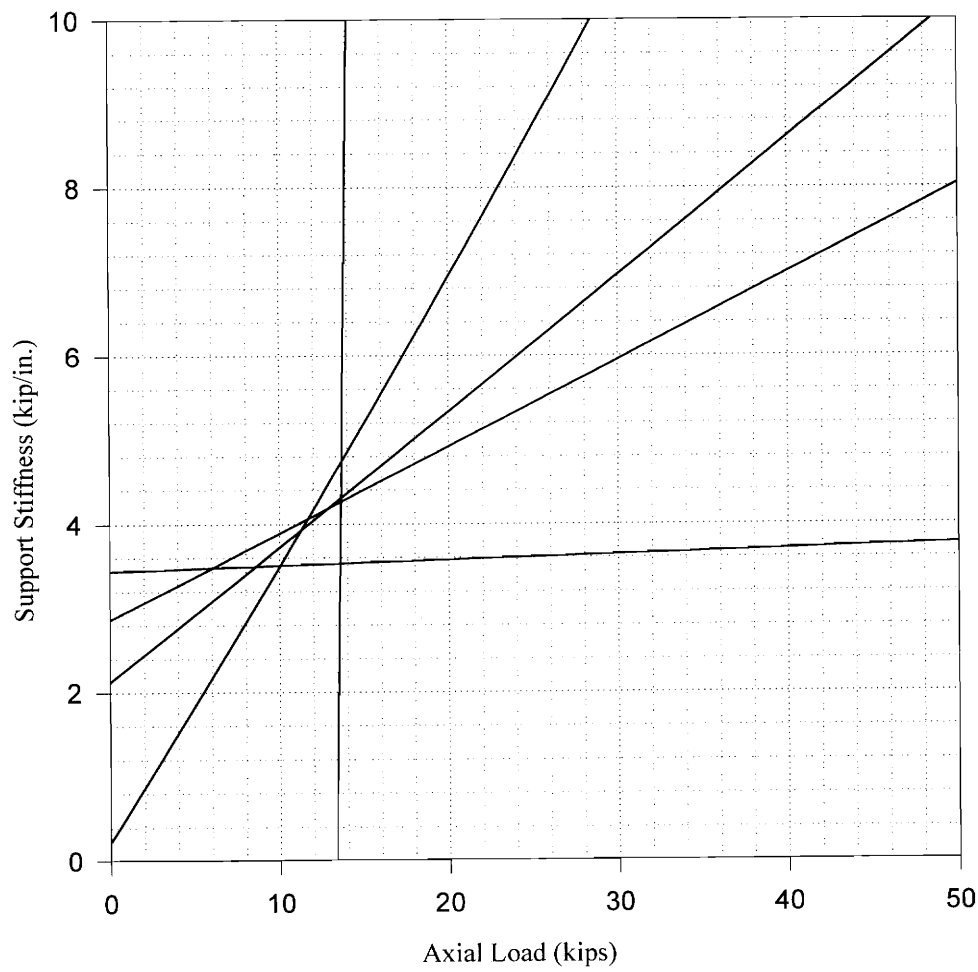


Fig.(5.32) Modified Model Contour Plot for $k_s=2.7$ kip/in. , $P=15$ kips

Modified Model Contour Lines for Modes 1-8

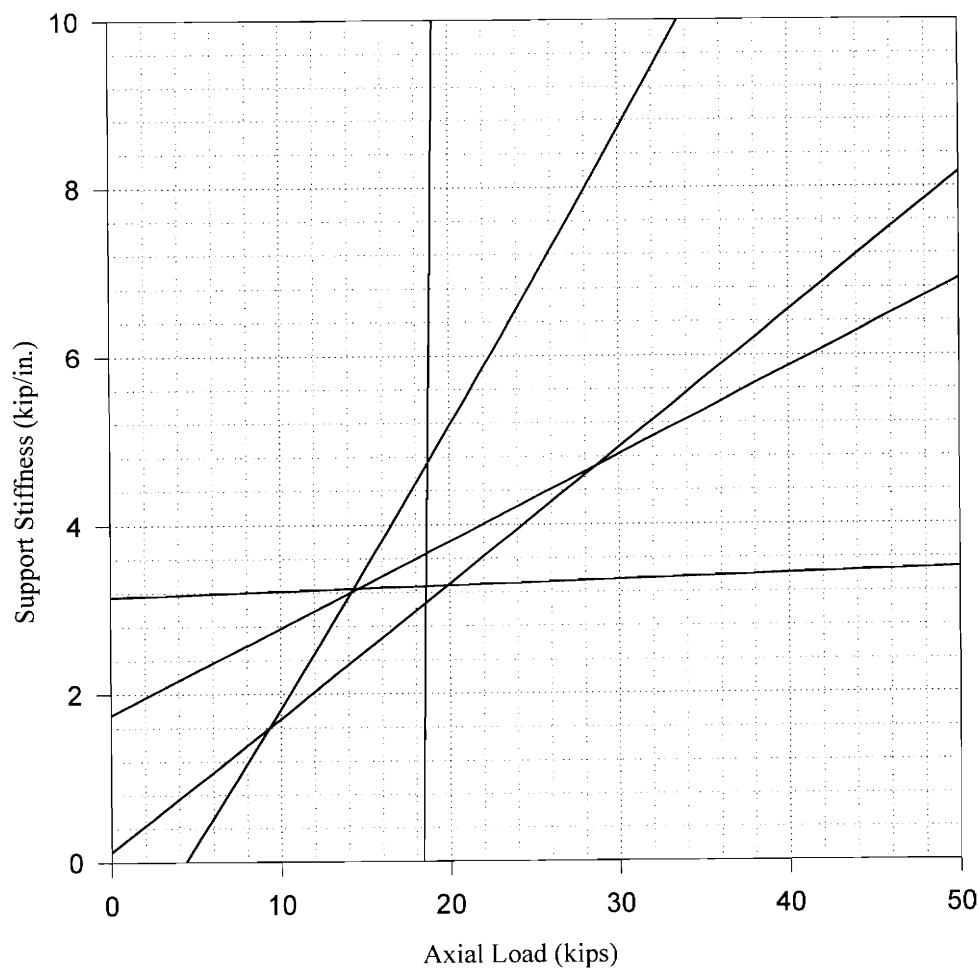


Fig.(5.33) Modified Model Contour Plot for $k_s=2.7$ kip/in. , $P=20$ kips

Modified Model Contour Lines for Modes 1-8

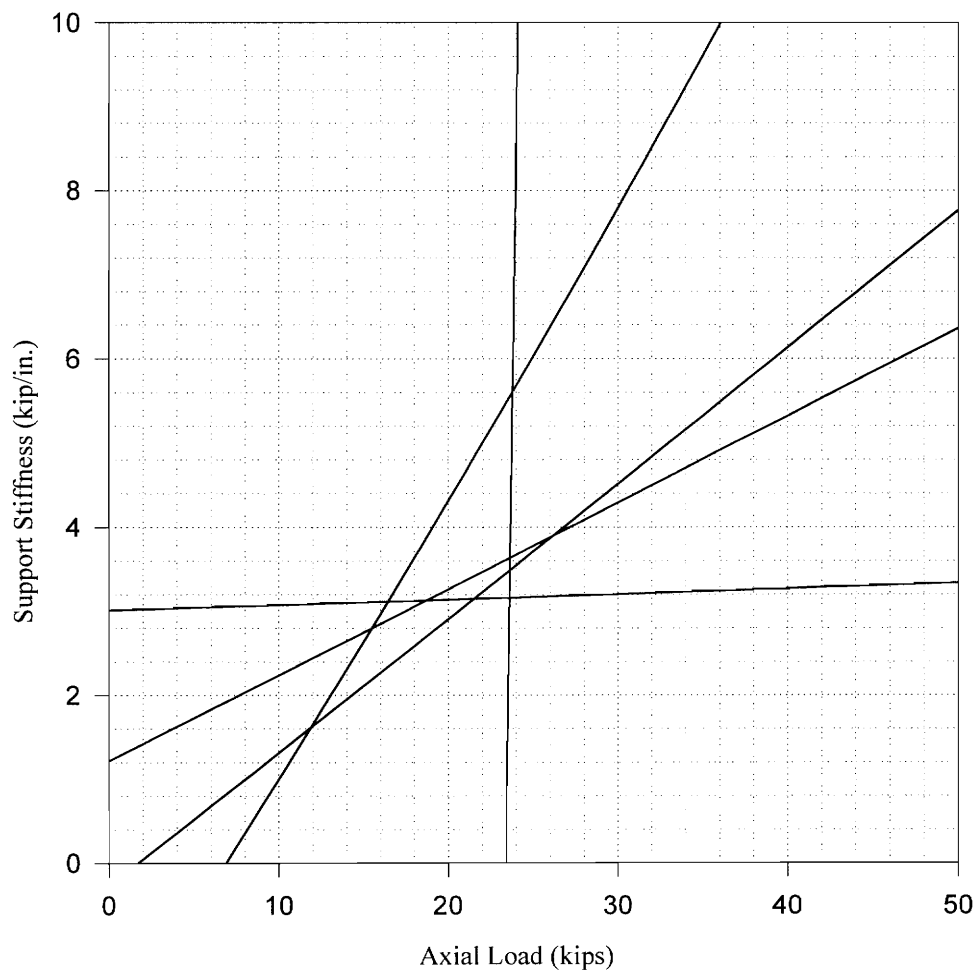


Fig.(5.34) Modified Model Contour Plot for $k_s=2.7$ kip/in. , $P=25$ kips

Modified Model Contour Lines for Modes 1-8

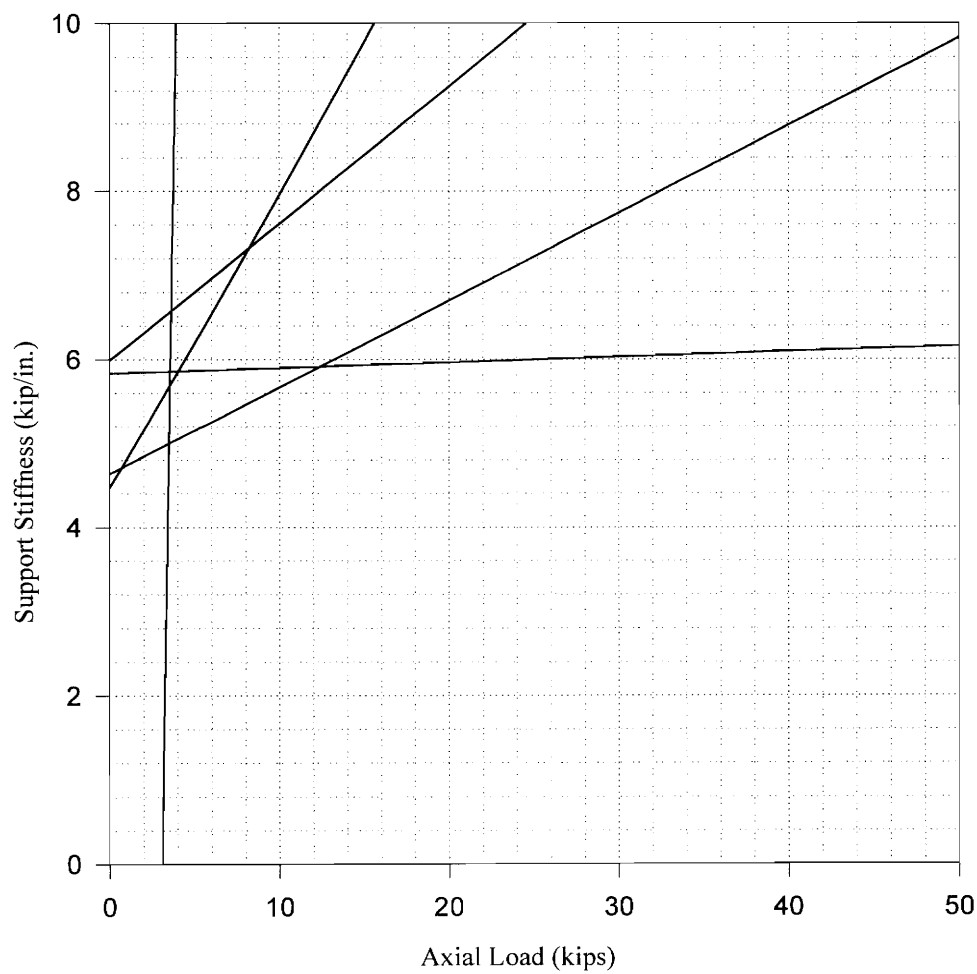


Fig.(5.35) Modified Model Contour Plot for $k_s=5.4$ kip/in. , $P=5$ kips

Modified Model Contour Lines for Modes 1-8

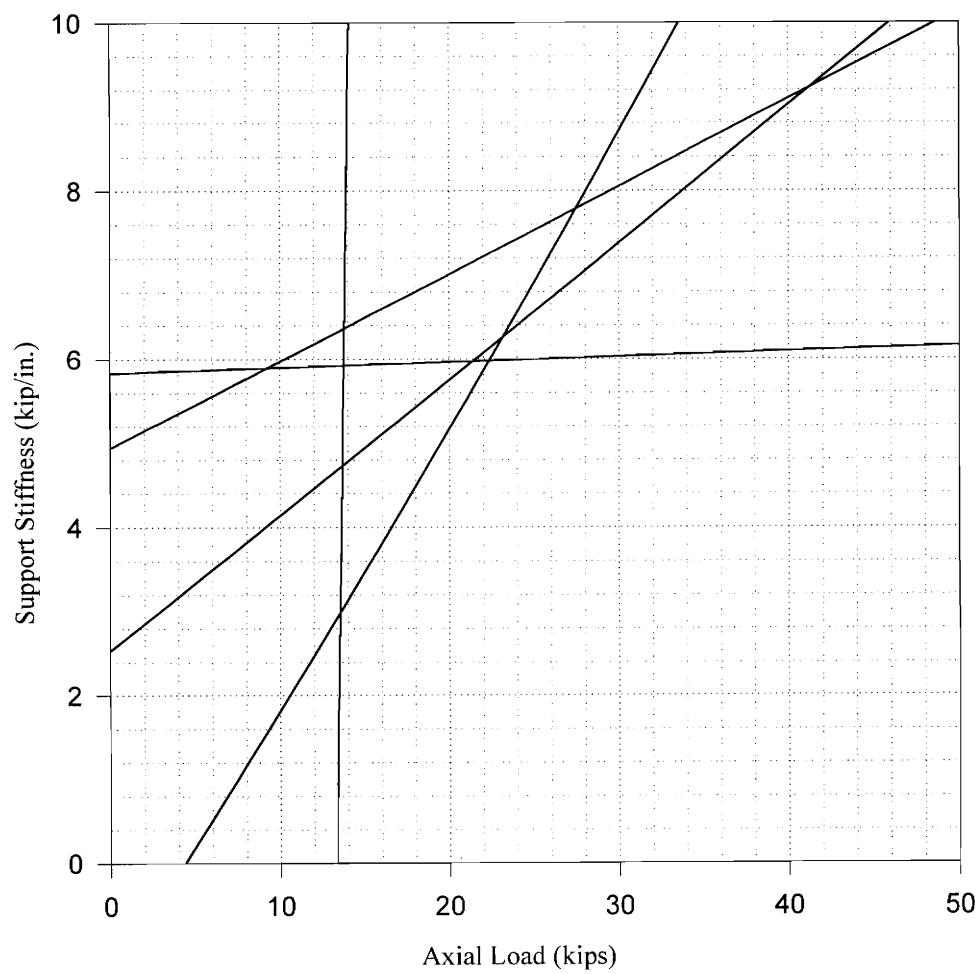


Fig.(5.36) Modified Model Contour Plot for $k_s=5.4$ kip/in. , $P=10$ kips

Modified Model Contour Lines for Modes 1-8

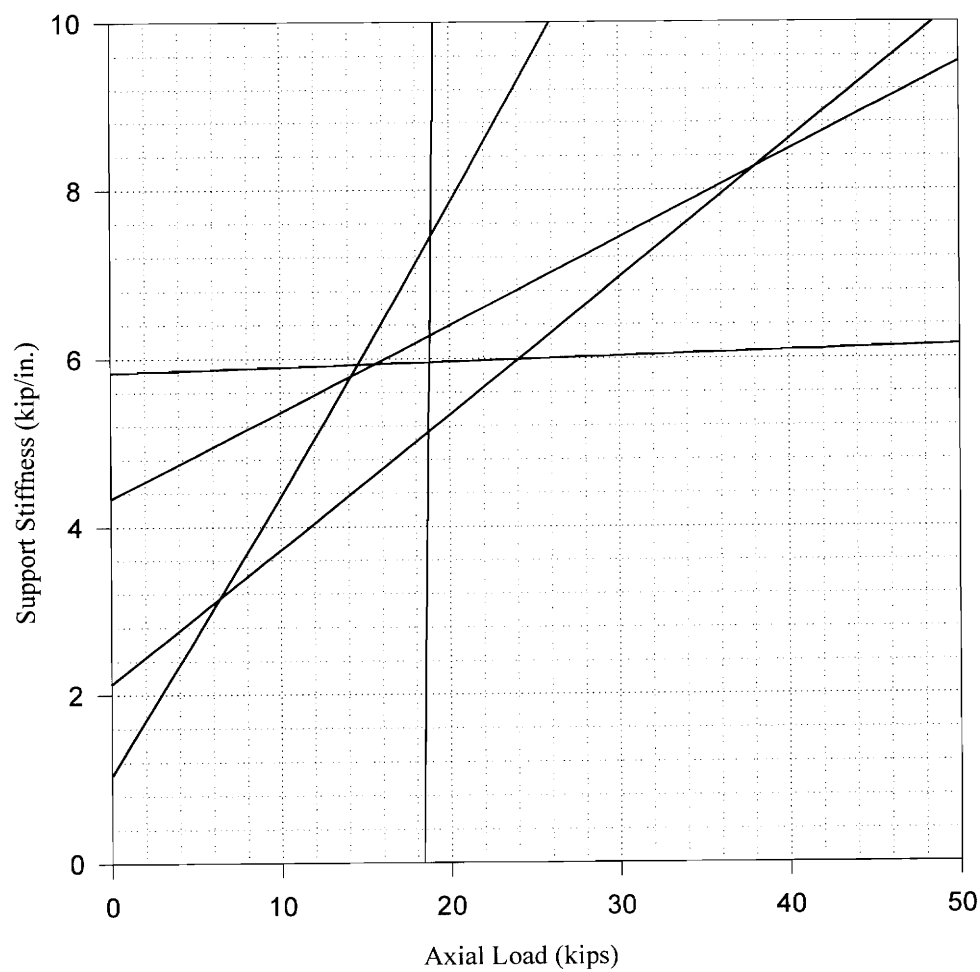


Fig.(5.37) Modified Model Contour Plot for $k_s=5.4$ kip/in. , $P=15$ kips

Modified Model Contour Lines for Modes 1-8

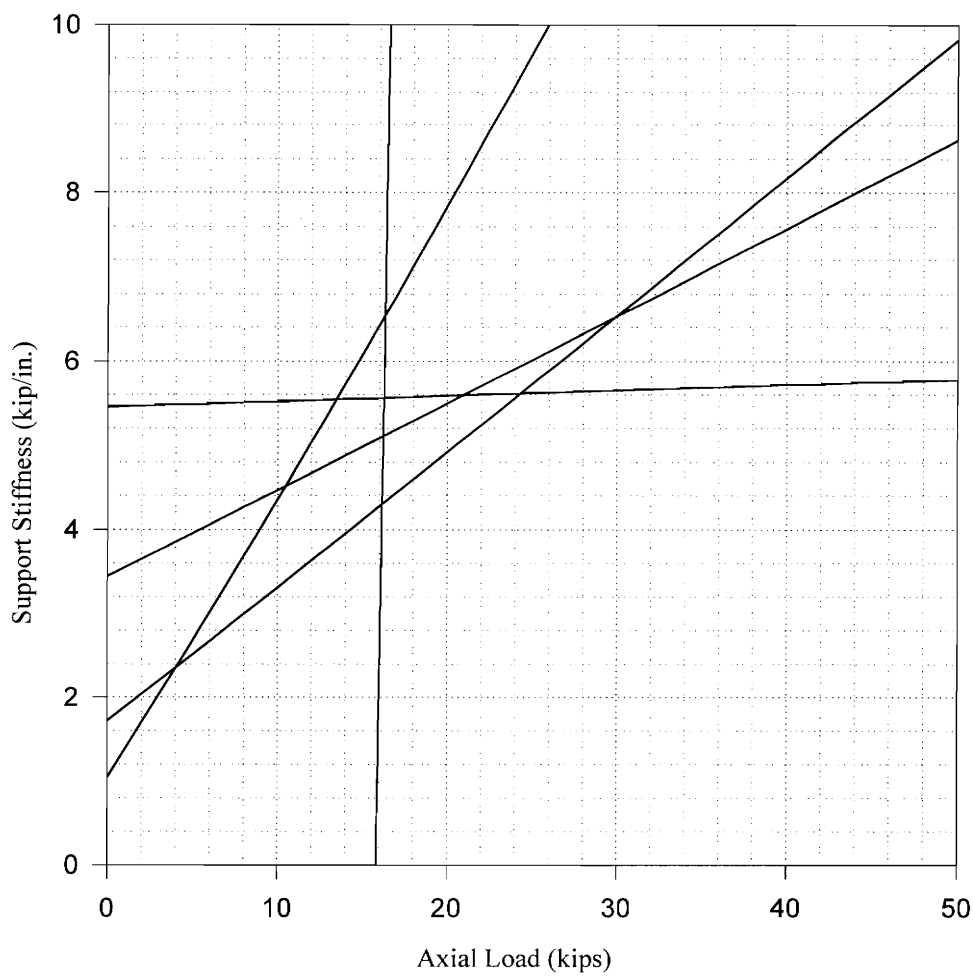


Fig.(5.38) Modified Model Contour Plot for $k_s=5.4$ kip/in. , $P=20$ kips

Modified Model Contour Lines for Modes 1-8

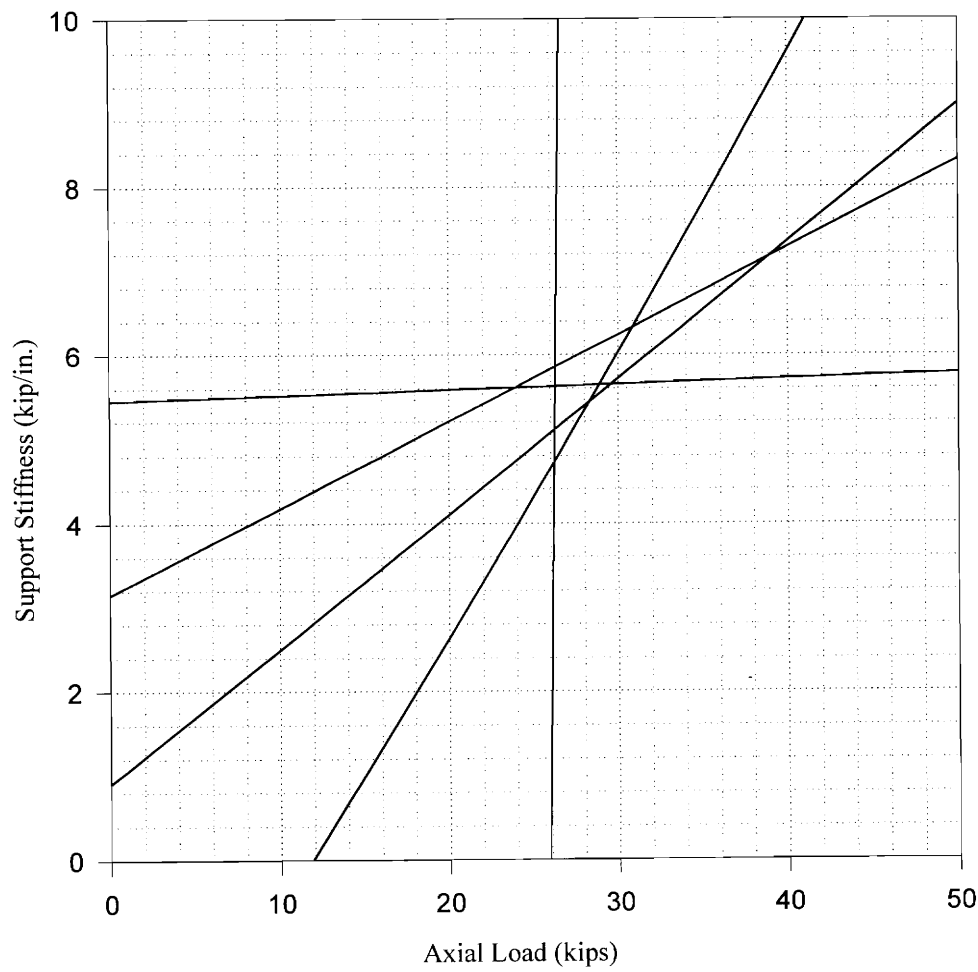


Fig.(5.39) Modified Model Contour Plot for $k_s=5.4$ kip/in. , $P=25$ kips

Estimated Loads vs. Applied Loads

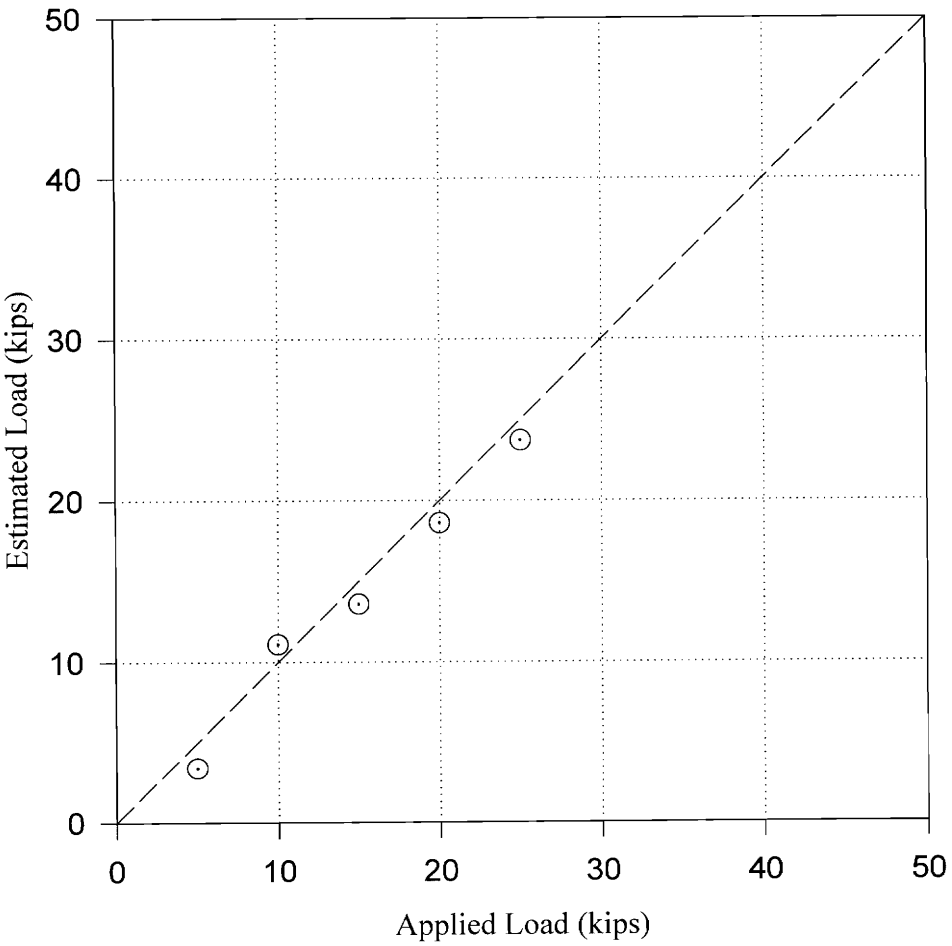


Fig.(5.40) Estimated vs. Applied Load for $k_s=2.7$ k/in. using Assumed End Stiffness

Estimated Loads vs. Applied Loads

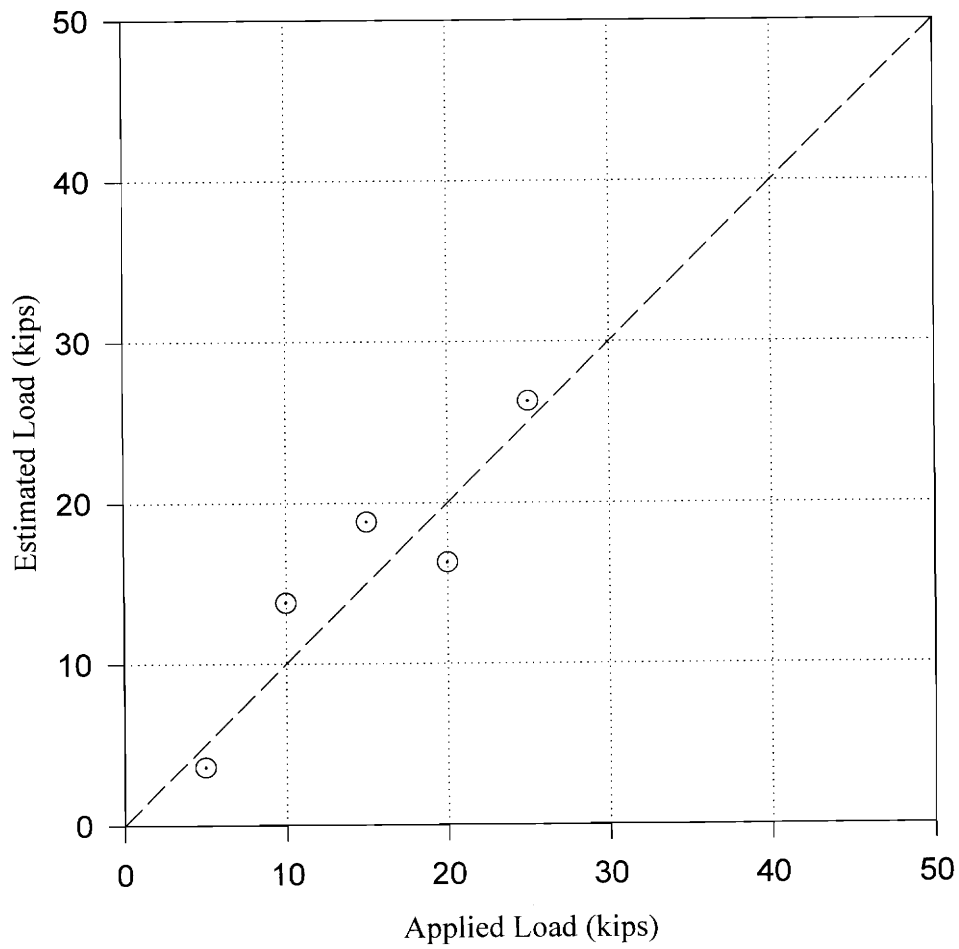


Fig.(5.41) Estimated vs. Applied Load for $k_s=5.4$ k/in. using Assumed End Stiffness

Measured and Analytical Frequencies vs. Axial Load

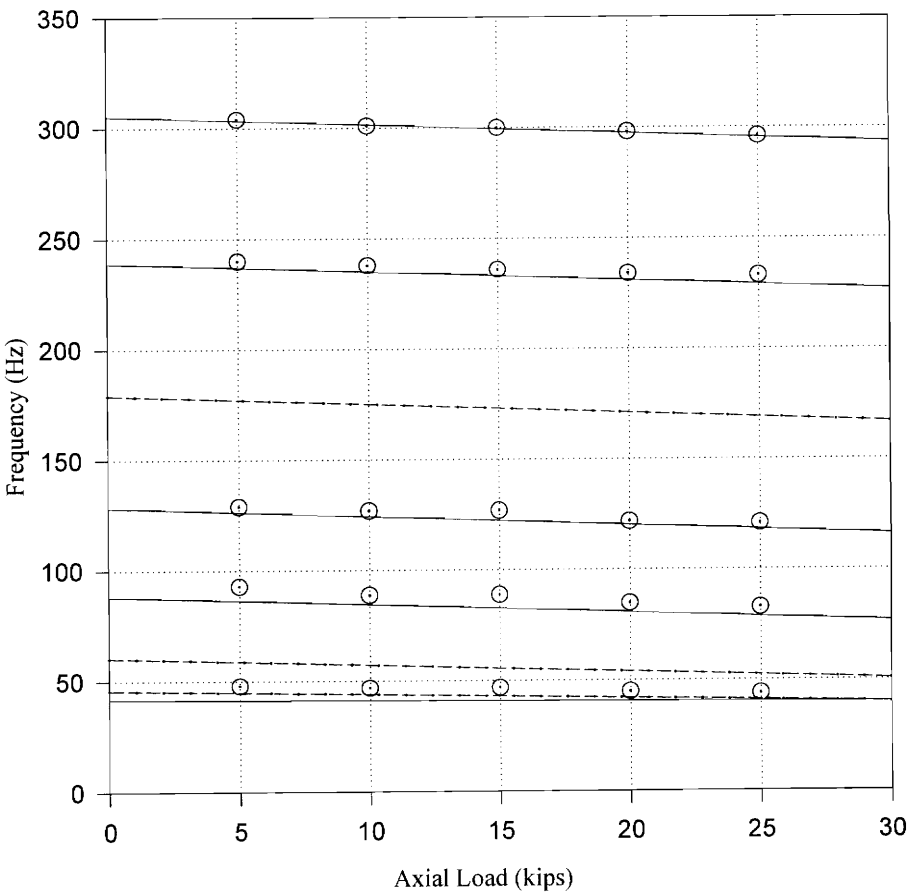


Fig.(5.42) Measured Frequencies Compared to Modified Frequencies for $k_s=2.7$ kip/in.

Measured and Analytic Frequencies vs. Axial Load

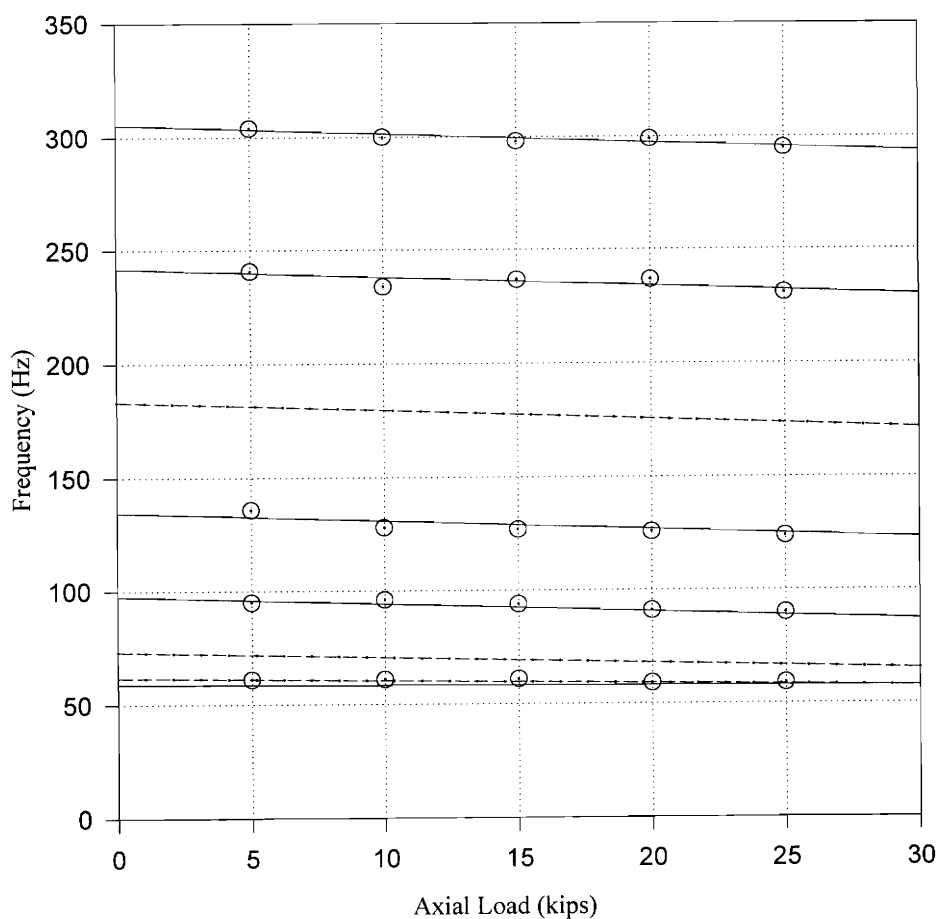


Fig.(5.43) Measured Frequencies Compared to Modified Frequencies for $k_s=5.4$ kip/in.

As figures (5.40) and (5.41) illustrate, the use of the assumed end support stiffness considerably decreased the discrepancy between the estimated and applied axial loads; however, the determination of the end support stiffness assumed that there were no other sources of error present, and therefore should not be assumed to be correct. The improvement of the results does suggest the possibility that the support stiffness was a cause of error. Comparing Figures (5.42) and (5.43) with Figures (5.15) and (5.16), the finite support stiffness had a noticeable effect on the mode 7 and mode 8 frequencies, but almost no effect on the lower modes.

Chapter 6

Conclusion

The discrete mass model and continuous model predict nearly identical frequencies for various axial loads and lateral stiffnesses. Both models confirm that the pinned-pinned mode of vibration is independent of the intermediate support stiffness. While the continuous model predicts more accurately the mode shapes of a beam, the discrete mass model is computationally more efficient.

Analysis of vibration measurements shows that the mode shapes of a beam on multiple elastic supports are clearly identifiable. The closeness of the first two natural frequencies of the beam resulted in measurement of a mixed mode shape. Both phase and magnitude of the higher modes compared well with theoretical mode shapes.

The effect of axial load on natural frequencies was determined experimentally and found to compare well to theoretical frequencies. Although measured frequencies were close to theoretical values, the small change in frequencies with increased axial load led to an average error of 13.6 kips in estimated loads. The estimated loads were consistently

higher than the applied loads since the theoretical frequencies for the 8th mode were consistently higher than the measured frequencies. The effect of a finite end support stiffness was considered, and determined to be a possible source of error. Another source of error is the 1 Hz frequency resolution of the spectrum analyzer which was necessary for the 400 Hz frequency range to be measured.

The effects of shear and rotatory inertia were investigated and found to be significant for the higher modes of vibration. A shear factor was derived which is multiplied with the frequencies of a pinned-pinned Bernoulli-Euler beam subject to axial load. For both the discrete and continuous models, the shear factor derived is exact only for the pinned-pinned mode of vibration, and can be considered only an approximation for other modes. Shear effects are even more significant for track rails, which have larger radii of gyration than the beam tested in this experiment. It is recommended that future research use Timoshenko beam theory in the development of a discrete or continuous model. A discrete model could also use a dynamic stiffness matrix instead of one based on static deflections.

Future experiments can account for the effects of end support conditions by either using experimentally determined stiffnesses in the beam model or by using longer beams so that the end support stiffness has less effect on beam vibrations.

It is also recommended that the analyzer used in future experiments be capable of fine frequency resolution due to the small change in frequency with respect to increased axial load.

References

- Clough, R. W., and Penzien, J. (1975). "Dynamics of Structures", McGraw-Hill, New York
- Cowper, G. R. (1966). "The Shear Coefficient in Timoshenko's Beam Theory", Journal of Applied Mechanics, vol.33, no.2, pp.335-340
- Ellyin, F. (1983). "Nonlinear Response and Stability of Structures", Canadian Journal of Civil Engineering, vol. 10, no.1, pp.27-35
- Grassie, S. L., Gregory, R. W., Harrison, D., and Johnson, K. L. (1982). "The Dynamic Response of Railway Track to High Frequency Vertical Excitation", Journal of Mechanical Engineering Science, vol. 24, no.2, pp.77-90
- Grassie, S. L., Gregory, R. W., and Johnson, K. L. (1982). "The Dynamic Response of Railway Track to High Frequency Lateral Excitation", Journal of Mechanical Engineering Science, vol. 24, no.2, pp.91-95
- Kerr, A. D. (1974). "The Stress and Stability Analyses of Railroad Tracks", Journal of Applied Mechanics, vol.41, no.4, pp.841-848
- Kerr, A. D. (1974). "On the Stability of the Railroad Track in the Vertical Plane", Rail International, vol.2, no.2, pp.131-142
- Kerr, A. D. (1975). "Lateral Buckling of Railroad Tracks due to Constrained Thermal Expansions- A Critical Survey", Proceedings of the Symposium on Railroad Track Mechanics, Pergamon Press, pp.141-163
- Kerr, A. D. (1976). "The Effect of Lateral Resistance on Track Buckling Analyses", Rail International, vol.7, no.1, pp.30-38
- Kerr, A. D. (1979). "Improved Stress Analysis for Cross-Tie Tracks", Journal of the Engineering Mechanics Division, ASCE, vol.105, no.4, pp.539-548
- Kerr, A. D. (1980). "An Improved Analysis for Thermal Track Buckling", International Journal of Non-Linear Mechanics, vol.15, no.2, pp.99-114

- Kerr, A. D., and Shenton, H. W. (1986). "Railroad Track Analyses and Determination of Parameters", *Journal of Engineering Mechanics*, vol.112, no.11, pp.1117-1134
- Kerr, A. D., and Zarembski, A. M. (1981). "The Response Equations for a Cross-Tie Track", *Acta Mechanica*, vol.40, no.3-4, pp.253-276
- Knothe, K.I. and Grassie, S. L. (1993). "Modeling of Railway Track and Vehicle/Track Interaction at High Frequencies", *Vehicle System Dynamics*, vol.2 no.3-4, pp.209-62
- Knothe, K.I., Strzyzakowski, Z., and Willner, K. (1994). "Rail Vibrations in the High Frequency Range", *Journal of Sound and Vibration*, vol.169, no.1, pp.111-123
- Livingston, T. S. (1993). "Determination of Axial Load by Frequency Analysis", Department of Civil Engineering, University of Vermont, Burlington
- Lusignea, R., Prah, F., and Maser, K. (1979). "The Effect of Axial Load on the Flexural Dynamic Response of a Rail", *Non-Destructive Techniques for Measuring the Longitudinal Force in Rails- Proceedings of a Joint Government-Industry Conference*, Washington, D.C., pp.86-109
- Timoshenko, S. (1915). "Strengths of Rails", *Transactions of the Institute of Ways of Communication*, St. Petersburg, Russia
- Timoshenko, S. (1926). "Method of Analysis of Statical and Dynamical Stresses in Rail", *Proceedings of the Second International Congress for Applied Mechanics*, Zürich, pp.408-418
- Timoshenko, S., and Langer, F. B. (1932). "Stresses in Railroad Track", *Journal of Applied Mechanics*, vol. 54, no.23, pp.277-302
- Winkler, E. (1875). "Der Eisenbahnoberbau" (3rd Edition), Verlag H. Dominikus, Prague
- Winkler, E. (1867). "Die Lehre von der Elastizität und Festigkeit", Verlag H. Dominikus, Prague

Appendix A

Derivation of Shear Factor

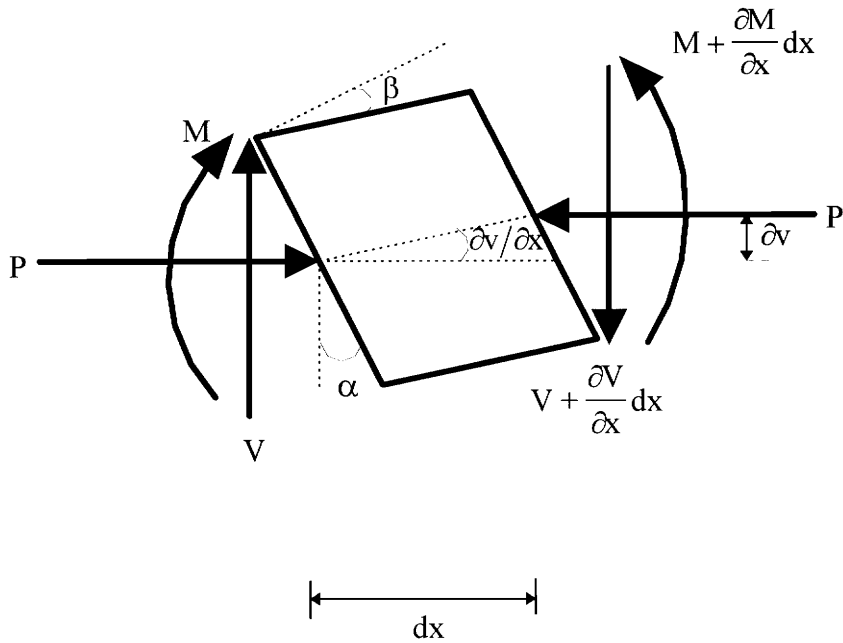


Fig.(A1.1) Differential Beam Segment Including Shear Deformation

The following derivation is similar to that given by Clough and Penzien (1975), but extended to include the effect of axial load. Consider the differential beam segment of Fig.(A1.1) which is subject to bending deformation and shear deformation. The angles

α and β represent the rotation due to bending and the shear distortion of the segment, respectively. α and β are related by

$$\beta = \alpha - \frac{\partial v}{\partial x} \quad (\text{A1.1})$$

where $\frac{\partial v}{\partial x}$ is the slope of the elastic axis. Summation of vertical forces gives

$$m \frac{\partial^2 v}{\partial t^2} dx = V - (V + \frac{\partial V}{\partial x} dx) \quad (\text{A1.2})$$

or

$$m \frac{\partial^2 v}{\partial t^2} = - \frac{\partial V}{\partial x} \quad (\text{A1.3})$$

Letting

$$V = k'AG\beta \quad , \quad (\text{A1.4})$$

where $k'A$ is the shear area of the section and G is the shear modulus, substitution into equation (A1.3) gives

$$m \frac{\partial^2 v}{\partial t^2} = - k'AG \frac{\partial \beta}{\partial x} \quad (\text{A1.5})$$

Taking the partial derivative of equation (A1.1) with respect to x and using equation (A1.5) gives

$$\frac{\partial \alpha}{\partial x} = \frac{\partial^2 v}{\partial x^2} - \frac{m}{k'AG} \frac{\partial^2 v}{\partial t^2} \quad (\text{A1.6})$$

Summing moments about the left end of the segment at the centroid gives

$$mr^2 \frac{\partial^2 \alpha}{\partial t^2} dx = -M + (M + \frac{\partial M}{\partial x} dx) - (V + \frac{\partial V}{\partial x} dx) dx + P \frac{\partial v}{\partial x} dx, \quad (A1.7)$$

which is equivalent, as $dx \rightarrow 0$, to

$$EI \frac{\partial^2 \alpha}{\partial x^2} = V + mr^2 \frac{\partial^2 \alpha}{\partial t^2} - P \frac{\partial v}{\partial x} \quad (A1.8)$$

where

$$M = EI \frac{\partial \alpha}{\partial x} \quad (A1.9)$$

and r is the radius of gyration of the cross-section. Taking the partial derivative of equation (A1.8) with respect to x and substituting equations (A1.5) and (A1.6) gives

$$EI \frac{\partial^2}{\partial x^2} \left(\frac{\partial^2 v}{\partial x^2} - \frac{m}{k'AG} \frac{\partial^2 v}{\partial t^2} \right) = -m \frac{\partial^2 v}{\partial t^2} + mr^2 \frac{\partial^2}{\partial t^2} \left(\frac{\partial^2 v}{\partial x^2} - \frac{m}{k'AG} \frac{\partial^2 v}{\partial t^2} \right) - P \frac{\partial^2 v}{\partial x^2} \quad (A1.10)$$

Rearranging and simplifying terms gives

$$EI \frac{\partial^4 v}{\partial x^4} + m \frac{\partial^2 v}{\partial t^2} + P \frac{\partial^2 v}{\partial x^2} - m^2 r^2 \frac{\partial^4 v}{\partial x^2 \partial t^2} - \frac{EI m}{k'AG} \frac{\partial^4 v}{\partial x^2 \partial t^2} + \frac{m^2 r^2}{k'AG} \frac{\partial^4 v}{\partial t^4} = 0 \quad (A1.11)$$

The first two terms in equation (A1.11) represent the basic case of transverse vibration for a Bernoulli-Euler beam. The third term represents the effect of axial load. The fourth and fifth terms represent the effects of rotatory inertia and shear deformation, respectively, and the last term represents a combined effect of shear deformation and rotatory inertia.

For the case of a pinned-pinned beam, we assume a displacement of the form

$$v(x, t) = A \sin\left(\frac{n\pi}{L} x\right) \sin(\omega t) \quad (A1.12)$$

which is identical to equation (2.16) which was derived for a pinned-pinned beam on a Winkler foundation. Substituting equation (A1.12) into equation (A1.11) gives

$$\left(\frac{n\pi}{L}\right)^4 - a^4 - \frac{P}{EI}\left(\frac{n\pi}{L}\right)^2 - a^4 r^2 \left(\frac{n\pi}{L}\right)^2 \left(1 + \frac{E}{k'G}\right) + a^4 r^2 \left(a^4 r^2 \frac{E}{k'G}\right) = 0 \quad (A1.13)$$

where

$$a^4 = \frac{m\omega_n^2}{EI} \quad (A1.14)$$

Since

$$a^4 \approx \left(\frac{n\pi}{L}\right)^4, \quad (A1.15)$$

which is a small number for the cases under consideration, the last term in equation (A1.13) is much smaller than the other terms, and can be ignored. Omitting this term and solving equation (A1.13) for a^4 gives

$$a^4 = \frac{\left(\frac{n\pi}{L}\right)^4 - \frac{P}{EI}\left(\frac{n\pi}{L}\right)^2}{\left[1 + r^2 \left(\frac{n\pi}{L}\right)^2 \left(1 + \frac{E}{k'G}\right)\right]} \quad (A1.16)$$

Substituting for a^4 and solving for ω_n gives

$$\omega_n = \frac{\left\{ \frac{1}{m} \left[EI \left(\frac{n\pi}{L}\right)^4 - P \left(\frac{n\pi}{L}\right)^2 \right] \right\}^{\frac{1}{2}}}{\left[1 + r^2 \left(\frac{n\pi}{L}\right)^2 \left(1 + \frac{E}{k'G}\right) \right]^{\frac{1}{2}}} \quad (A1.17)$$

Equation (A1.17) represents the natural frequency of a pinned-pinned beam subject to an axial load, including the effects of shear deformation and rotatory inertia. Equation (A1.17) can be rewritten as

$$\omega_n = \Phi_n \cdot \left\{ \frac{1}{m} \left[EI \left(\frac{n\pi}{L} \right)^4 - P \left(\frac{n\pi}{L} \right)^2 \right] \right\}^{\frac{1}{2}} \quad (\text{A1.18})$$

where

$$\Phi_n = \left[1 + r^2 \left(\frac{n\pi}{L} \right)^2 \left(1 + \frac{E}{k'G} \right) \right]^{-\frac{1}{2}} \quad (\text{A1.19})$$

The bracketed expression in equation (A1.18) represents the frequency of a pinned-pinned Bernoulli-Euler beam with axial load. Φ_n is a frequency reduction factor which accounts for the effects of shear deformation and rotatory inertia. The shear factor, Φ_n , is a function of the beam cross-section properties as well as the mode of vibration. As equation (A1.19) indicates, the effect of shear and rotatory inertia increases with mode number.

Appendix B

Discrete Mass Model Code

The computer program, **discrete.m**, contained in this appendix was written for MATLAB. The program determines frequencies and eigenvectors for a continuous Bernoulli-Euler beam with a compressive axial load on equally spaced elastic supports. The program assembles mass and stiffness matrices for the discretized system. The stiffness matrix is reduced to include only transverse degrees of freedom. Frequencies and eigenvectors are sorted according to mode number. Frequencies are calculated for various axial loads. Discrete mass model frequencies are plotted vs. axial load and compared to Winkler foundation model frequencies. Data for mesh plots in Fig.(3.11) to Fig.(3.18) are generated by using the program, **discrete.m**, in this appendix with various intermediate support stiffnesses.

```
% discrete.m - THIS MATLAB PROGRAM CALCULATES NATURAL
% FREQUENCIES FOR A CONTINUOUS BEAM WITH A COMPRESSIVE AXIAL
% LOAD AND EQUALLY SPACED LATERAL SUPPORTS USING A DISCRETE
% MASS APPROXIMATION
```

```
% INPUT VARIABLES *****
numsprings = 9      ;    % NUMBER OF SPRINGS (INCLUDING END SPRINGS)
L = 192             ;    % LENGTH OF MEMBER (inches)
I = 0.764           ;    % MOMENT OF INERTIA OF SECTION (in.^4)
A = 2.26            ;    % AREA OF CROSS-SECTION (in.^2)
E = 29000.          ;    % ELASTIC MODULUS OF MEMBER (ksi)
rho = .000283       ;    % WEIGHT DENSITY OF STEEL (k/in.^3)
g = 386             ;    % ACCELERATION DUE TO GRAVITY (in./s^2)
kdefault = 5.4      ;    % DEFAULT SPRING STIFFNESS (k/in.)
```

```
springs = kdefault*ones(numsprings,1);
```

```
% SPECIFY SPECIFIC SPRING STIFFNESSES AFTER THIS LINE *****
springs(1) = 10000000;                                     %*
springs(numsprings) = 10000000;                             %*
%*****
```

```
% LOCAL VARIABLES *****
n = 8*(numsprings-1)+2;    % DEG. OF FREEDOM OF INITIAL SYSTEM
numelements = n/2-1;       % NUMBER OF BEAM ELEMENTS TO BE
                           % ASSEMBLED
dof = numelements+1;       % DEG. OF FREEDOM OF REDUCED SYSTEM
l = L/numelements;         % LENGTH OF ELEMENTS BETWEEN MASSES
kspacing= L/(numsprings-1); % DISTANCE BETWEEN SPRINGS
num_modes = 8;             % NUMBER OF MODES TO RANK
Pmin = 0.01;               % SMALLEST LOAD TO APPLY TO SYSTEM
Pmax = 2*sqrt(kdefault*E*I/kspacing; % LARGEST LOAD TO APPLY TO SYSTEM
num_loads = 30;            % TOTAL NUMBER OF LOADS TO APPLY TO
                           % SYSTEM
P = linspace(Pmin,Pmax,num_loads);
```

```
% INITIALIZE MATRICES
WFREQ = zeros(num_modes, num_loads);
DMFREQ = zeros(num_modes, num_loads);
```

```
for c=1:num_loads
```



```

% CREATE ELEMENT STIFFNESS MATRIX *****
Kel = zeros(4,4);

k = sqrt(P(c)/(E*I));
% STABILITY FUNCTIONS
phic = 2-2*cos(k*l)-k*l*sin(k*l);
phi1 = (k*l)^3*sin(k*l)/(12*phic);
phi2 = (k*l)^2*(1-cos(k*l))/(6*phic);
phi3 = k*l*(sin(k*l)-k*l*cos(k*l))/(4*phic);
phi4 = k*l*(k*l-sin(k*l))/(2*phic);

alpha = E*I/l^3;
Kel(1,1) = alpha*12*phi1;
Kel(1,2) = alpha*6*l*phi2;
Kel(1,3) = -alpha*12*phi1;
Kel(1,4) = alpha*6*l*phi2;
Kel(2,2) = alpha*4*l^2*phi3;
Kel(2,3) = -alpha*6*l*phi2;
Kel(2,4) = alpha*2*l^2*phi4;
Kel(3,3) = alpha*12*phi1;
Kel(3,4) = -alpha*6*l*phi2;
Kel(4,4) = alpha*4*l^2*phi3;
Kel(2,1) = Kel(1,2);
Kel(3,1) = Kel(1,3);
Kel(3,2) = Kel(2,3);
Kel(4,1) = Kel(1,4);
Kel(4,2) = Kel(2,4);
Kel(4,3) = Kel(3,4);

% ASSEMBLE GLOBAL STIFFNESS MATRIX *****
Kglobal = zeros(n,n);
for a=1:numelements
    b=2*a-1;
    Kglobal(b:b+3,b:b+3) = Kglobal(b:b+3,b:b+3)+Kel;
end

% ADD SPRING STIFFNESSES TO STIFFNESS MATRIX *****
for a=1:8:n-1
    % THE FOLLOWING LINE MUST BE MODIFIED IF NUMBER OF SPRINGS OR
    % BEAM ELEMENTS IS CHANGED
    Kglobal(a,a) = Kglobal(a,a) + springs((a+7)/8);

```

```

end

% REDUCE Kglobal *****
F = zeros(n,dof);
for a=1:dof
    F(2*a-1,a) = 1;
end

Dglobal = Kglobal\F;
D = Dglobal(1:2:n-1,:);
K = inv(D);

% CREATE REDUCED MASS MATRIX *****
M = diag(ones(dof,1));
M(1,1) = 0.5;
M(dof,dof) = 0.5;
M = (A*rho*l/g)*M;

% SOLVE FOR EIGENVALUES *****
[x,values] = eig(K,M);
omega2 = diag(values);

% RANK FREQUENCIES ACCORDING TO MODE SHAPE *****
for a=1:dof
    count=1;
    for b=2:dof-2
        if x(b,a)*x(b+1,a)<=0
            if x(b,a)~=0
                count = count + 1;
            end
        end
    end
    mode(a) = count;
end

[dummy,rank] = sort(mode);
freq = sqrt(omega2(rank))/(2*pi);
% ADD SORTED FREQUENCIES TO DMFREQ
DMFREQ(:,c) = real(freq(1:num_modes));

% GENERATE FREQUENCIES FOR WINKLER FOUNDATION MODEL *****

```

```

for d=1:num_modes
WFREQ(d,c)=sqrt((E*I*(d*pi/L)^4-
P(c)*(d*pi/L)^2+kdefault/kspacing)*g/(A*rho))/(2*pi);
end

```

```

end

```

```

% PLOT RESULTS *****

```

```

plot (P,WFREQ(1:4,:), 'b--',P,DMFREQ(1:4,:), 'k-')
title('Winkler(-- ) and Discrete Mass(-) Frequencies vs. Load for n=1-4')
xlabel('Axial Load (kips)')
ylabel('Frequency (Hz)')
grid
pause

```

```

plot (P,WFREQ(5:8,:), 'b--',P,DMFREQ(5:8,:), 'k-')
title('Winkler(-- ) and Discrete Mass(-) Frequencies vs. Load for n=5-8')
xlabel('Axial Load (kips)')
ylabel('Frequency (Hz)')
grid

```

Appendix C

Continuous Model Code

The computer program, **contin.m**, contained in this appendix was written for MATLAB. The program determines frequencies and eigenvectors for a continuous Bernoulli-Euler beam with a compressive axial load on equally spaced elastic supports. The program uses a continuous model which yields an exact solution for Bernoulli-Euler beam theory. The program assembles a characteristic matrix, **CM**, the determinant of which is zero for natural frequencies of vibration. Natural frequencies are determined through an iterative process by calculating $\det(\mathbf{CM})$ for incremental values of frequency, ω , until the determinant experiences a sign change. The method requires a very small frequency increment. To significantly reduce the run time of the program, initial values for frequency iteration are determined based on discrete mass model frequencies calculated with the program **discrete.m** (Appendix 2). **contin.m** requires the variables **P** (applied axial loads) and **DMFREQ** (discrete model frequencies) which are calculated in **discrete.m**. Frequencies and eigenvectors are sorted according to mode number. Frequencies are calculated for various axial loads. Continuous model frequencies are stored in the matrix **CMFREQ**. The program plots the mode shape for each natural frequency determined.

```
% contin.m - THIS PROGRAM CALCULATES NATURAL FREQUENCIES OF A
% CONTINUOUS BEAM WITH A COMPRESSIVE AXIAL LOAD ON EQUALLY
% SPACED ELASTIC SUPPORTS. THE PROGRAM USES A CONTINUOUS
% MODEL WHICH GIVES AN EXACT SOLUTION FOR BERNOULLI-EULER
% BEAM THEORY
```

```
% INPUT VARIABLES
```

```
*****
```

```
numsprings = 9;      % NUMBER OF SPRINGS (INCLUDING END SPRINGS)
L = 192;             % LENGTH OF MEMBER (inches)
I = 0.764;           % MOMENT OF INERTIA OF SECTION (in^4)
A = 2.26;            % AREA OF CROSS-SECTION (in^2)
E = 29000.;          % ELASTIC MODULUS OF MEMBER (ksi)
rho = .000283;       % WEIGHT DENSITY OF MEMBER (k/in^3)
g = 386;             % ACCELERATION DUE TO GRAVITY (in/s^2)
kdefault = 2.7;      % DEFAULT SPRING STIFFNESS (k/in)
krotdefault = 0;     % DEFAULT ROTATIONAL SPRING STIFFNESS (k-in/in)
num_modes = 8;       % NUMBER OF MODES TO EVALUATE
```

```
k = kdefault*ones(numsprings,1);
```

```
% DESIGNATE SPECIFIC SUPPORT STIFFNESSES AFTER THIS LINE *****
```

```
k(1) = 10000000;      %*
k(numsprings) = 10000000; %*
%*****
```

```
krot = krotdefault*ones(numsprings,1);
```

```
% DESIGNATE SPECIFIC ROTATIONAL STIFFNESSES AFTER THIS LINE
```

```
% LOCAL VARIABLES *****
```

```
numelements = numsprings-1; % NUMBER OF BEAM ELEMENTS
l = L/numelements;          % LENGTH OF EACH ELEMENT
m = A*rho/g;                % MASS OF BEAM PER UNIT LENGTH
EI = E*I;
n4 = 4*numelements;
```

```
deltaf=.01;                % INCREMENT OF f
```

```
% INITIALIZE FREQUENCIES
```

```
CMFREQ=zeros(size(DMFREQ));
```

```
%*****
```

```
for p=1:num_loads
```

```

figure(1)
hold
grid

flag = 0;
mode_count = 0;
test = -1;

while mode_count < num_modes
fmin = (DMFREQ(mode_count+1,p)-.2)*2*pi;  % SMALLEST FREQUENCY TO
                                          % EVALUATE

flag2 = mode_count;
if flag == 0
    f = fmin;
end

% CREATE CHARACTERISTIC MATRIX (CM) *****
root1 = (-P(p) + sqrt(P(p)^2 + 4*EI*m*f^2))/2/EI;
root2 = (-P(p) - sqrt(P(p)^2 + 4*EI*m*f^2))/2/EI;

% FOUR WAVE NUMBERS
lambda1 = sqrt(root1);
lambda2 = -sqrt(root1);
lambda3 = sqrt(root2);
lambda4 = -sqrt(root2);

CM = zeros(4*numelements,4*numelements);

% LEFT END SUPPORT *****

% SHEAR B.C.
shear(1) = k(1) + EI*lambda1^3 + P(p)*lambda1;
shear(2) = k(1) + EI*lambda2^3 + P(p)*lambda2;
shear(3) = k(1) + EI*lambda3^3 + P(p)*lambda3;
shear(4) = k(1) + EI*lambda4^3 + P(p)*lambda4;
CM(1,1:4) = shear(1:4);

% MOMENT B.C.
moment(1) = krot(1)*lambda1 - EI*lambda1^2;
moment(2) = krot(1)*lambda2 - EI*lambda2^2;
moment(3) = krot(1)*lambda3 - EI*lambda3^2;
moment(4) = krot(1)*lambda4 - EI*lambda4^2;
CM(2,1:4) = moment(1:4);

```

```
% INTERMEDIATE SUPPORTS *****
```

```
for spring = 2:numsprings-1
```

```
    x = 1*(spring-1);
    c1 = exp(lambda1*x);
    c2 = exp(lambda2*x);
    c3 = exp(lambda3*x);
    c4 = exp(lambda4*x);
```

```
% SHEAR B.C.
```

```
shear(1) = (-EI*lambda1^3 + k(spring))*c1;
shear(2) = (-EI*lambda2^3 + k(spring))*c2;
shear(3) = (-EI*lambda3^3 + k(spring))*c3;
shear(4) = (-EI*lambda4^3 + k(spring))*c4;
shear(5) = EI*lambda1^3*c1;
shear(6) = EI*lambda2^3*c2;
shear(7) = EI*lambda3^3*c3;
shear(8) = EI*lambda4^3*c4;
CM(4*(spring-1)-1,(spring-2)*4+1:(spring-2)*4+8) = shear;
```

```
% MOMENT B.C.
```

```
moment(1) = (EI*lambda1^2 + krot(spring))*c1;
moment(2) = (EI*lambda2^2 + krot(spring))*c2;
moment(3) = (EI*lambda3^2 + krot(spring))*c3;
moment(4) = (EI*lambda4^2 + krot(spring))*c4;
moment(5) = -EI*lambda1^2*c1;
moment(6) = -EI*lambda2^2*c2;
moment(7) = -EI*lambda3^2*c3;
moment(8) = -EI*lambda4^2*c4;
CM(4*(spring-1),(spring-2)*4+1:(spring-2)*4+8) = moment;
```

```
% DEFLECTION B.C.
```

```
def = [c1 c2 c3 c4 -c1 -c2 -c3 -c4];
CM(4*(spring-1)+1, (spring-2)*4+1:(spring-2)*4+8) = def;
```

```
% SLOPE B.C.
```

```
slope1 = [lambda1*c1 lambda2*c2 lambda3*c3 lambda4*c4];
slope = [slope1 -slope1];
CM(4*(spring-1)+2,(spring-2)*4+1:(spring-2)*4+8) = slope;
```

```
end
```

```
% RIGHT END SUPPORT *****
```

```
x = L;
c1 = exp(lambda1*x);
```

```

c2 = exp(lambda2*x);
c3 = exp(lambda3*x);
c4 = exp(lambda4*x);

% SHEAR B.C.
shear(1) = (-k(numsprings) + EI*lambda1^3 + P(p)*lambda1)*c1;
shear(2) = (-k(numsprings) + EI*lambda2^3 + P(p)*lambda2)*c2;
shear(3) = (-k(numsprings) + EI*lambda3^3 + P(p)*lambda3)*c3;
shear(4) = (-k(numsprings) + EI*lambda4^3 + P(p)*lambda4)*c4;
CM(4*numelements-1,4*numelements-3:4*numelements) = shear(1:4);

% MOMENT B.C.
moment(1) = (krot(numsprings)*lambda1 + EI*lambda1^2)*c1;
moment(2) = (krot(numsprings)*lambda2 + EI*lambda2^2)*c2;
moment(3) = (krot(numsprings)*lambda3 + EI*lambda3^2)*c3;
moment(4) = (krot(numsprings)*lambda4 + EI*lambda4^2)*c4;
CM(4*numelements,4*numelements-3:4*numelements) = moment(1:4);

% CALCULATE DETERMINANT OF CHARACTERISTIC MATRIX
dete = det(CM);
deter = sign(real(dete))*log(abs(real(dete)));
dcm = [dcm deter];

% CHECK IF DETERMINANT PASSES THROUGH ZERO
if deter*test <= 0
if flag == 1
    CMsub = CM(2:n4, 2:n4);
    row1 = -CM(2:n4,1);
    C = CMsub\row1;
    C = [1 ; C];
    for el=1:numelements
        x = linspace((el-1)*l, el*l, 13);
        if el == numelements
            smax = 13;
        else
            smax = 12;
        end
        for s = 1:smax
            shape((el-1)*12+s) = C((el-1)*4+1)*exp(lambda1*x(s)) + C((el-1)*4+2)*exp(lambda2*x(s)) + C((el-1)*4+3)*exp(lambda3*x(s)) + C((el-1)*4+4)*exp(lambda4*x(s));
        end
    beam = linspace(0, L, 12*numelements+1);
end

```



```

% PLOT MODE SHAPE
shape=real(shape./max(abs(shape)));
plot(beam, shape,'b')
axis([0 L -1.1 1.1])
title(num2str(f/2/pi))

freq = [freq f/2/pi];
test = deter;
fre =f/2/pi;
mode_count = mode_count + 1;
CMFREQ(mode_count,p)=fre;
[p mode_count]
flag = 0;
else
    test= -test;
    end
end

if flag2 < mode_count
    flag = 0;
else
    flag = 1;
end

hz = [hz f/2/pi];
f = f+deltaf;
end
%pause
%clf
end

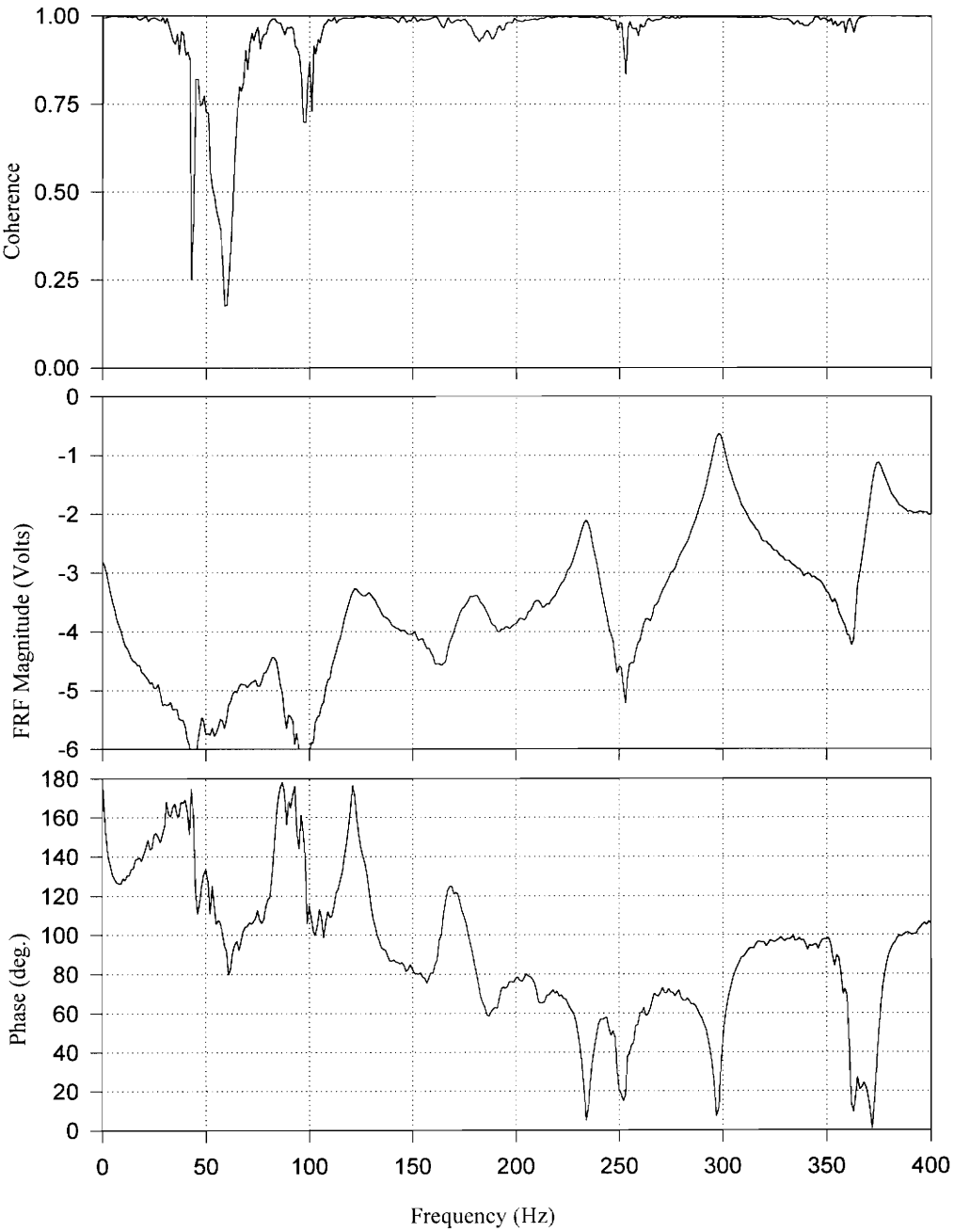
```

Appendix D

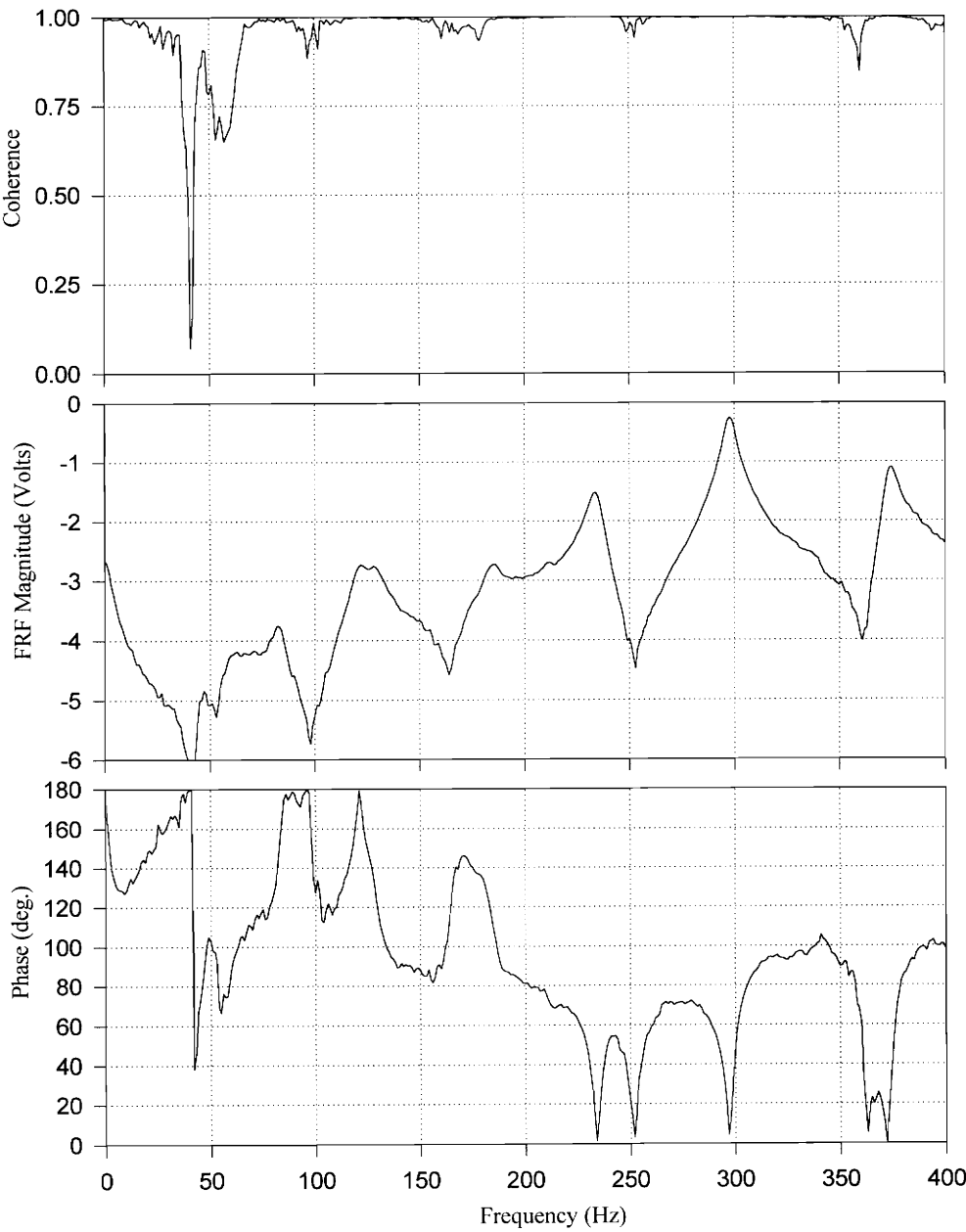
Data for Mode Shape Determination in Section 5.4

Data contained in this section were used for the sample mode shapes determined in section 5.4 . These data were recorded for a 20 kip axial load and an intermediate support stiffness of 2.7 kip/in. . Each page contains a coherence, FRF, and phase trace for measurements taken at one of the 16 measurement positions along the length of the test beam. Odd numbered positions were 5 in. to the right of a support and even numbered positions were midspan between supports. FRF's are plotted on a logarithmic scale. Each FRF is an average of 3 measurements. The coherence plots are a measure of the correlation between the 3 measurements where a coherence of 1 indicates a perfect correlation and a coherence of 0 indicates no correlation.

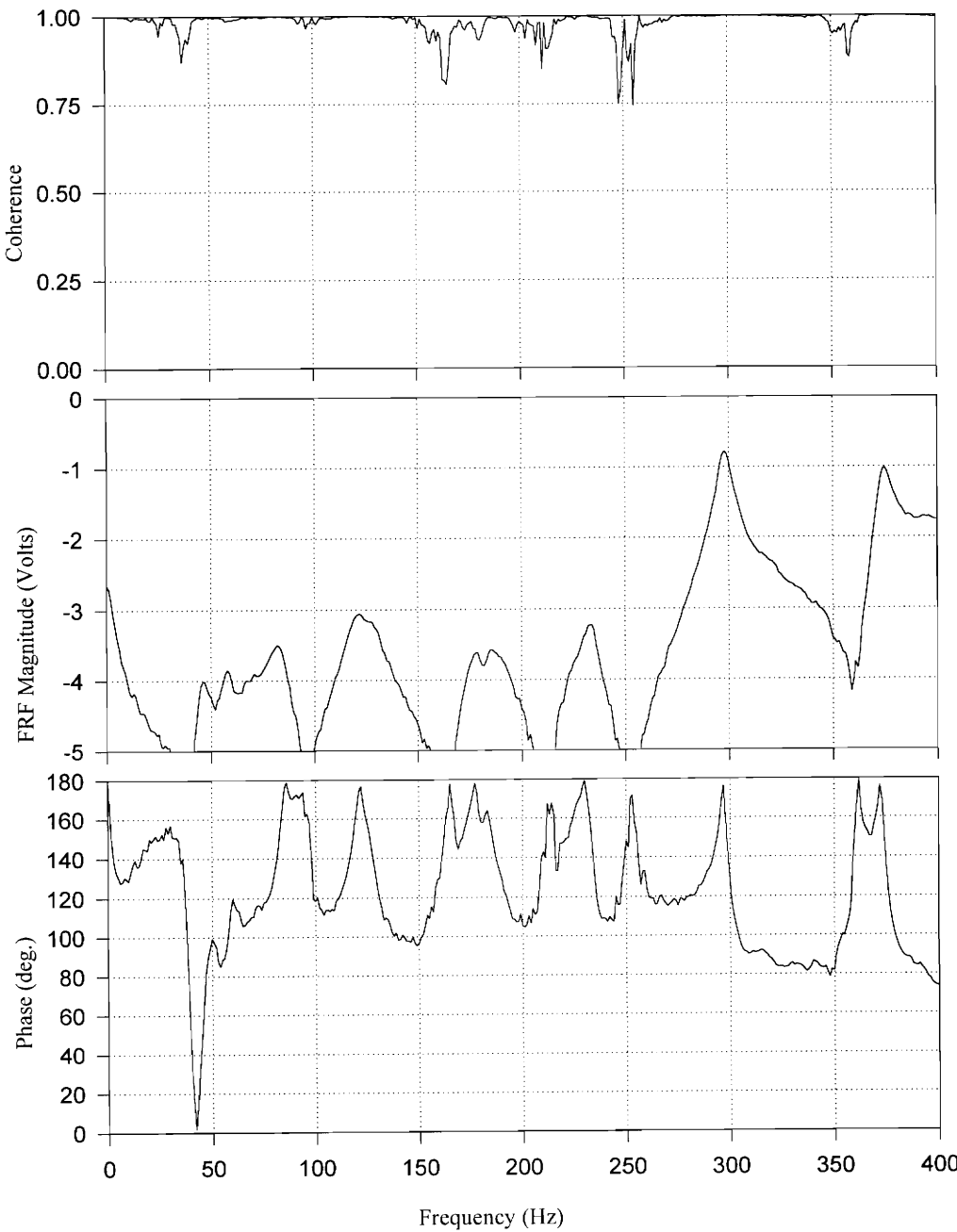
Position 1 Measurement

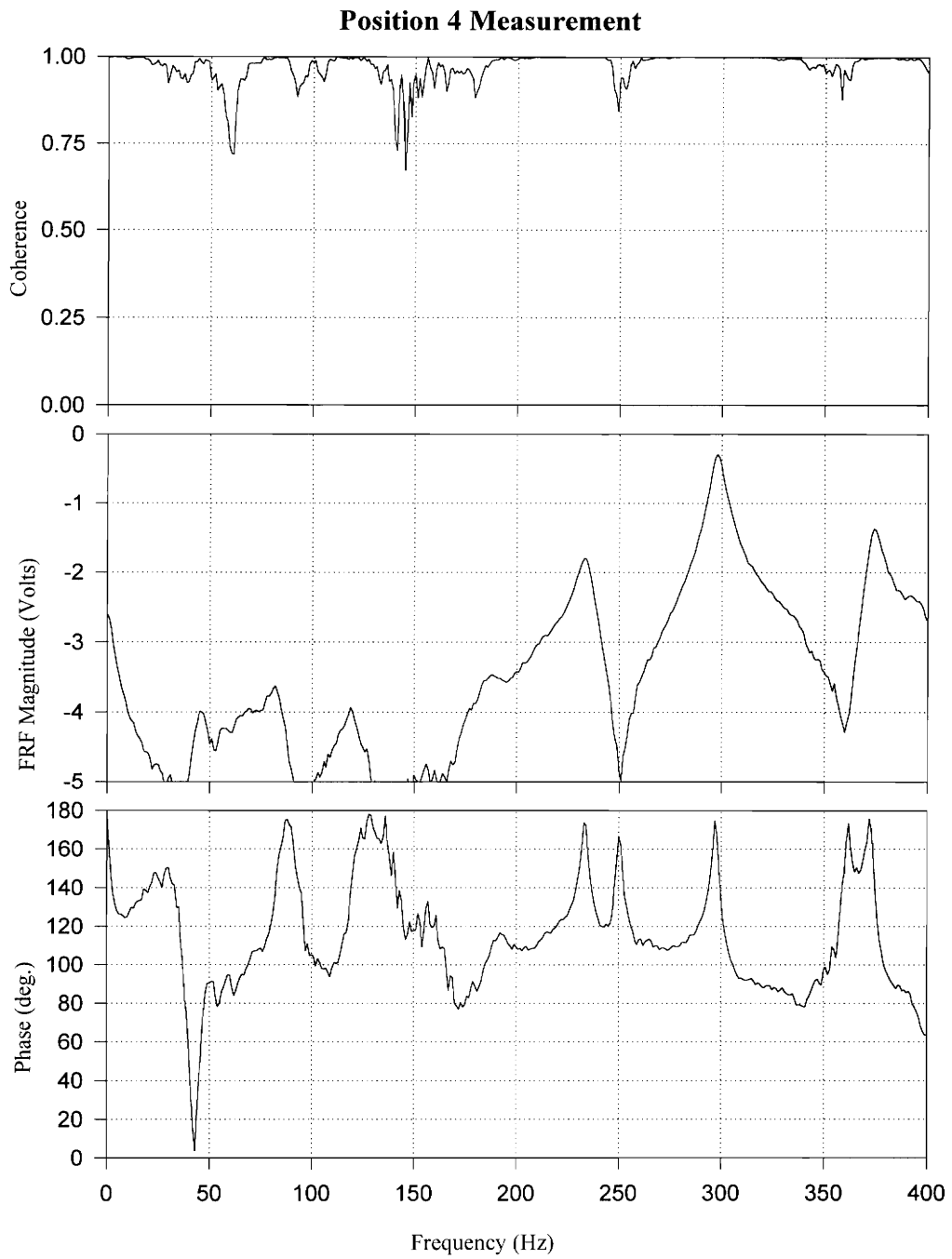


Position 2 Measurement

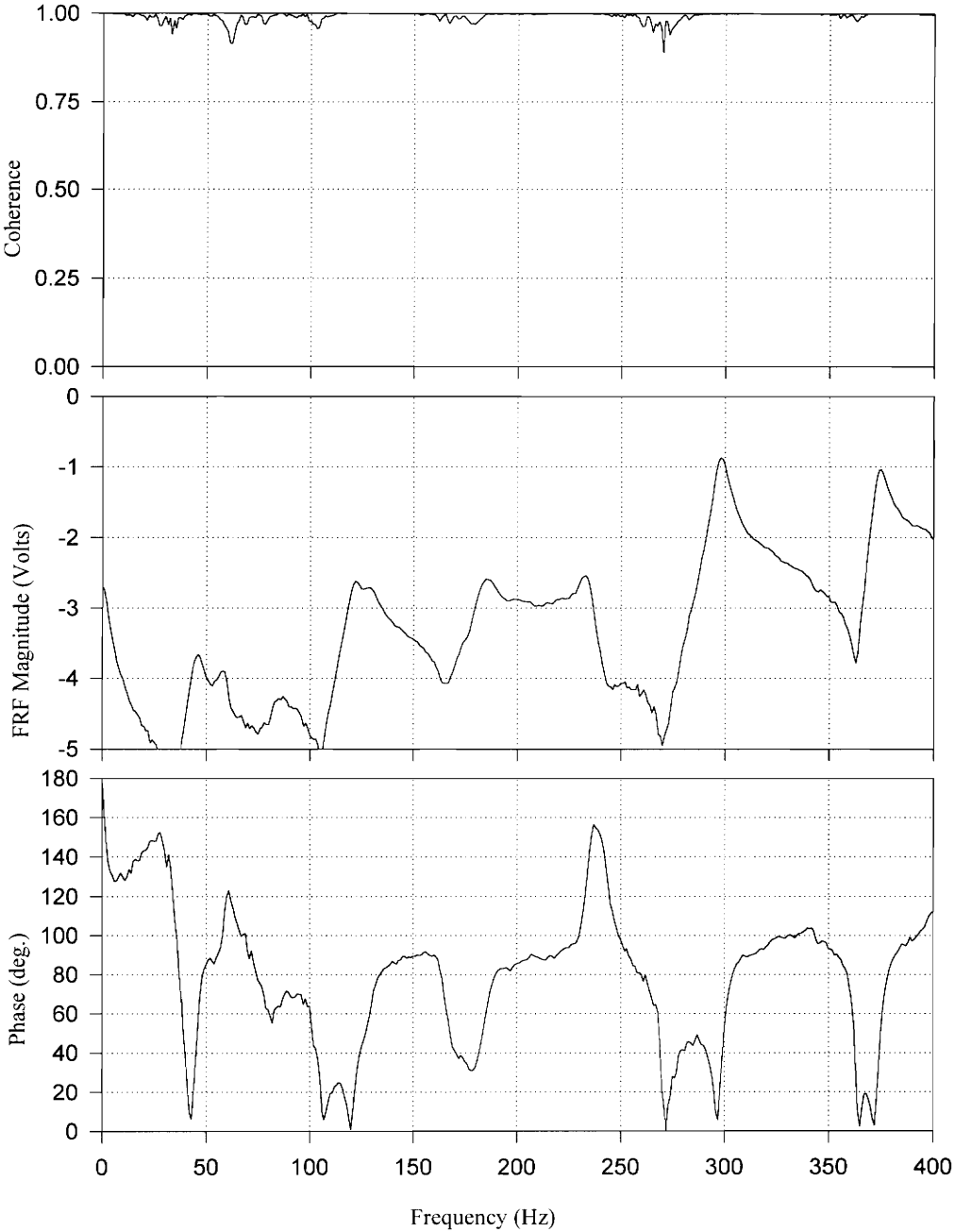


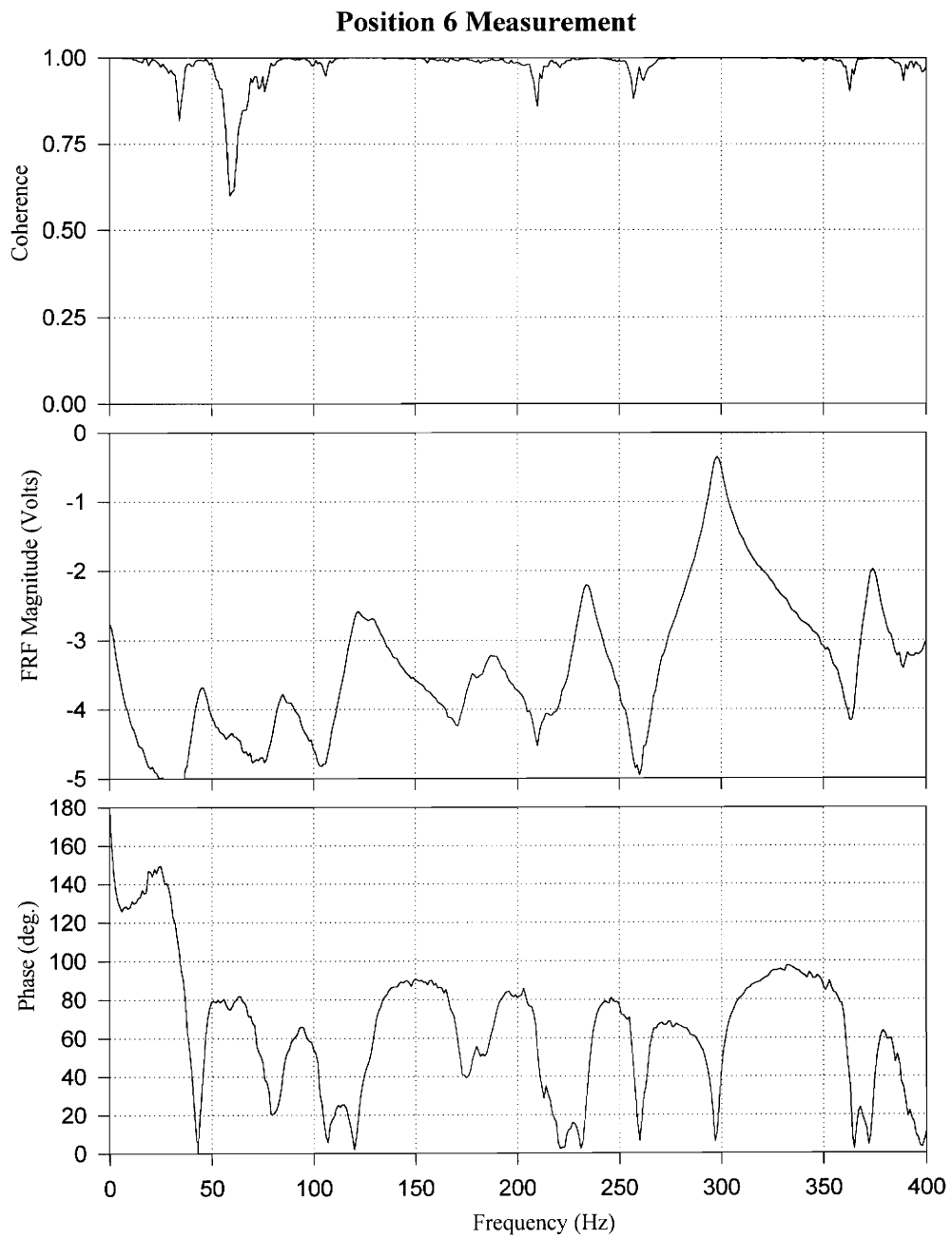
Position 3 Measurement



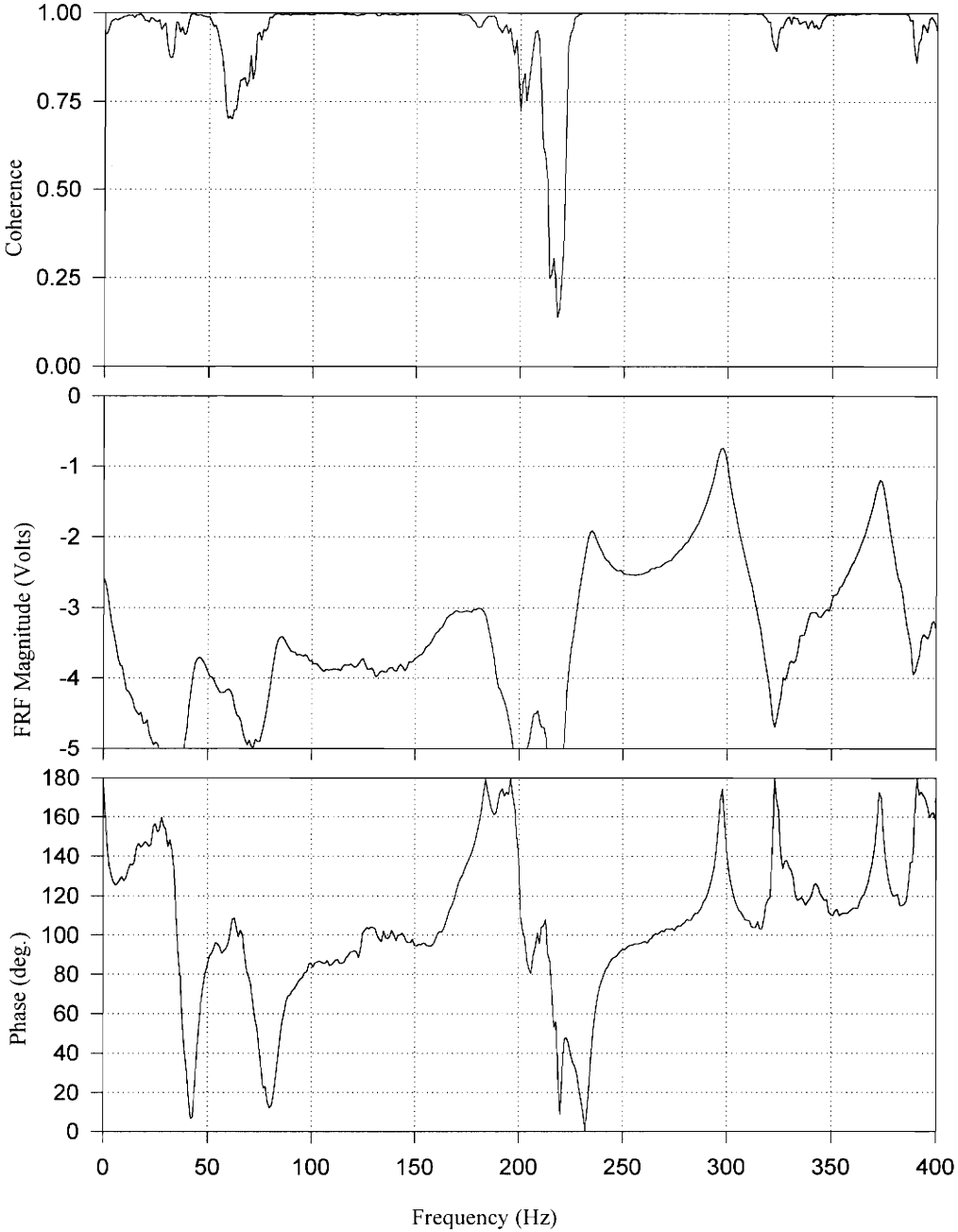


Position 5 Measurement

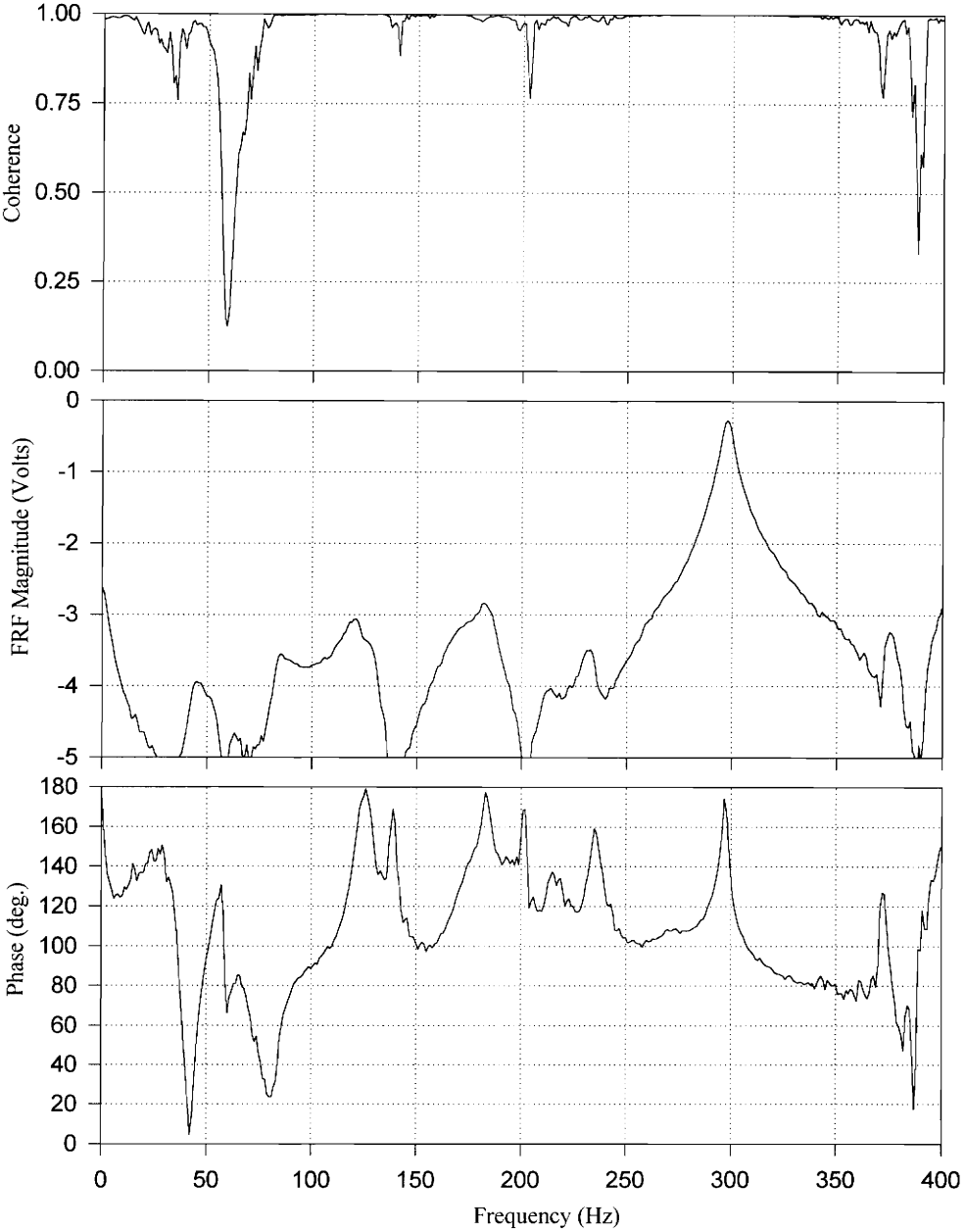




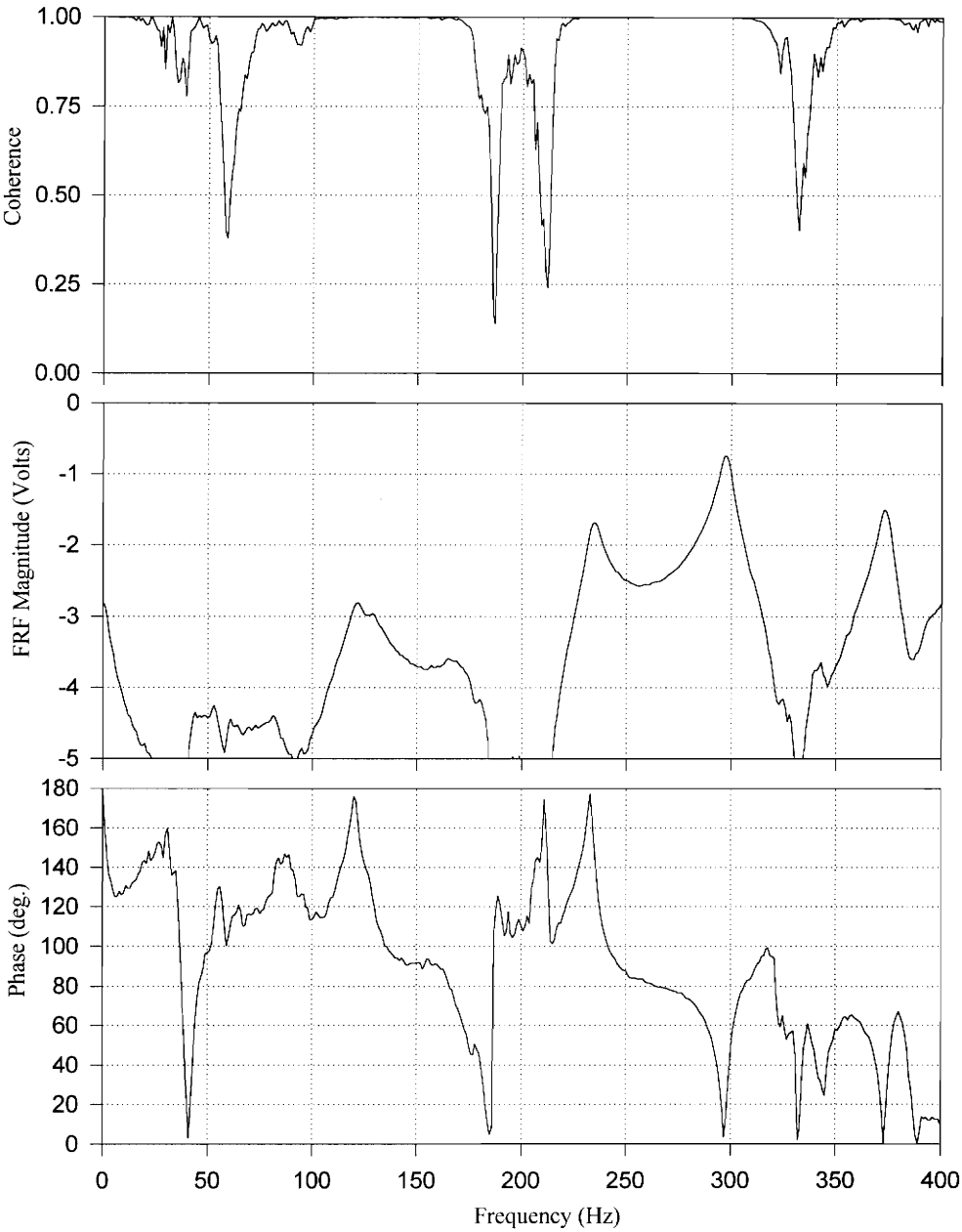
Position 7 Measurement



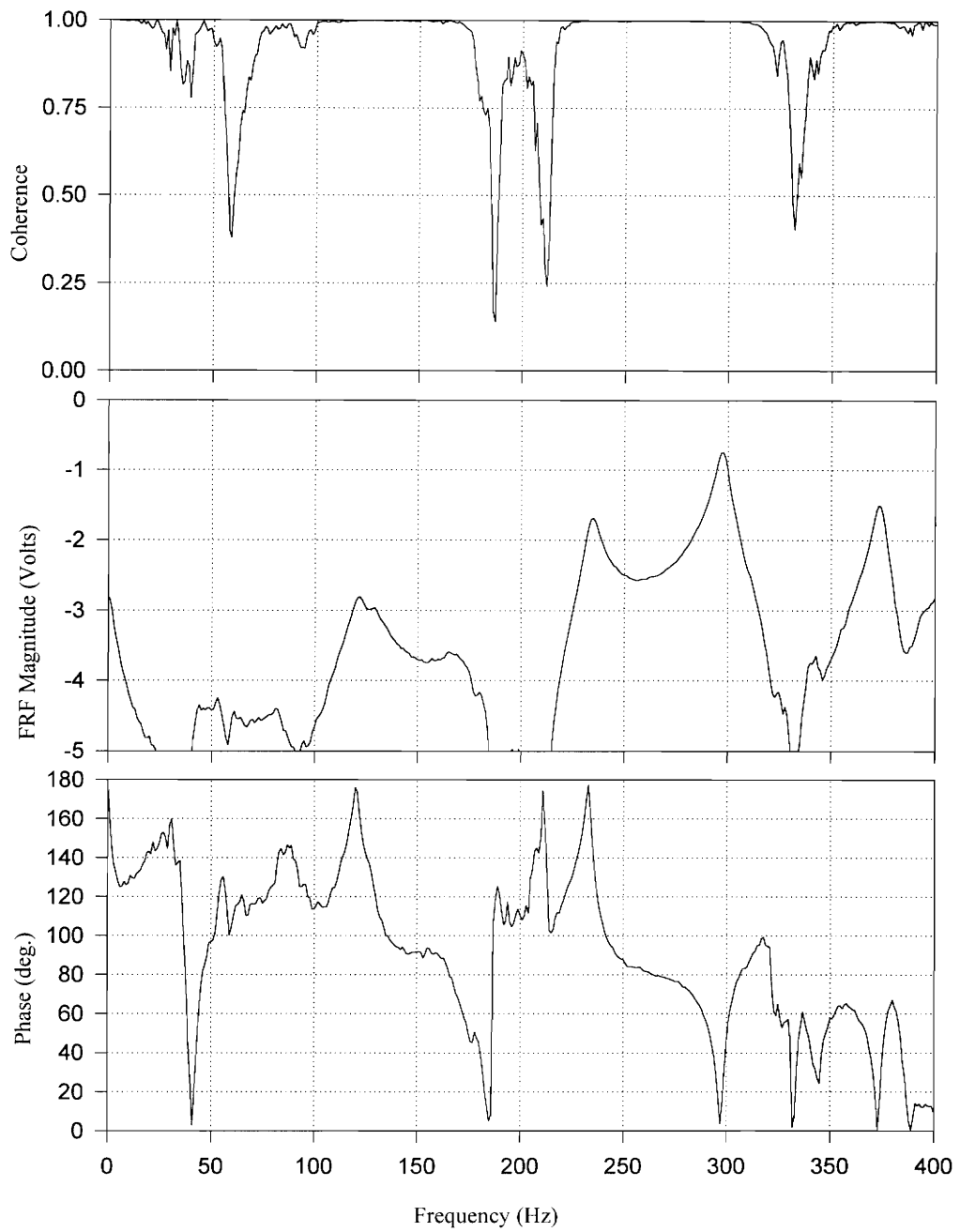
Position 8 Measurement



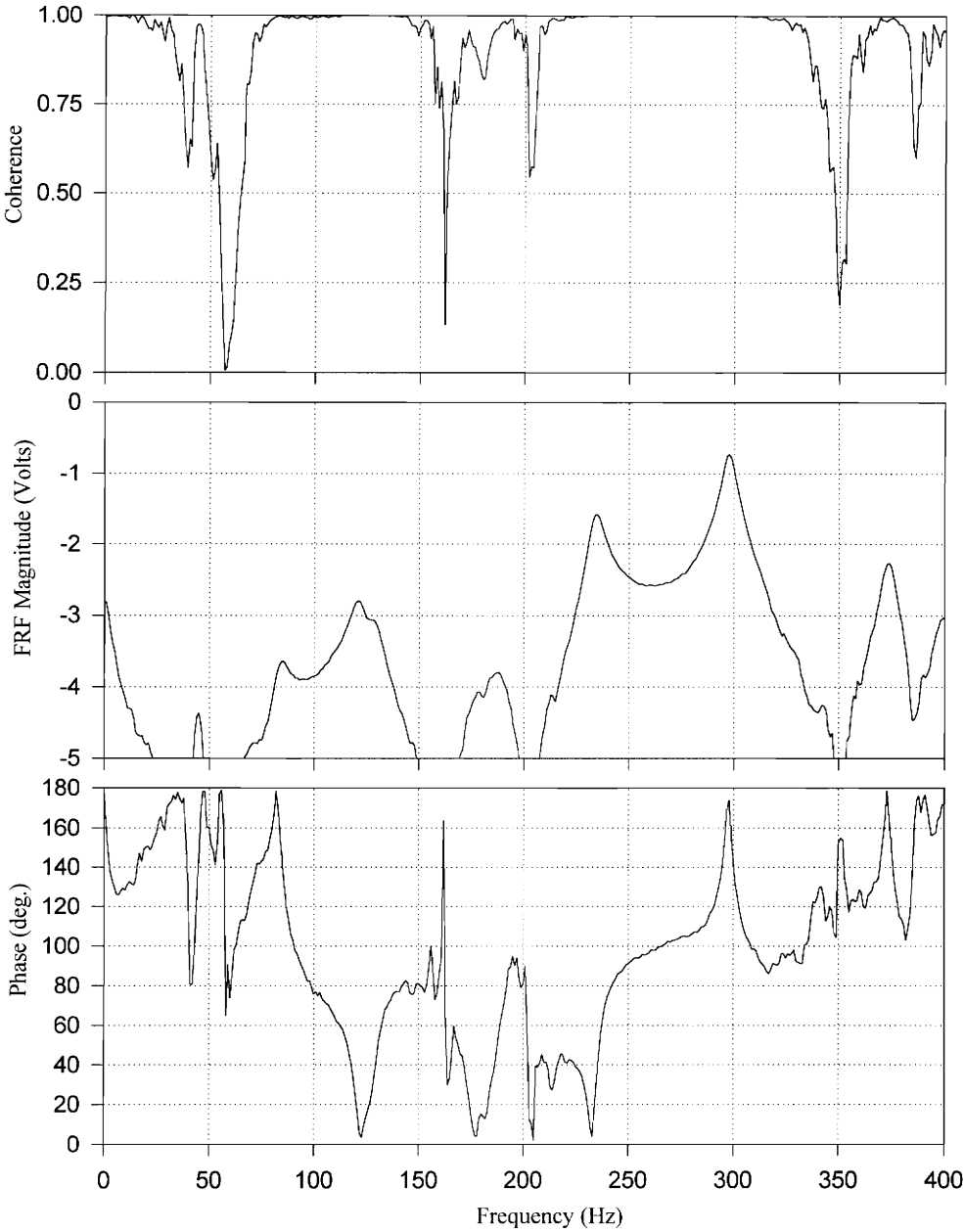
Position 9 Measurement



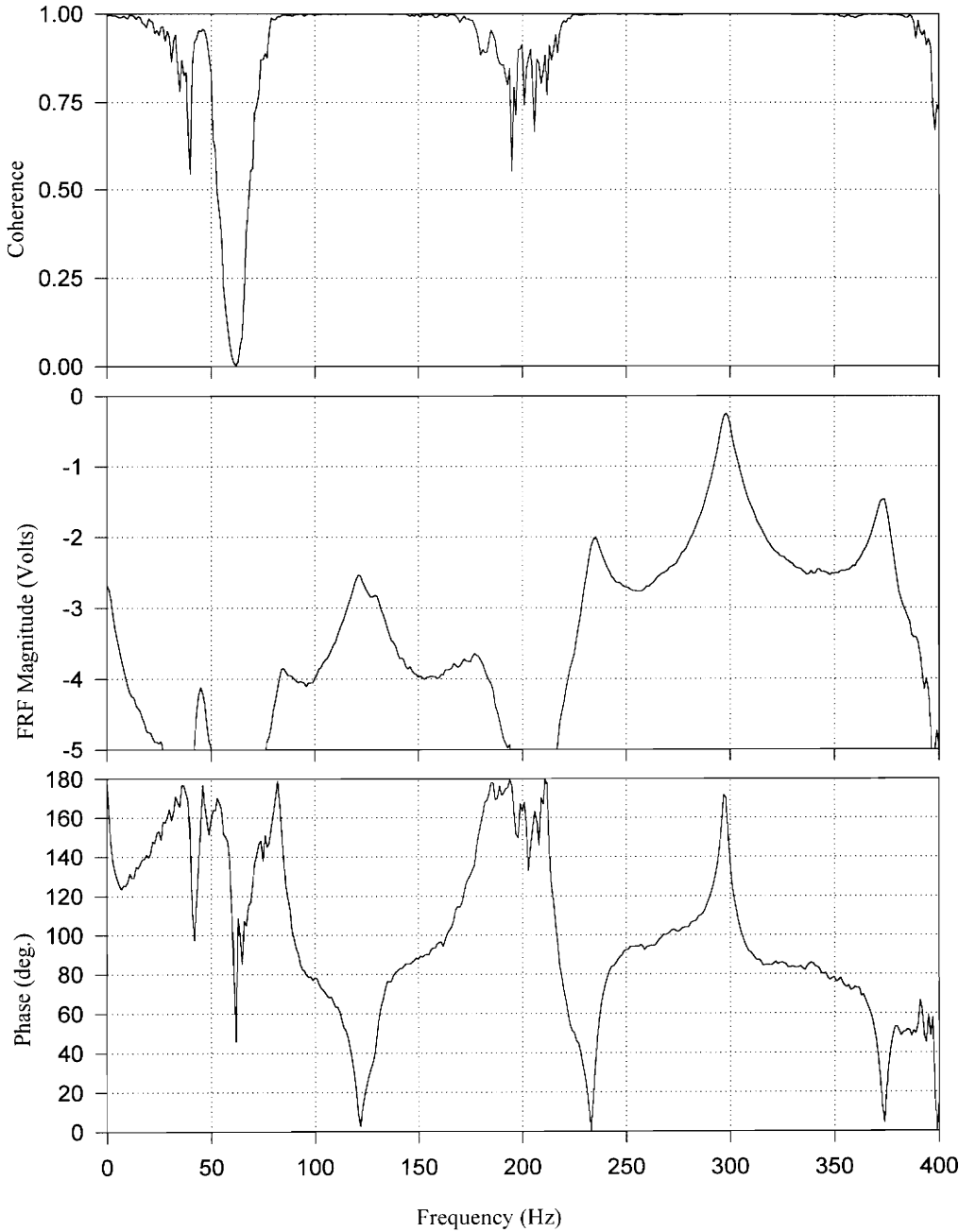
Position 10 Measurement



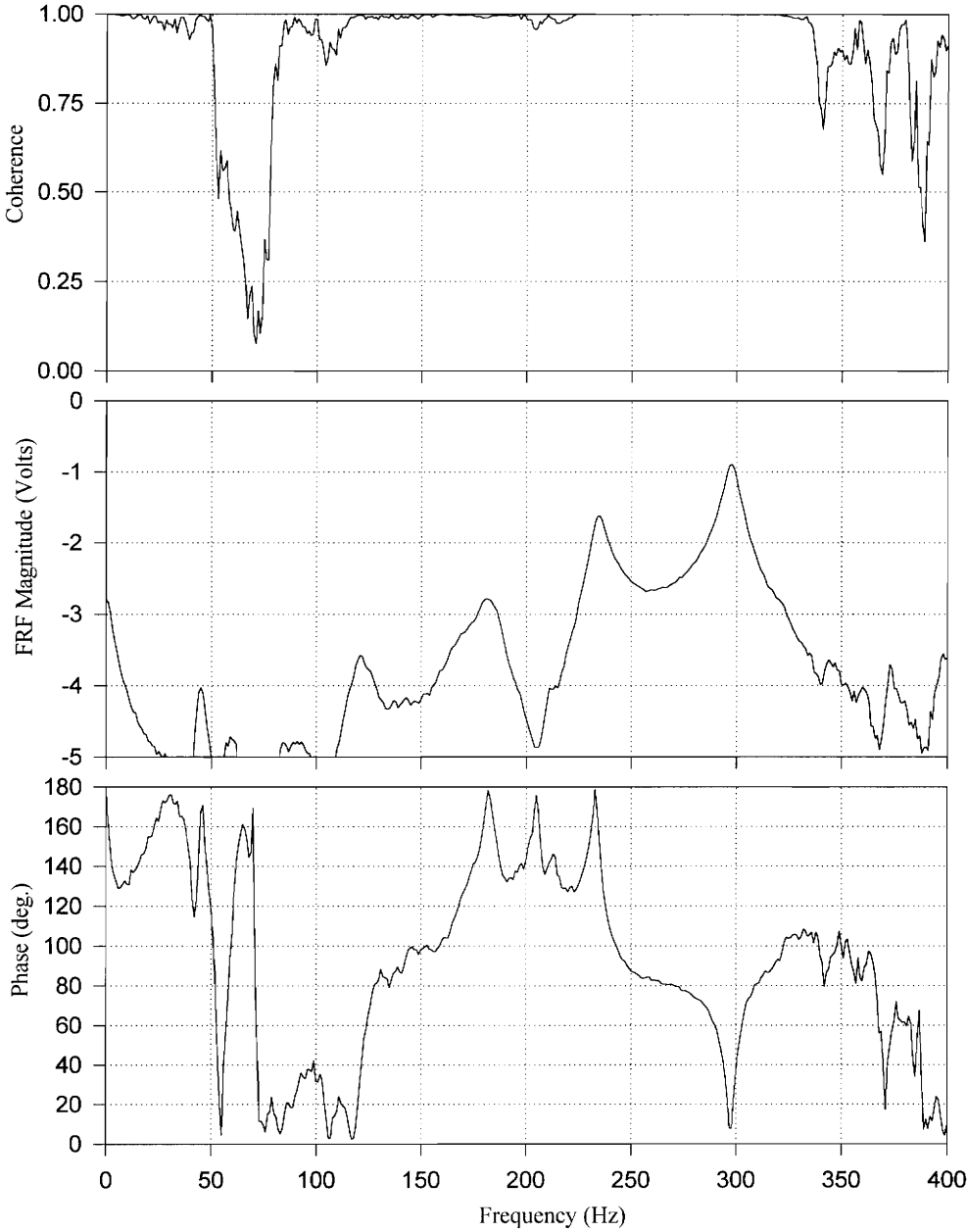
Position 11 Measurement



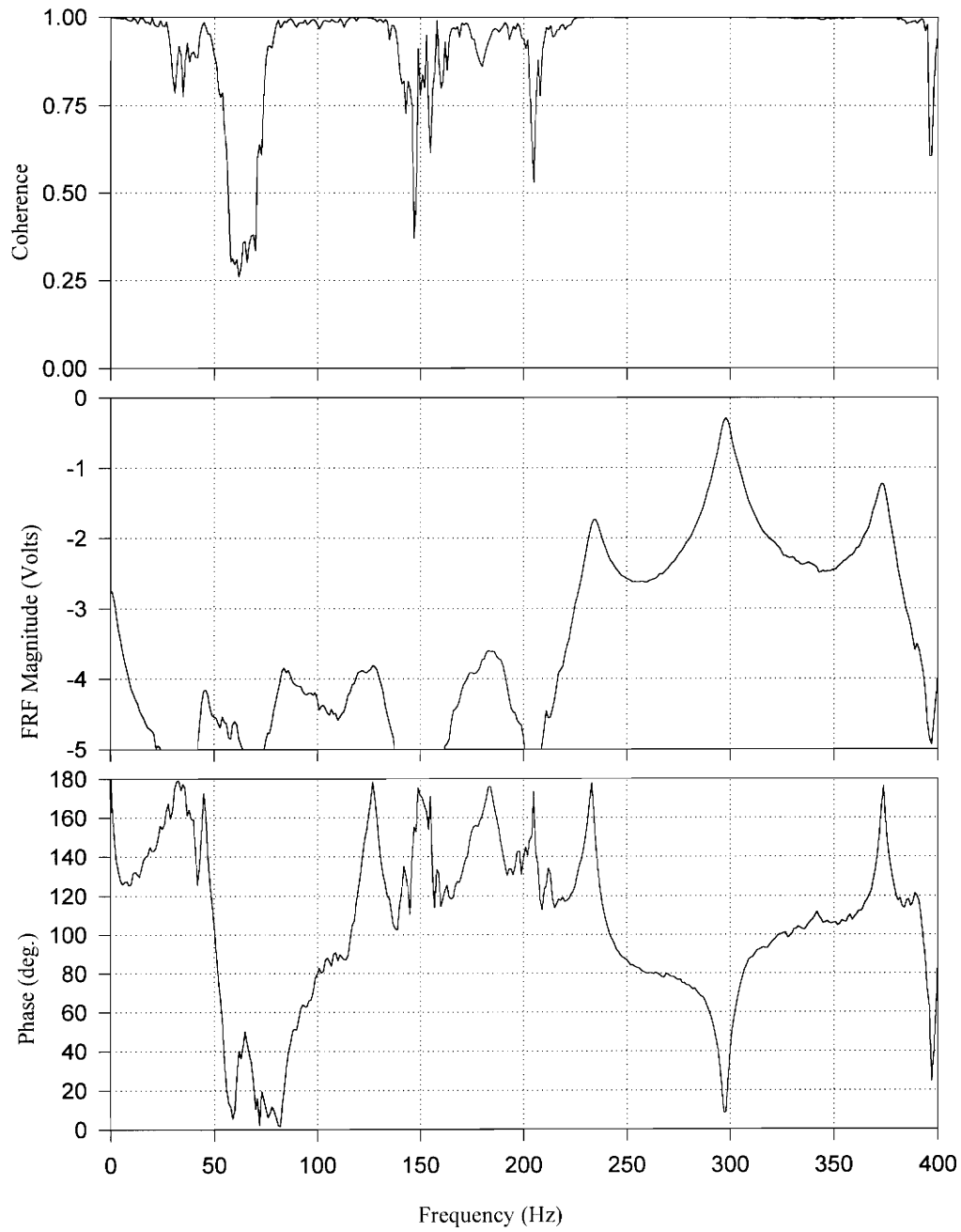
Position 12 Measurement



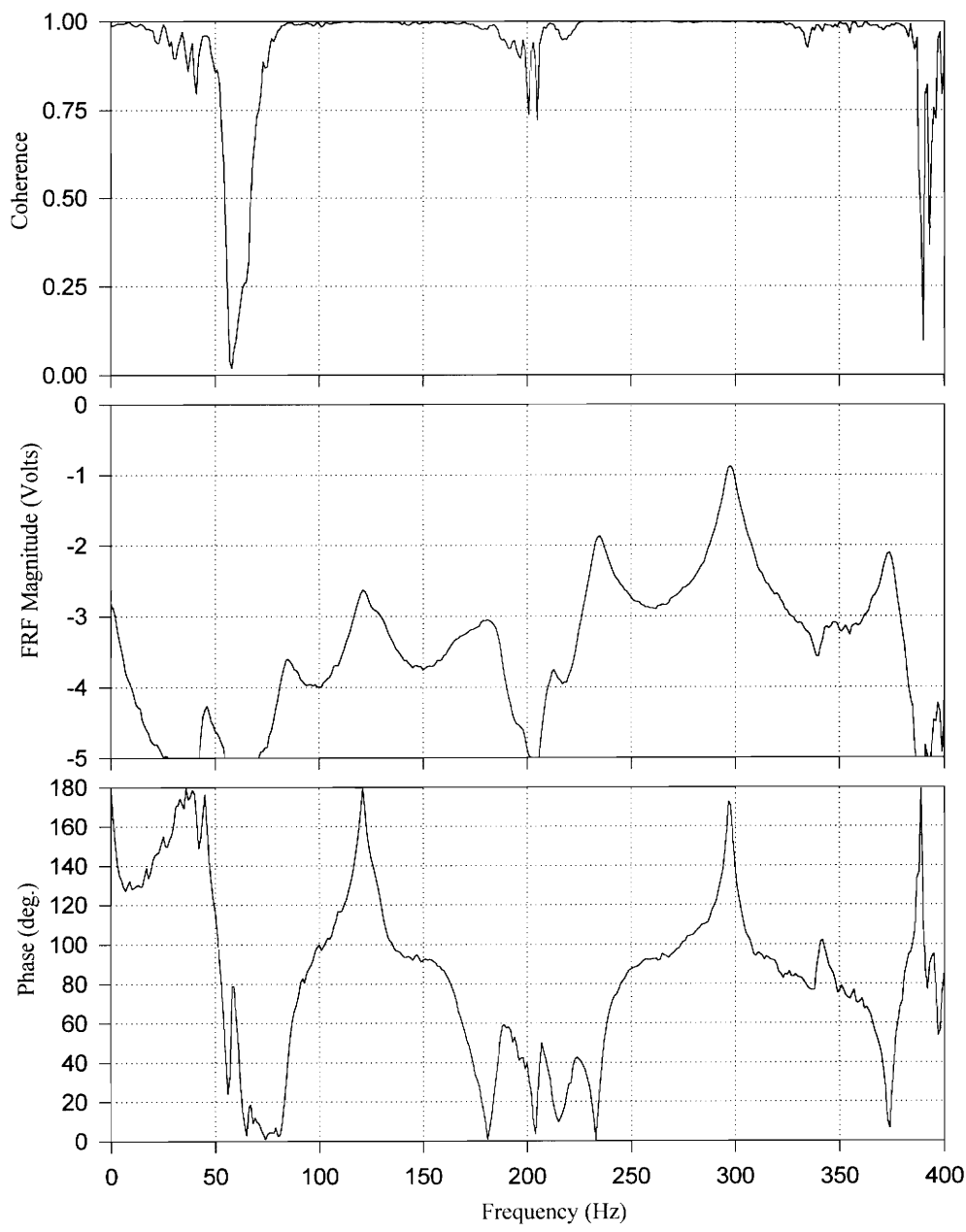
Position 13 Measurement



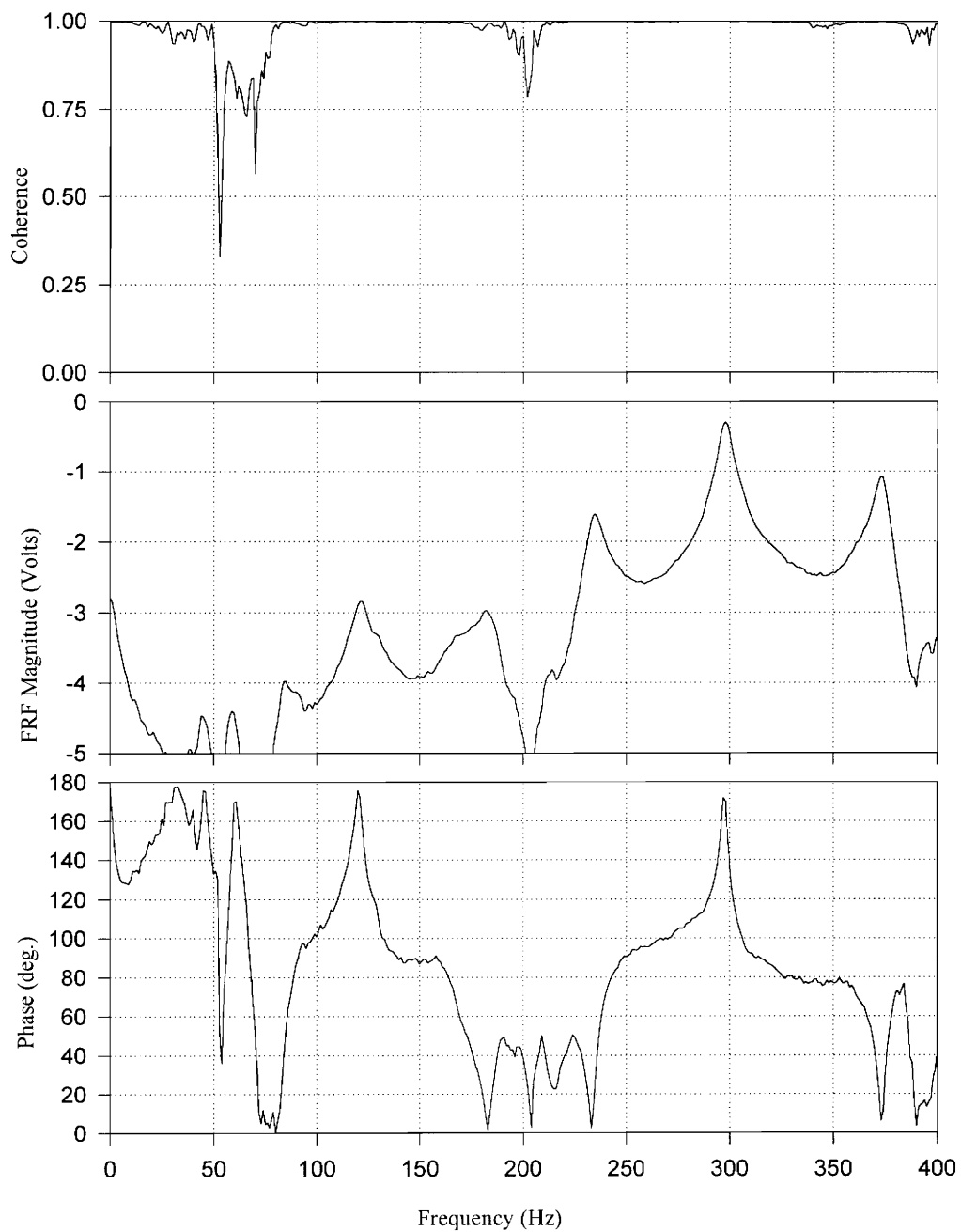
Position 14 Measurement



Position 15 Measurement



Position 16 Measurement

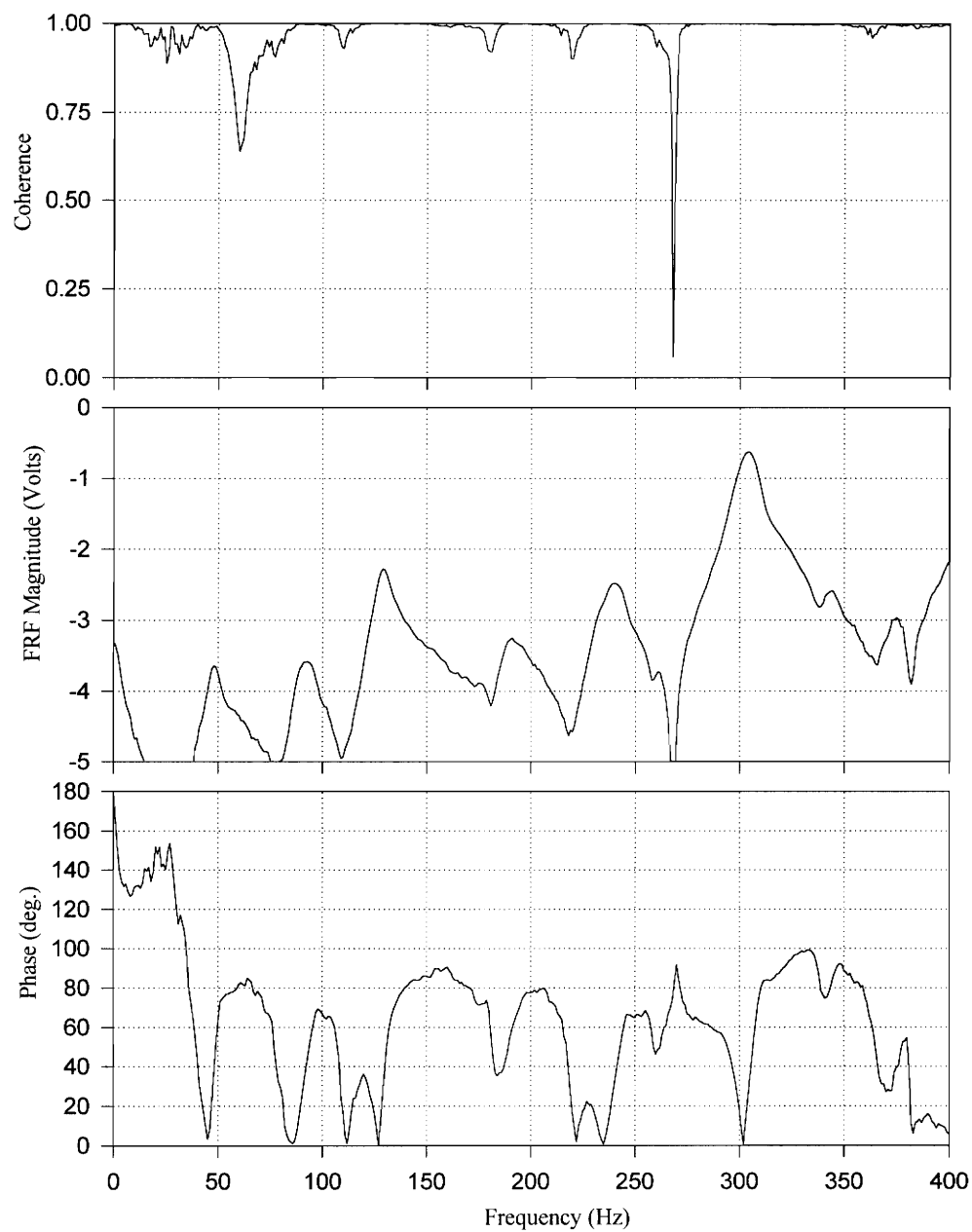


Appendix E

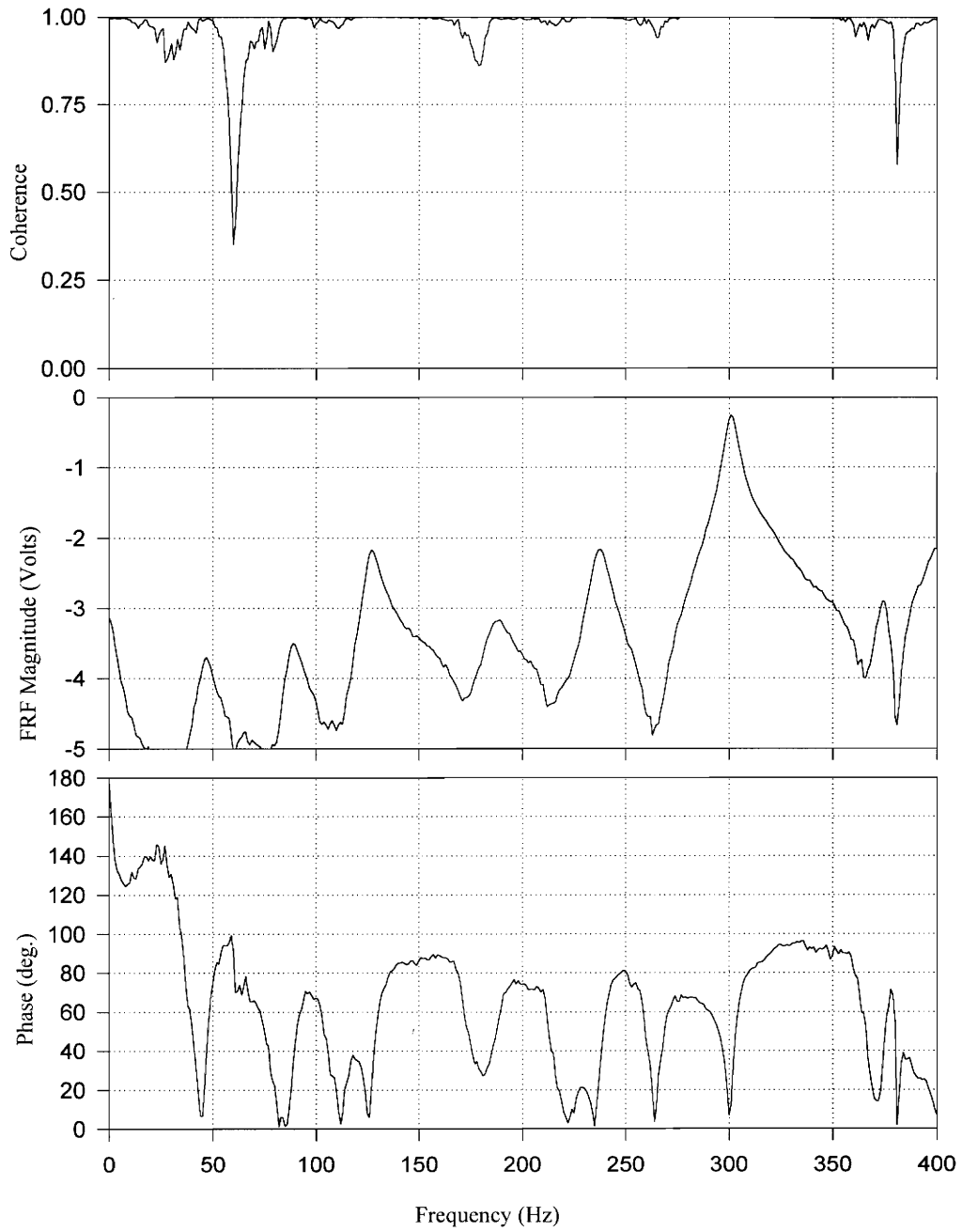
Driving Point FRF's

Data contained in this section correspond to the driving point FRF's (FRF's for which excitation is at the same position as the response measurement). These data were used to determine axial loads and support stiffnesses. FRF's are plotted on a logarithmic scale. Each FRF is an average of 3 measurements. The coherence plots are a measure of the correlation between the 3 measurements where a coherence of 1 indicates a perfect correlation and a coherence of 0 indicates no correlation.

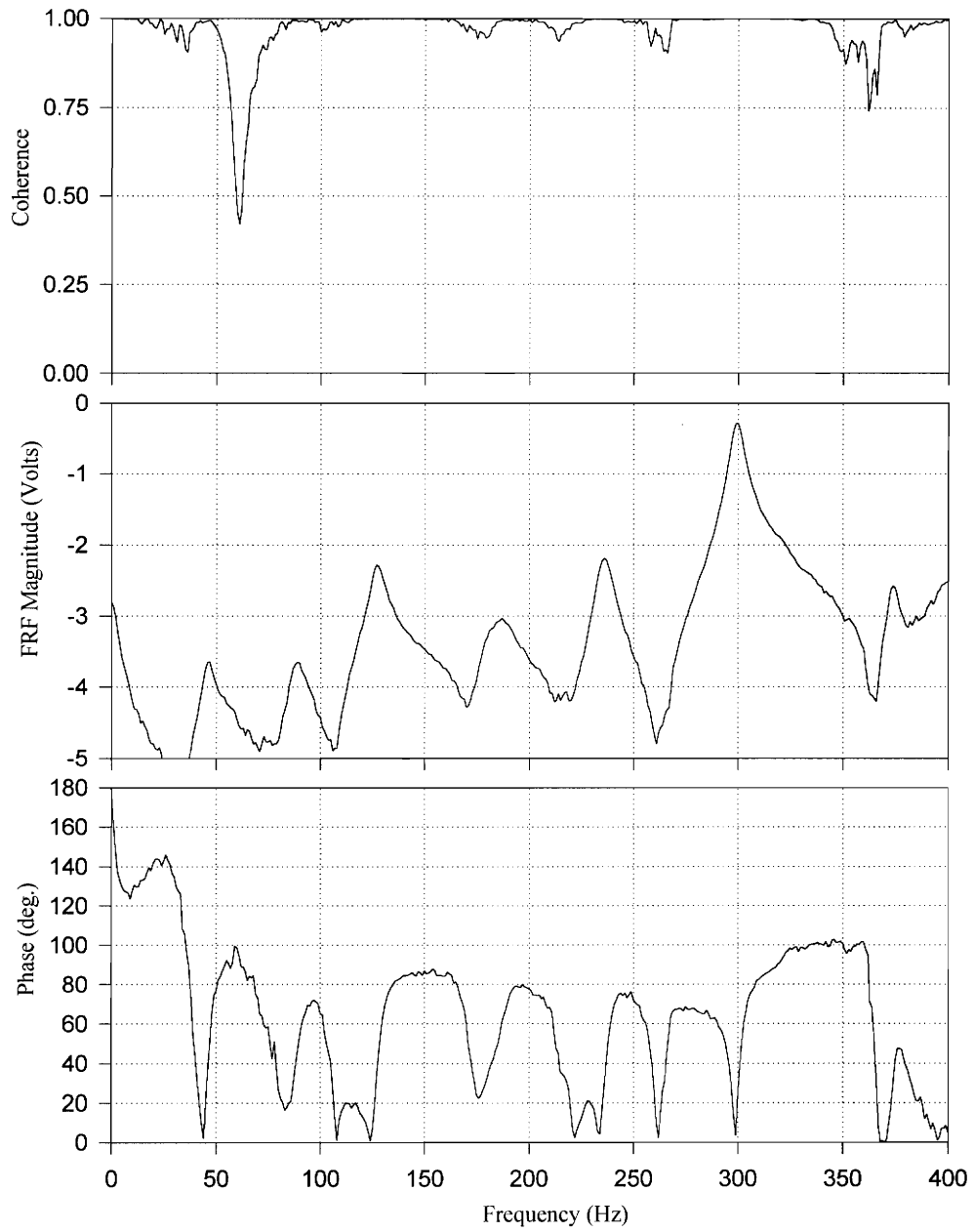
Driving Point Measurements for $k_s=2.7$ kip/in. , $P=5$ kips



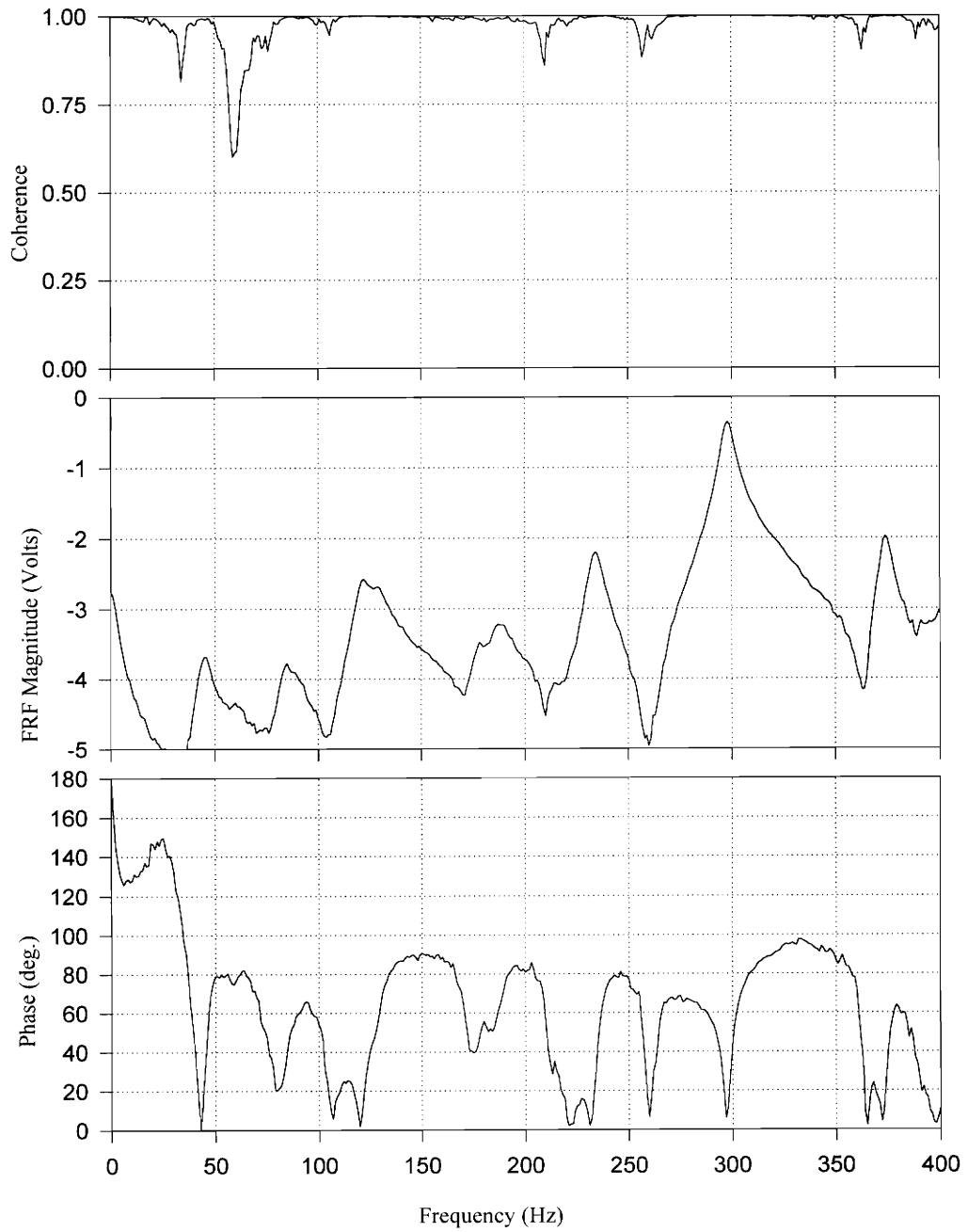
Driving Point Measurements for $k_s=2.7$ kip/in. , $P=10$ kips



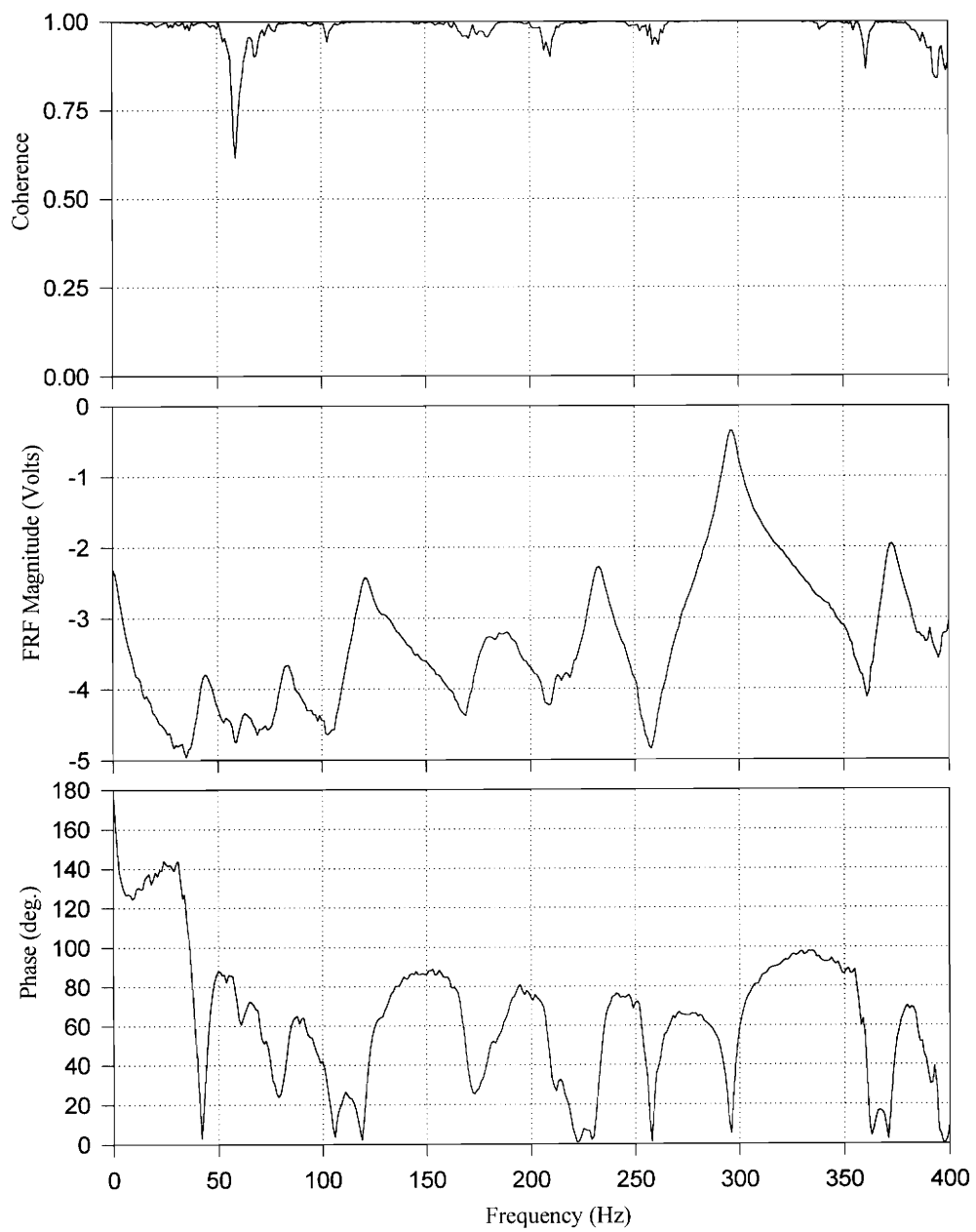
Driving Point Measurements for $k_s=2.7$ kip/in. , $P=15$ kips



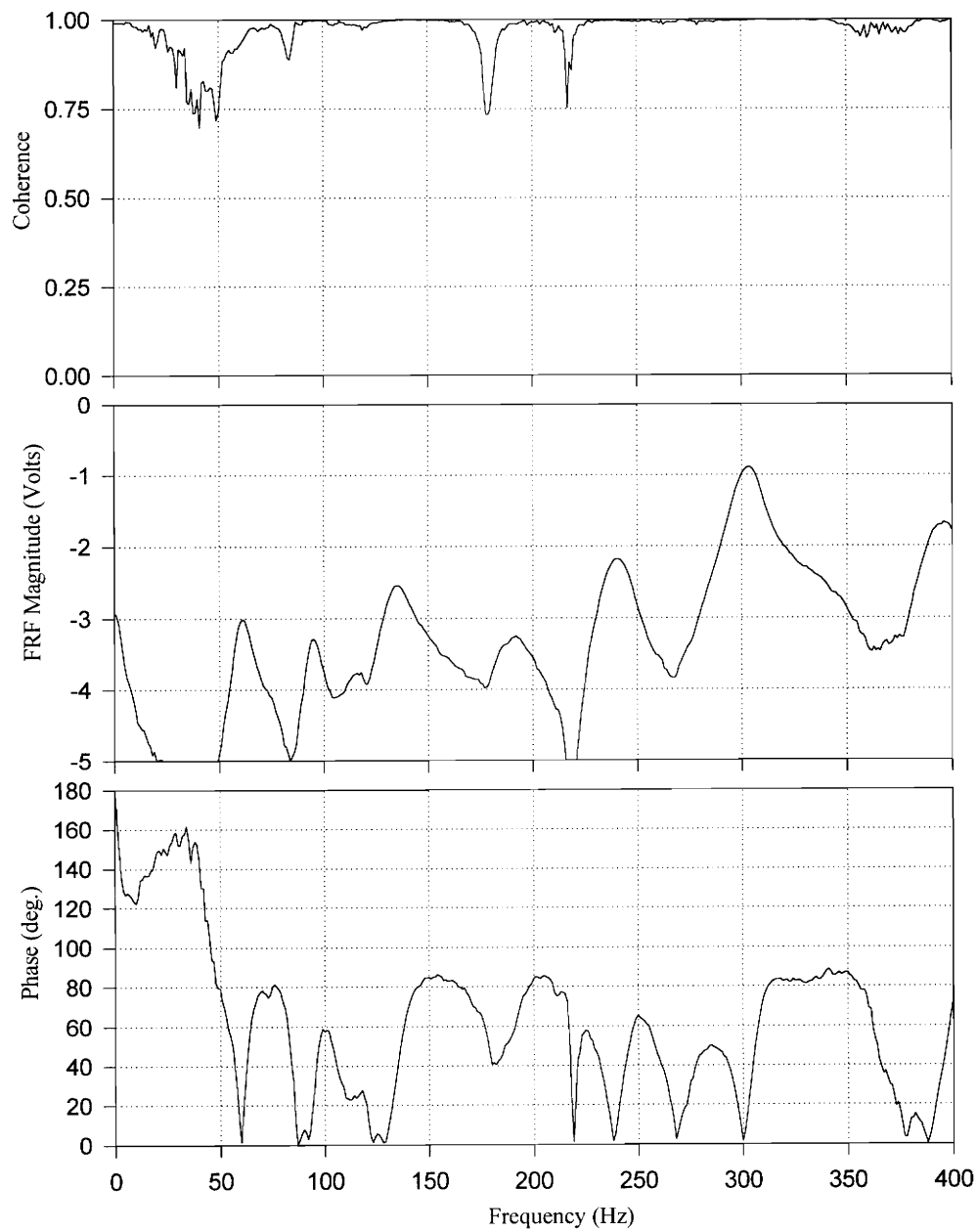
Driving Point Measurements for $k_s=2.7$ kip/in. , $P=20$ kips



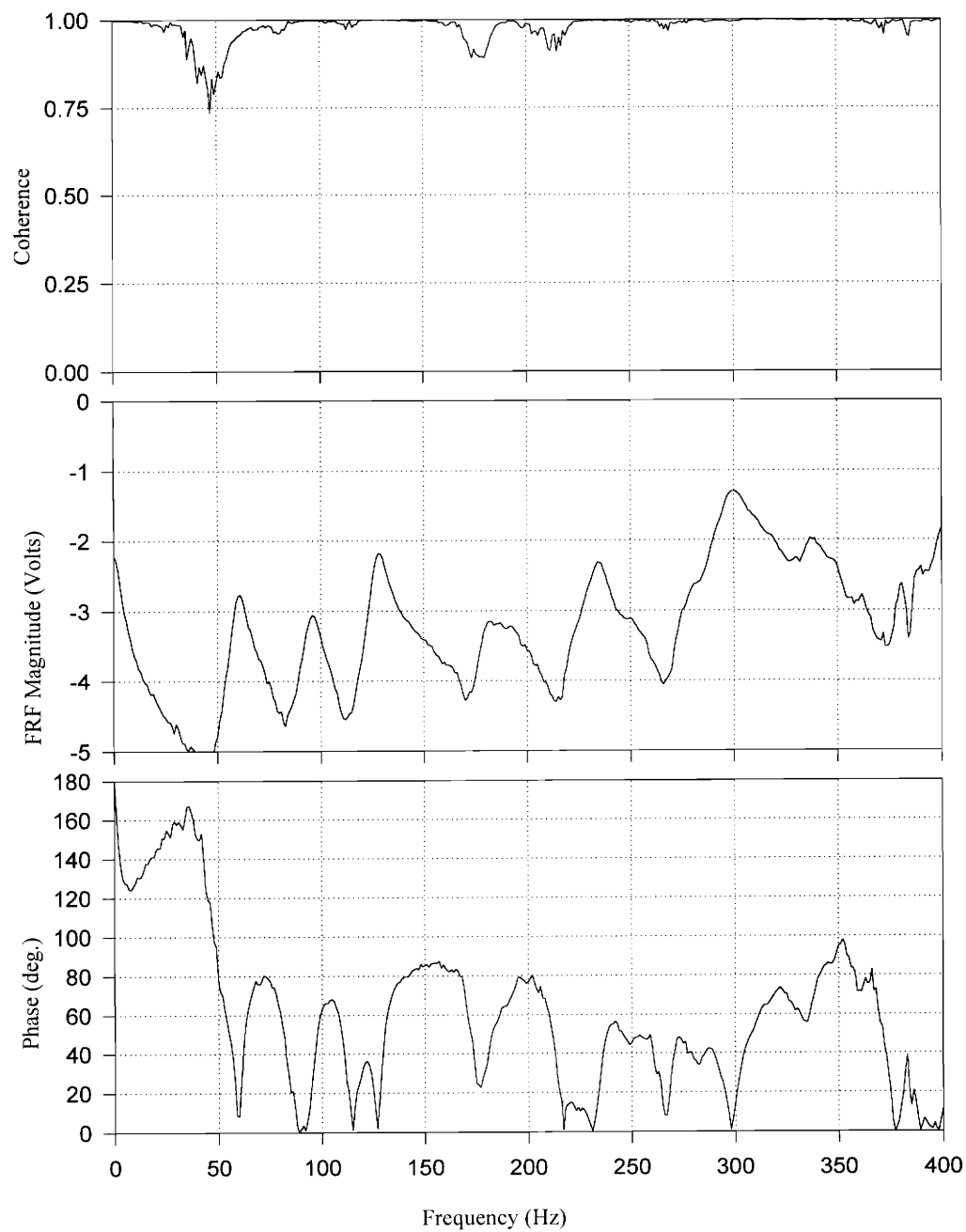
Driving Point Measurements for $k_s=2.7$ kip/in. , $P=25$ kips



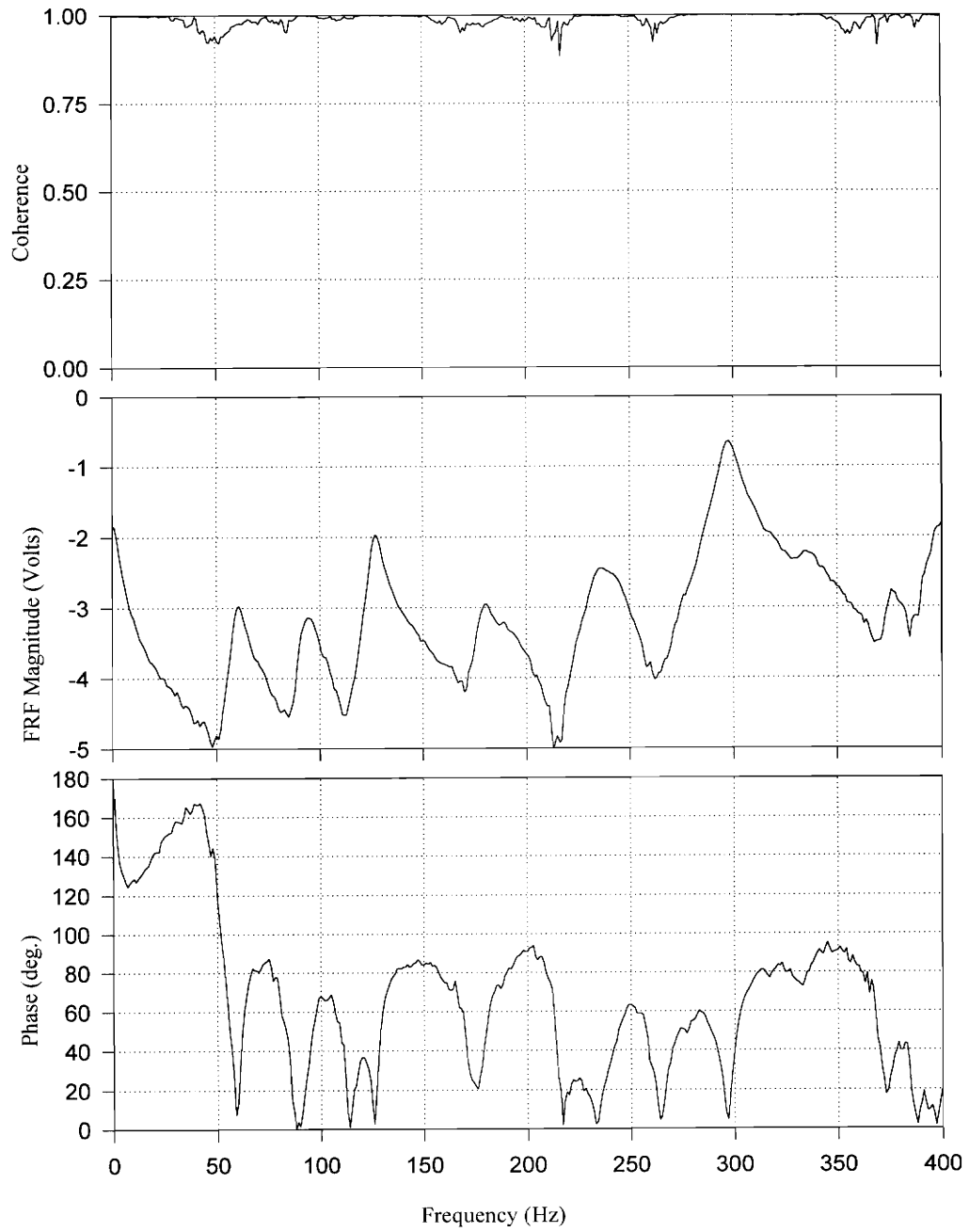
Driving Point Measurements for $k_s=5.4$ kip/in. , $P=5$ kips



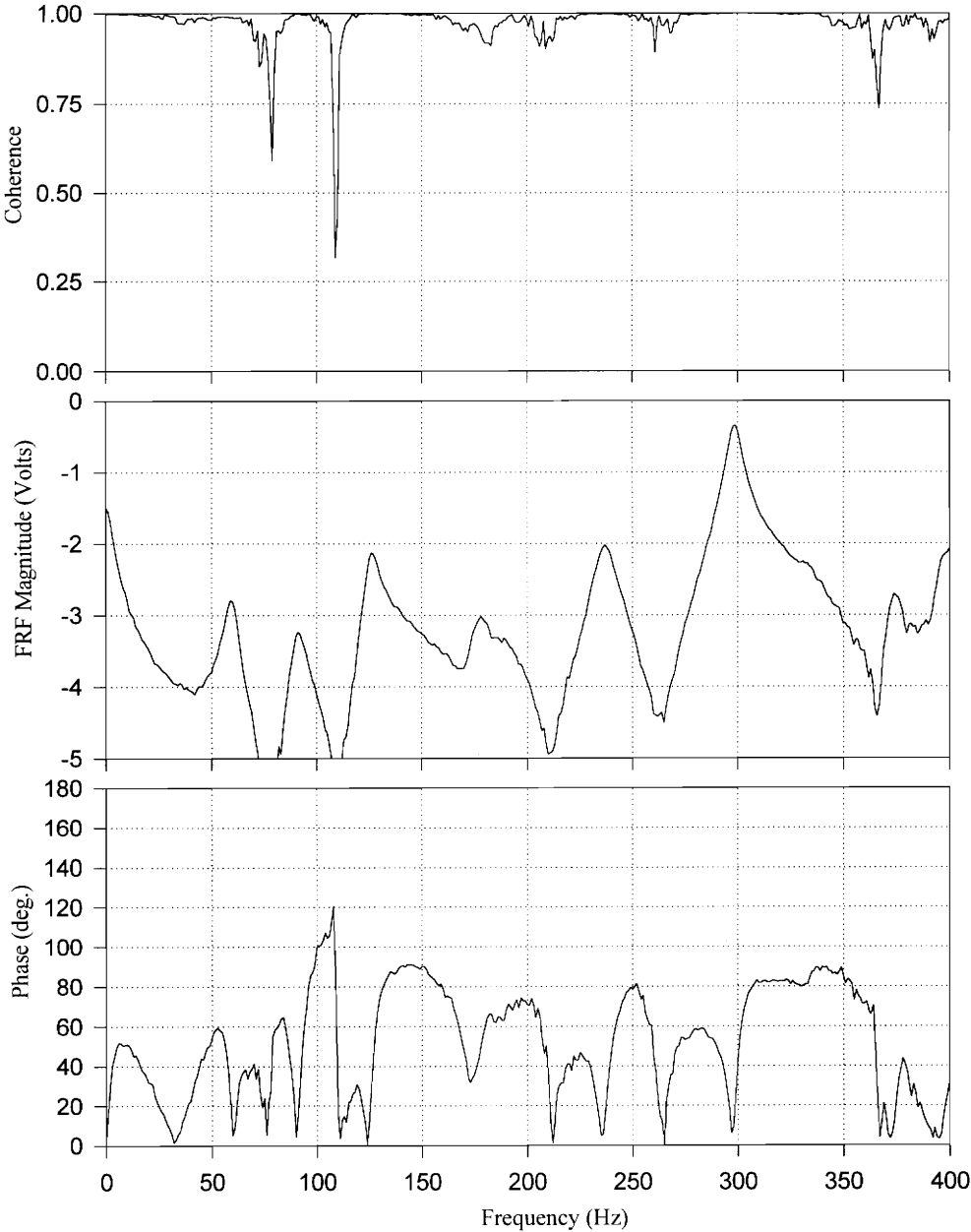
Driving Point Measurements for $k_s=5.4$ kip/in. , $P=10$ kips



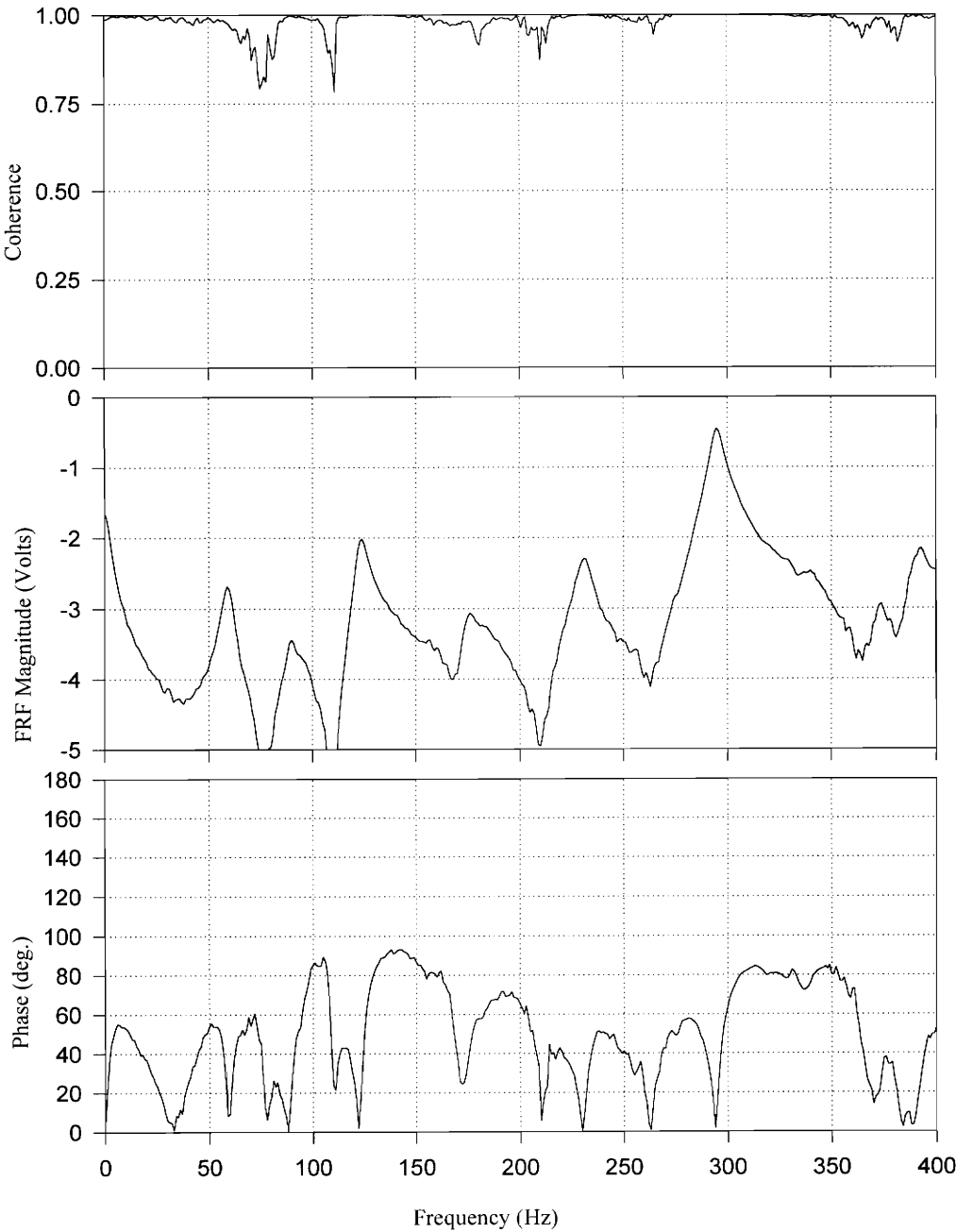
Driving Point Measurements for $k_s=5.4$ kip/in. , $P=15$ kips



Driving Point Measurements for $k_s=5.4$ kip/in. , $P=20$ kips

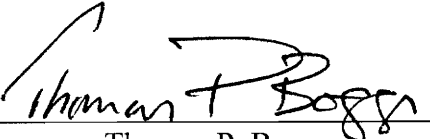


Driving Point Measurements for $k_s=5.4 \text{ kip/in.}$, $P=25 \text{ kips}$



VITA

Thomas P. Boggs was born in Bad Orb, Germany on August 23, 1969. He graduated from General H. H. Arnold High School in Wiesbaden, Germany. In May, 1991, he received a Bachelor of Science degree in Physics from Virginia Polytechnic Institute & State University. In May, 1992, he received a Bachelor of Arts in Philosophy from Virginia Polytechnic Institute & State University. He enrolled in the graduate program at Virginia Polytechnic Institute & State University in August, 1992.



Thomas P. Boggs